ABSTRACT

Title of Thesis:	ASSESSING THE OXIDATIVE HISTORY OF MILLER RANGE MARTIAN METEORITES
	James Wosley Dottin, III, Master of Science, 2016
Thesis Directed By:	Professor James Farquhar, Department of Geology and Earth System Sciences Interdisciplinary Center, University of Maryland-College Park

Miller Range (MIL) Martian meteorites are oxidized nakhlites. Early studies attribute their oxidation to reduction-oxidation reactions involving assimilated sulfate. I utilize the sulfur isotope and major element composition of the MIL pairs to assess their oxidative history.

MIL sulfides display an average sulfur isotope composition that is different from Nakhla sulfate and sulfide. The sulfur isotope differences produce a mixing array between juvenile sulfur and mass-independent sulfur signatures, indicating assimilation of anomalous sulfur into the melt. I estimate an fO_2 of QFM ($+3.5 \pm 0.4$) and a sulfur content of 360 ppm ± 12 – 1300 ppm ± 50. With these results, I test the hypothesis of sulfate assimilation through models of charge balance, isotope mixing, and degassing of sulfur bearing compounds. I conclude that sulfate assimilation was significant in the oxidation of the MIL pairs but, additional oxidants were assimilated.

ASSESSING THE OXIDATIVE HISTORY OF MILLER RANGE MARTIAN METEORITES

by

James W. Dottin III

Thesis submitted to the Faculty of the Graduate School of the
University of Maryland, College Park, in partial fulfillment
of the requirements for the degree of
Master of Science
2016

Advisory Committee:
Professor James Farquhar, Chair
Professor Phil Piccoli
Professor William McDonough

Acknowledgements

I owe endless gratitude to my advisor Dr. James Farquhar and mentor Dr. Jabrane Labidi for their endless advising, reading of drafts, and mentorship in academic and life pursuits. Additionally, I owe thanks to other lab members, especially Dr. Joost Hoek and Daniel Eldridge for teaching me lab techniques and helping me understand sulfur isotope systematics. I thank Dr. Phil Piccoli for his constructive insight to this project and help with analyses on the electron microprobe and Dr. William McDonough his constructive insight for this project. I thank Ming-Chang and Kevin McKeegan for their help with SIMS analyses at UCLA.

I acknowledge Mark Larson, Chao Gao, Alex Ray, Priyanka Moondra, Evan Weber, and Andrew Pfeiffer for their love, friendship, and endless support throughout this journey to the M.Sc. degree. I would also like to thank my family James, Sartreina, Tatjana, Janiece, Sharai and my girlfriend Ruth for their endless and unconditional love throughout this journey.

I acknowledge the NSF, NASA, and TRIO for funding this project and my salary. I also thank the Meteorite Working Group for providing samples used in this thesis.

Table of Contents

List of Tables

List of Figures

Chapter 1: Introduction

225 million miles away from earth lay a red planet, Mars. The cold, desert like planet covered in rusty red iron bearing minerals was geologically active, spewing out hot lava from volcanoes up to 180 million years ago or so. Some may not be able to tell the difference between pictures of mars or pictures of the mid-western United States because Mars underwent geologic activity similar to that happening on Earth. Examples are processes such as volcano formation and eruptions and the flowing of liquid water to form gullies and deep valleys. Today, the Martian surface is rich with ancient volcano material and remnants of evaporated streams and lakes. Through the use of robots (or rovers) and pieces of Mars that landed on Earth (called Martian meteorites) after being blasted off of the Martian surface by an asteroid impact, scientists aim to develop a deeper understanding of Mars' geologic history.

Considering Mars is a different planet, the likelihood of unique material is high. The bulk of rock material from Mars is chemically very similar to Earth, excluding evidence for processes unavailable to mars such as the movement of plates underneath the surface. Some of the rocks from Mars are very different, and to this day, the reason for their differences has yet to be agreed upon in the science community. This thesis focuses on a group of Martian meteorites that are chemically different from Earth. The thesis further develops a previously proposed hypothesis that can explain the observed differences. To develop the hypothesis, this thesis

focuses on three key chemical elements: oxygen, iron, and sulfur; and four key minerals: pyroxene, olivine, magnetite, and sulfide.

Martian SNC (Shergottite Nakhlite Chasignite) meteorites have been shown to record a wide range of oxygen fugacities (Iron-Wüstite (IW) -1 to Iron-Wüstite (+4). Shergottites record fO_2 values that range from one log unit below the Iron-Wüstite (IW) buffer, to two and a half log units above the Iron-Wüstite buffer (Fe:FeO) (Herd et al., 2002; Wadhwa, 2008, 2001). The oxidizing conditions recorded by shergottites and nakhlites imply variations of fO_2 that span over five orders of magnitude. Nakhlites are more oxidized than the shergottites (fO_2 of IW +3 to +4 (Wadhwa, 2008). For comparison, the lowest oxygen fugacity (IW -1) for shergottites is well below the fO_2 value recorded for Earth's upper mantle (roughly IW +3.5 or QFM, (Cottrell and Kelley, 2011). Since the low fO_2 values are generally assumed to represent the Martian mantle source (Wadhwa, 2008), it is inferred that Mars underwent differentiation and geological evolution under significantly more reducing conditions than Earth. The origin of the oxidized components in the Martian meteorites, seen in the nakhlites and some shergottites, remains unclear. Some of the more oxidized shergottites have been shown to record processes of crustal assimilation (Wadhwa, 2001). The fO_2 observed in the nakhlites could also indicate widespread assimilation of oxidized surficial material by the parental magmas (Franz et al., 2014; McCubbin et al., 2009). Franz et al. (2014) argue nakhlites underwent assimilation of oxidative surface sulfate salts. Tuff et al. (2013), however, suggest the SNC meteorites are sampling a deep (>190km) reduced mantle source, while older

material (i.e. Gusev crater ~3.7 Ga), sample a shallower mantle that was oxidized by crustal recycling early in Mars' history.

The assimilation of sulfate that hosts mass-independent fractionation (MIF) into Martian melts offers a way to oxidize iron. Franz et al. (2014) propose the reduction of sulfur in its S^{6+} valence to its S^{2-} state consumes 8 moles of electrons that can be used to oxidized 8 moles of Fe^{2+} to Fe^{3+}. This reaction was suggested by Franz et al. (2014) to occur in nakhlite melts, as the MIF signature of some sulfides from MIL meteorites displayed a composition similar to Martian MIF-bearing sulfates.

This thesis tests whether sulfate assimilation and reduction is a viable explanation for the high oxygen fugacity observed in the MIL Martian meteorites. Martian SO_4 from Nakhla, produced in the atmosphere, carries an anomalous $\Delta^{33}S$ signature of -1.25 ± 0.008‰ (Farquhar et al., 2007). In order to assess the feasibility of the hypothesis proposed by Franz et al. (2014), this thesis reports on: (1) the S-isotope composition for troilite obtained via SIMS and GS-IRMS (published in Franz et al., 2014) to characterize the level of isotopic heterogeneity that exists among MIL troilite grains, (2) X-ray mapping to determine the modal abundance and the ratio of magnetite to troilite in the MIL pairs, (3) mass balance calculations of hypothetical assimilation reactions, and (4) wavelength-dispersive spectroscopy (WDS) analyses of phases combined with site assignments to determine Fe^{3+} content and oxygen fugacity. The average bulk rock $\Delta^{33}S$ value (previously measured by Franz et al., (2014)) of sulfides in the MIL nakhlites is -0.512± 0.008‰, displaying evidence for assimilated Martian sulfates preserved in nakhlite meteorites that were reduced in the precursor melt of the MIL meteorites. This work focuses on a group of three

meteorites (MIL 090030, MIL 090032, MIL 090136) that have been genetically linked to (paired with) MIL 03346 because of shared petrographic features and discovery in a common geographic region. MIL 03346 has demonstrated to be the most oxidized nakhlite among all nakhlites, record an fO_2 of QFM +1.5 using Fe^{3+} contents in pyroxene determined via Mossbauer Spectroscopy (Dyar et al., 2005). Such findings on MIL 03346 make its genetically linked meteorites (MIL 090030/090032/090136) important targets in assessing the oxidation of Martin nakhlites.

Chapter 2: Background

2.1 Martian surface mineralogy

The Martian surface has been observed and analyzed for its mineralogy using both satellite orbiter instruments and rovers. Thermal Emission Spectrometer (TES) and Pancam spectra on the Mars Exploration Rover (MER) have identified several possible matches for hydrous iron sulfates (Johnson et al., 2007). The Observatoire pour la Minéralogie, l'Eau, les Glaces et l'Activité (OMEGA), and Compact Reconnaissance Imaging Spectrometer (CRISM) on the Mars Reconnaissance Orbiter identified sulfate mineral evaporites on the Martian surface such as gypsum ($CaSO_4 \cdot 2H_2O$), kieserite ($MgSO_4 \cdot H_2O$), and polyhydrated sulfates (Gendrin et al., 2005; Lichtenberg et al., 2010; Murchie et al., 2009). The Martian surface is dominated by basaltic rock with regional variability in the abundance of minerals such as plagioclase, pyroxene, and olivine (Ehlmann and Edwards, 2014). Such variability indicates differences in magma composition (Ehlmann and Edwards, 2014). Additionally, the occurrence of large impact basins with enrichments in high-Mg olivine implies either excavation of the upper mantle or the emplacement of a high-temperature lava following the impact event (Ehlmann and Edwards, 2014). Where there is Noachian (4.1-3.7 million years ago) dated crust exposed at the surface, clay minerals exist, suggesting the occurrence of aqueous alteration processes. The surface of Mars also hosted paleolakes in the late Noachian, where enhanced near surface weathering may have taken place, generating various aluminum clay minerals, sedimentary clay minerals, and precipitated salts such as

sulfates, chlorides and carbonates (Ehlmann and Edwards, 2014). Additionally, groundwater alteration during the Hesperian (a Martian epoch that ended between 3.455 and 1.8 billion years ago) played an important role in the formation and deposition of clay minerals, sulfates (mainly iron and aluminum sulfates, (Tosca et al., 2005; Wray et al., 2010, 2009), hematite, and chlorides. The sulfates tend to form as gypsum, Mg-sulfate, jarosite, and alunite (Wray et al., 2010, 2009). Lastly, carbonate bearing rocks with minor amounts of olivine have been detected in small quantities (Harner and Gilmore, 2015).

2.2 Sulfur in Martian meteorites

Achondrites are stony meteorites that originate from differentiated asteroids, planetessimals and planets. One group of achondrites is interpreted to come from Mars. These Martian meteorites preserve young radiometric solidification ages (Nyquist et al., 2001) that suggested a planetary origin. Additionally, dynamical arguments were made by Ashwal et al. (1982), that it was more likely that the material originated from Mars than from another solar system body. Similarities between the noble gas and nitrogen composition of the Martian atmosphere, gases trapped in shock glasses of EETA 79001 (Becker and Pepin, 1984; Bogard et al., 1984; Pollack and Black, 1982), and petrological similarities (Stolper and McSween, 1979) provided further support for a Martian origin (Ott and Begeman, 1985).

The first report of relative sulfur isotope abundances in Martian meteorites was by Burgess et al. (1989). This study used SO_2 generated from the sulfur bearing minerals, troilite (FeS) and gypsum ($CaSO_4 \cdot 2H_2O$), in Shergotty, ALH 77705, Nakhla, and Chassigny. Given the nature of sample size and sulfur content, Burgess

et al. (1989) were only able to obtain a measurement from Shergotty, from which they report a $\delta^{34}S$ value of -0.5 ± 1.5‰.

Gao and Thiemens, (1990) report bulk rock sulfur isotopic analyses on ALH 77005 in Table 1 below.

Table 1. Sulfur Isotopic Composition of ALH 77005 from Gao and Thiemens (1990)

Phase	$\delta^{33}S$ (‰)	$\delta^{34}S$ (‰)	$\delta^{36}S$ (‰)
Acid Soluble	-0.07 ± 0.03	-0.17 ± 0.03	-0.3 ± 0.2
Acid Residue	1.65 ± 0.2	3.30 ± 0.2	6.2 ± 0.8

The acid soluble phase is presumed to be troilite, whereas the acid residue phase is assumed to be gypsum, however, the acid residue phase could have a component of S^0 from a reaction between acid volatile sulfur (AVS) and Fe^{3+} in the rock, where the reduction of Fe^{3+} to Fe^{2+} can catalyze the production of S^0 from S^{2-}. These values yield calculated $\Delta^{33}S$= 0.02‰ and -0.05‰ for the acid soluble and acid residue phase respectively and $\Delta^{36}S$=0.02‰ and -0.08‰ for the acid soluble and acid residue phase respectively.

Greenwood et al. (1997) measured the sulfur isotopic composition of shergottites using ion microprobe techniques. Data from Greenwood et al. (1997) is reported below in Table 2 (where all error is reported as 1σ). Greenwood et al. (1997) argue that their data illustrate values that are similar to those on the terrestrial ocean

floor, suggesting that the sulfur isotopic composition of the Martian mantle is similar to that of the terrestrial mantle.

Table 2. Sulfur isotopic composition of shergottites from Greenwood et al. (1997)

Sample/phase	$\delta^{34}S$ (‰)
Shergotty pyrrhotite	-0.5 to 0.2‰ ± 0.7‰
Zagami pyrrhotite	1.4 to 3.1‰ ± 0.7‰
EET 79001 lithology A pyrrhotite	-2.6 to 0.2‰ ± 0.4‰
QUE 94201 pyrrhotite	0.1 to 1.5‰ ± 0.6‰
LEW 88516 pyrrhotite	-2.9 to -0.9‰ ± 0.6‰
EET 79001 lithology B pyrrhotite	2.6 to -1.5‰ ± (0.4‰)

Farquhar et al. (2000) measured 12 SNC Martian meteorites and report $\delta^{34}S$= -0.92 to 5.25‰, $\Delta^{33}S$= -0.302 to 0.071‰ (standard error= 0.001 to 0.051‰), $\Delta^{36}S$=0.0 to 2.6‰ (standard error= 0.1 to 1.6‰). They argued that variability for $\Delta^{33}S$ could be attributed to atmospheric chemical reactions. Continued study on Nakhla by Farquhar et al. (2007) revealed relatively large S-MIF signatures for $\Delta^{33}S$ (see Table 3).

Table 3. Sulfur isotopic composition of Nakhla from Farquhar et al. (2007)

Sample/phase	$\delta^{34}S$	$\Delta^{33}S$	$\Delta^{36}S$
BM 1913.25 total sulfate	4.7 ± 0.2‰	-1.25 ± 0.01	-0.16 ± 0.2
BM 1913.25 Chromium Reducible Sulfide	-1.6 ± 0.2	-0.09 ± 0.01	-0.24 ± 0.2

BM 1913.25 Acid Volatile Sulfur	0.9 ± 0.5	-0.06 ± 0.03	0.06 ± 0.2

The statistically significant differences in $\Delta^{33}S$ for sulfide and total sulfate in Nakhla in Farquhar et al. (2007) suggest that sulfide and sulfate contain sulfur that was processed in different ways.

Franz et al. (2014) conducted a more extensive and comprehensive sulfur isotopic study on SNC meteorites in order to understand atmosphere-surface interactions and the deep sulfur cycle on Mars. A summary of results from nakhlites is reported in Table 4.

Table 4. Compiled summary of sulfur isotopic composition of nakhlites from Franz et al. (2014)

Phase	$\delta^{34}S$	$\Delta^{33}S$	$\Delta^{36}S$
Water-soluble sulfate	4.36 to 12.75‰ ± 0.15‰	-0.576 to -0.176‰ ± 0.008‰	-0.48 to 0.38‰ ± 0.15‰
Acid-soluble sulfate	-0.57 to 10.39‰ ± 0.15‰	-0.474 to -0.070‰ ± 0.008‰	-0.67 to 0.46 ± 0.15
Chromium reducible sulfide	6.81 to 8.78‰ ± 0.15‰	-0.538 to -0.434‰ ± 0.008‰	-0.04 to 0.18‰ ± 0.15‰

This data demonstrates the presence of both an oxidized (sulfate) and reduced (sulfide) species with mass-independent (see background section 2.4) sulfur isotopic values that appear to be opposite to those found in Nakhla (Farquhar et al., 2007) (i.e. strongly negative $\Delta^{33}S$ for sulfide in nakhlites vs. strongly negative sulfate in Nakhla) that are attributed to photochemistry. Franz et al. (2014) attribute the presence of an

oxidized and reduced sulfur species to the assimilation of sulfate species that are then reduced while Fe in pyroxene bearing minerals are oxidized to form magnetite.

2.3 Samples studied: Miller Range (MIL) 090030/090032/090136/03346

The Miller Range meteorites 090030/090032/090136/03346 are nakhlite Martian meteorites found in the Miller Ranges of Antarctica. MIL 03346 was collected during the 2003 meteorite collection season while the MIL 090030/090032/090136 meteorites were collected during the 2009 meteorite collection season. MIL 03346 is a clinopyroxenite that was shown to be the most oxidized (QFM +1.5, (Dyar et al., 2005)) and least equilibrated nakhlite among all nakhlites (Udry et al., 2012). The lack of equilibration is evidenced by in the high amounts of intergranular crystals and interstitial glass (avg. ≈ 24.1) within the mesostasis (Hallis and Taylor, 2011; Kuebler, 2013; McCanta et al., 2009; Udry et al., 2012), as these are crystals that were emplaced within the flow late in its history. MIL 090030, 090032, and 090136 were paired with MIL 03346 on the basis of similarities in the mineralogy and texture of both the cumulus and intercumulus phases (Day et al., 2006; Hallis and Taylor, 2011; Udry et al., 2012). The cumulus phases in all four MIL meteorites are the euhedral-subhedral zoned olivine and zoned pyroxene grains with magnesium-rich cores and ferroan rims (Udry et al., 2012; Day et al., 2006) that settled out from the liquid, and the intercumulus phases are within a glassy matrix that hosts sodic plagioclase, silica, phosphate, pyroxene, skeletal titanomagnetite, and pyrrhotite (Udry et al., 2012; Hallis and Taylor 2011) that solidified out of the liquid that was trapped between the cumulus grains (Figure 1).

Figure 1. Reflected light image of MIL090032

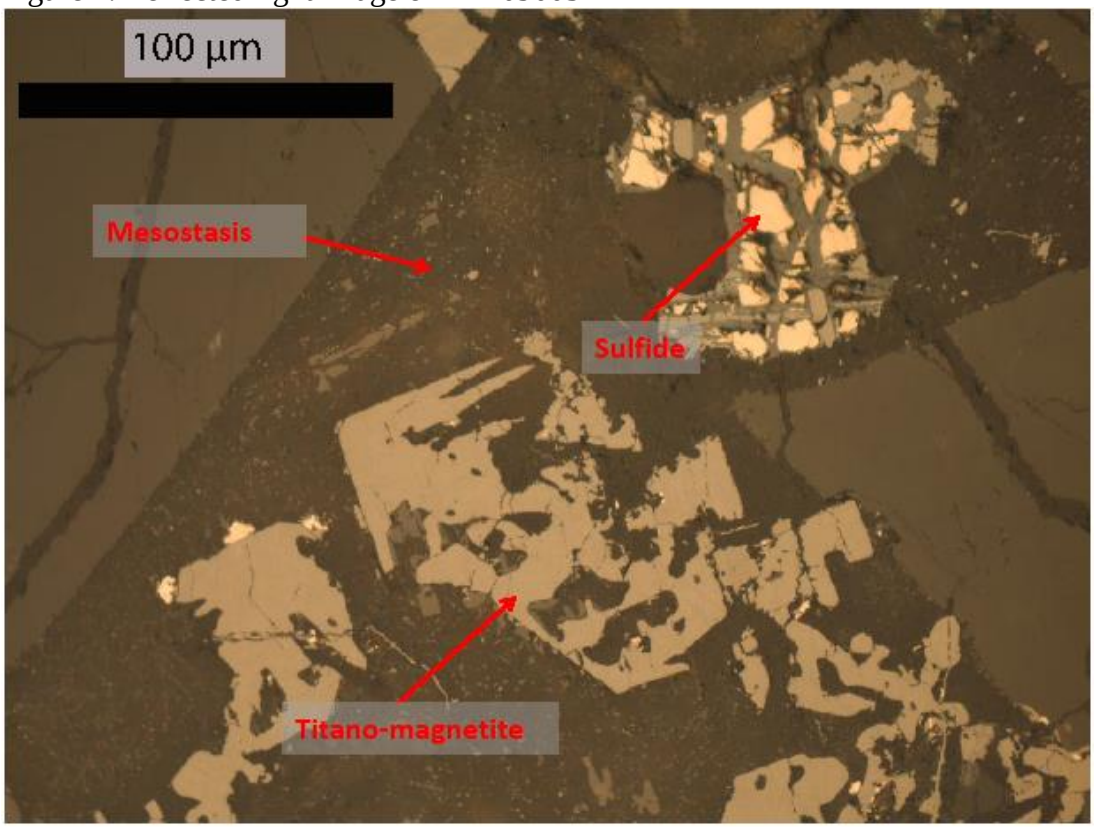

Figure 1. This image displays the presence of small sulfide grains in contact with magnetite grains in the mesostasis of MIL 090032. The mesostasis is enclosed by silicate phases.

2.4 Sulfur isotope notation and basics behind mass-dependence vs. mass-independence

All observed sulfur isotopic analyses are normalized to measurements of CDT using IAEA-S-1 as a secondary standard and S-1 standard. Data are reported as,

$$\delta^{34}S = [(({}^{34}S/{}^{32}S)\text{sample} / ({}^{34}S/{}^{32}S)_{CDT}) - 1] \times 1000$$

$$\delta^{33}S = [(({}^{33}S/{}^{32}S)\text{sample} / ({}^{33}S/{}^{32}S)_{CDT}) - 1] \times 1000$$

$$\delta^{36}S = [(({}^{36}S/{}^{32}S)\text{sample} / ({}^{36}S/{}^{32}S)_{CDT}) - 1] \times 1000$$

$$\Delta^{33}S = \delta^{33}S - 1000 \times (((\delta^{34}S/1000)+1)^{0.515} -1)$$

$$\Delta^{36}S = \delta^{36}S - 1000 \times (((\delta^{34}S/1000)+1)^{1.9} -1)$$

The exponents of 0.515 and 1.91 are the mass dependent relationships of $\delta^{33}S$ and $\delta^{36}S$ where $\delta^{33}S=0.515$ and $\delta^{36}S=1.9$ (Hulston and Thode, 1965a; Hulston and Thode, 1965b). These relationships are termed mass dependent because of the approximate mass differences between isotopes. For example, $\delta^{33}S$ varies as approximately one half (0.515) the variation of $\delta^{34}S$ because the difference in mass between ^{33}S and ^{32}S is .999387 amu which is approximately one half the mass difference of ^{34}S and ^{32}S, 1.995788 amu. The same principles apply for $\delta^{36}S$ seeing that it varies as approximately two times ($\approx$ 1.9) the variation of $\delta^{34}S$ because the mass difference between ^{36}S and ^{32}S is 3.995007 amu. Due to differences in vibrational frequencies and the way energy scales with mass in statistical mechanics (Hulston and Thode, 1965) the exponent in the $\Delta^{33}S$ equation (0.515) deviates from 0.5001. In some cases, sulfur isotopic values have been observed to deviate from the mass-dependent array ((Farquhar et al., 2000; Mojzsis et al., 2003; Ono et al., 2003; Savarino, 2003). Such deviations are termed mass-independent. These deviations from mass-dependence are characterized by non-zero $\Delta^{33}S$ and $\Delta^{36}S$.

Chapter 3: Methods

3.1 Sequential chemical extractions for Martian Meteorites

Sulfur was extracted from MIL 090030/090032/090136 using a sequential chemical extraction protocol similar to that of Kim and Farquhar (2008). Approximately 1 g of whole rock samples were first crushed in an agate mortar and pestle. Once weighed out, they were placed into a 15 ml centrifuge tube and ultrasonicated for 20 minutes with 10 ml of milli-Q water in order to dissolve the water-soluble sulfate. The water-soluble sulfate was precipitated as $BaSO_4$ using $BaCl_2$. The tubes were then centrifuged for 10 minutes in order to separate the solid from the liquid. The solids were then transferred into a single neck round bottom boiling flask. The precipitated solids were then acidified using 5N HCl, releasing acid volatile sulfur (referred to as an AVS extraction).

The round-bottom boiling flask was assembled with a water-cooled condenser, a bubbler filled with Milli-Q water, and a sulfide trap filled with silver nitrate. All joints were sealed with vacuum grease and parafilm. The apparatus was then checked for leaks and lastly purged with nitrogen for at least 10 minutes (the flow of nitrogen gas continues throughout the reaction). For the first extraction in the sequential extraction process, 25 ml of 5N HCl was injected into the boiling flask through a septum with a syringe and needle. The solution was heated to approximately 60 ^{0}C. The AVS extraction extracts monosulfides (i.e. troilite, pyrrhotite, pentlandite, and chalcopyrite) as H_2S gas. When Fe^{3+} is not present, the H_2S is captured in the $AgNO_3$ trap and converted to silver sulfide. Where Fe^{3+} is

present, it is reduced to Fe^{2+}. The reduction of Fe^{3+} to Fe^{2+} yields the production of elemental sulfur by stripping electrons from S^{2-}. The reduction reaction was run for at least 3 hours.

After the first extraction, the sulfide trap was changed and replaced. A mixture of HI, HPO_3 and 12N HCl (Thode Solution; (Thode et al., 1961)) was added through the same septum using a syringe and needle. The solution was then heated to 85 ^{0}C. The thode extraction was shown elsewhere to quantitatively reduce the acid-soluble sulfate from the sample to H_2S (Thode et al., 1961). The reaction was also let run for at least 3 hours. When the reaction was complete, capture tubes were dismantled while the boiling flasks cooled. Once cool the solution in the boiling flask was transferred to 50 ml centrifuge tubes. The contents were then centrifuged and the acid solution was decanted into waste containers. The residual sample was rinsed with Milli-Q water and transferred into a clean single neck round bottom boiling flask for the final extraction.

For the final extraction, a clean apparatus identical to the one described for the first extraction is set up, leak checked, and purged with nitrogen. In the final reduction step, 15 ml of chromium (II) solution and 15 ml of 5N HCl are added to the round bottom flask through a septum using a syringe and needle. The solution is heated to at least 85 ^{0}C and the reaction is run for at least 3 hours.

3.2 Fluorination and Gas Source Mass Spectrometry

Ag_2S captured in the $AgNO_3$ traps were cleaned with Milli-Q and NH_4OH solution and dried in an oven in 1.5 ml eppendorf tubes. The Ag_2S was converted to SF_6 gas through a reaction with fluorine gas in a nickel bomb at approximately 250 ^{0}C

for at least 8 hours. The SF_6 was then transferred from the nickel bomb to a trap cooled with liquid nitrogen. The residual F_2 was passivated by reaction with heated (100 ^{0}C KBr salt. After passivation, the liquid nitrogen on the SF_6 trap was replaced by an ethanol slush (approx. -115 ^{0}C) in order to separate the SF_6 gas from HF and allow for the transfer of the SF_6 into the injection loop of a the gas chromatograph (GC). The Gas chromatograph allows for the purification of the SF_6 by a 1/8-inch diameter, 6-foot long Molecular Sieve GC column, followed by a 1/8-inch diameter, 12-foot long 5A Haysep-Q^{TM} GC column, with helium used as a carrier gas at the flow rate of 20 mL/min. After purification in the GC, the SF_6 was captured in liquid nitrogen cooled metal spiral tubes and transferred into the sample tubes on a glass manifold. The glass manifold was then attached to a Thermofinnigan MAT 253 dual-inlet mass spectrometer. The SF_6 was subsequently transferred into the bellows of the mass spectrometer and sulfur isotopic analyses were conducted. The SF_6 was measured by monitoring SF_5^+ ion beams at *m/z* of 127, 128, 129, and 131 Da.

3.4 Secondary Ion Mass Spectrometry (SIMS) Methods

Three 1" round interior thin sections (MIL 090030,43; MIL 090032,87; MIL 090136,34) allocated by the Meteorite Working Group from the Antarctic meteorite collections were analyzed. The thick sections were gold coated for SIMS analyses. SIMS was used to measure sulfur isotopes in sulfide grains within in the MIL thick sections. Analyses were undertaken at the University of California, Los Angeles using a Cameca SIMS 1270 ion microprobe in multicollector mode. SIMS works by producing a positively charged primary ion beam that impacts the sample surface,

ejecting ionized and neutral atoms and molecular fragments. Negatively charged secondary ions produced by this process are accelerated, focused into and analyzed by a magnetic sector mass spectrometer. Sulfur isotopic compositions are reported in δ and Δ notation (see section 2.4).

The analytical run conditions used for this study include a 5 nA, 20 KeV Cs^+ primary ion beam focused to a 15 micron spot. Before each analysis, the sample was pre-sputtered for approximately 1.5-2 minutes followed by 30 cycles of sputtering of 10-second integrations. A mass resolving power of a~ 4000 and energy filtering was used in order to minimize contributions from the $^{33}SH^+$ ion to the ^{32}S peak. In order to prevent charging of the sample, an electron flood gun was applied to the primary beam. Multiple Faraday cups collected the secondary ions of $^{32}S^-$, $^{33}S^-$, and $^{34}S^-$ after the magnetic sector. A total of 30 spots were analyzed among the three thin sections. Uncertainty for this technique is dependent upon the mineral grain and the primary beam characteristic, which overall affects the number of sulfur ions produced when ionized. The SIMS also produces a mass-dependent fractionation (Instrumental Mass Fractionation) during ionization and transfer to the Faraday and mass-dependent detectors. The fractionations are corrected by normalizing directly to troilite, FeS, the same measured phase observed in the MIL sections.

3.5 X-ray mapping

X-ray maps were collected for the three Miller Range thin sections using wavelength-dispersive spectrometry (WDS) for 5 elements: magnesium, calcium, iron, sulfur, and titanium. Spectral analyses were collected for 30ms and each pixel was 6.4 microns in area. The x-ray maps made for the MIL pairs were divided into

multiple parts, given the shape of the samples in thin section. The dimensions for the x-ray maps are reported in Table 5.

In order to determine modal mineralogy elemental/mineralogical distribution maps were constructed with LISPIX (version LX190P) software. This software aids in the identification and mapping of pyroxene, olivine, magnetite, sulfide, mesostasis and subsequent area determination. Thresholds defined for elements of interest were analyzed using LISPIX to determine the modal distribution of each phase in the MIL pairs thin sections.

In order to determine modal mineralogy elemental/mineralogical distribution maps were constructed with LISPIX (version lispixLX190P) software. A detailed protocol for making the maps are written in the appendix of this thesis. Within the LISPIX software, x-ray maps are uploaded and thresholds are defined in order to highlight phases of interest. I utilized LISPIX in order to identify pyroxene, olivine, magnetite, sulfide, mesostasis and subsequent area determination. Using the x-ray maps described above, the thresholds defined for each phase are displayed in the table below:

Table 5. Thresholds for making modal abundances maps from x-ray maps

X-Ray Map (dimensions in pixels)	Pyroxene	Olivine	Titano-magnetite	Sulfide	Background
MIL 090136 Composite 1 1000 x 1000	Fe = 3-254 Ca = 44-254 Mg = 44-254	Fe = 67-170 Ca = 1-48 Mg = 22-149	Fe = 76-254 Ti = 37-254	Fe = 89-254 S = 32-254	Fe = 1-1
MIL 090136 Composite 2 1000 x 500	Fe = 25-73 Ca = 102-254 Mg = 32-148	Fe = 74-254 Mg = 36-254	Fe = 64-254 Ti = 42-251	Fe = 8-254 S = 62-254	Fe = 1-1
MIL 090030 Composite 1 500 x 1000	Ca = 61-254 Mg = 30-254	Fe = 65-254 Mg = 65-254	Fe = 76-254 Ti = 37-254	Fe = 56-254 S = 39-254	Fe = 1-1
MIL 090030 Composite 2 520 x 300	Ca = 31-254 Mg = 22-254	Fe = 87-254 Mg = 42-254	Fe = 39-254 Ti = 41-254	Fe = 4-254 S = 59-254	Fe = 1-1
MIL 090032 Composite 1 400 x 1000	Ca = 65-254 Mg = 36-254	Fe = 101-254 Mg = 36-254	Fe = 55-254 Ti = 53-254	Fe = 59-254 S = 71-254	Fe = 1-1
MIL 090032 Composite 2 500 x 500	Ca = 115-254 Mg = 55-254	No olivine	Fe = 32-254 Ti = 44-254	Fe = 32-254 S = 32-254	Fe = 1-1

Details on how to make the modal abundance maps using LISPIX are outlined in the appendix (*section v*).

3.6 Electron Microprobe analyses

The composition of pyroxene, olivine, and magnetite grains was determined using the JEOL JXA-8900 Superprobe at the University of Maryland, College Park. WDS analyses were performed under an accelerating potential of 15 keV, a 10 micron beam diameter, a 20 nA current, and a counting time of 20 seconds for iron and sulfur and 30 seconds for all other elements. Thick sections were coated with 200-300 angstroms of carbon and raw x-ray intensities were corrected with a ZAF (Z-atomic number correction, A-absorption correction, F-fluorescence correction) algorithm. The following standards were used for olivine analyses: San Carlos Olivine - Fe, Mg, Si, Ni; Kakanui Augite - Ca, Al; Hypersthene – Cr; Fayalite- Mn; Kakanui Hornblende –Ti. The following standards were used for pyroxene standards:

Kakaknui Hornblende-Fe, Ti; Kakanui Augite - Ca, Mg, Al, Si; Fayalite - Mn; San Carlos Olivine – Ni; Hypersthene – Cr. Uncertainty on analyses are reported in the appendix.

Chapter 4: Results

4.1 Secondary Ion Mass Spectrometry

Figure 2 presents sulfur isotopic data for the 4 MIL pairs 090030/090032/090136/03346 (data tables are reported in the appendix). Plotted are $\delta^{34}S$ values versus $\Delta^{33}S$ values in per mil (‰). The black symbols represent bulk rock analyses from this thesis (published in Franz et al., 2014). Green symbols represent SIMS data from (Franz et al., 2014). Grey symbols represent SIMS data from this thesis. The purple dotted line represents a possible mixing line of sulfide with variable S-Isotopic signatures. Data from SIMS reports average values (with uncertainties reported as 1σ standard deviation) of $\Delta^{33}S$= -0.68‰ ± 0.14, -0.60‰ ± 0.06, -0.76‰ ± 0.15 and $\delta^{34}S$= 14.3‰ ± 1.3, 14.7‰ ± 3.0, 13.7‰ ± 2.8 for MIL 090030/090032/090136 respectively. The average value among all three pairs is $\delta^{34}S$= 14.2‰ ± 2.33 and $\Delta^{33}S$= -0.68‰ ± 0.12. The range of isotopic compositions are as follows (± 1σ): (1) MIL 090030: $\delta^{34}S$= 11.71 to 16.85‰ (± 1.3), $\Delta^{33}S$= -0.79 to -0.32‰ (± 0.1); (2) MIL 090032: $\delta^{34}S$= 11.71 to 19.35‰ (± 3.0), $\Delta^{33}S$= -0.65 to -0.53‰ (± 0.06); (3) MIL 090136: $\delta^{34}S$= 10.40 to 18.35 (± 2.8) ‰, $\Delta^{33}S$= -0.96 to -0.50‰ (± 2.8).

In comparison, the bulk rock values for sulfide as follows: (1) MIL 090030: $\delta^{34}S$= 8.78‰ ±0.15, $\Delta^{33}S$= -0.538‰ ±0.008; (2) MIL 090032: $\delta^{34}S$= 8.85‰ ±0.15, $\Delta^{33}S$= -0.523±0.008; (3) MIL 090136: $\delta^{34}S$= 8.78‰ ±0.15, $\Delta^{33}S$= -0.476‰±0.008. The $\Delta^{33}S$ values are similar to those measured via SIMS. On the contrary, $\delta^{34}S$ values appear less positive.

Figure 2. $\delta^{34}S$ vs. $\Delta^{33}S$ for nakhlites

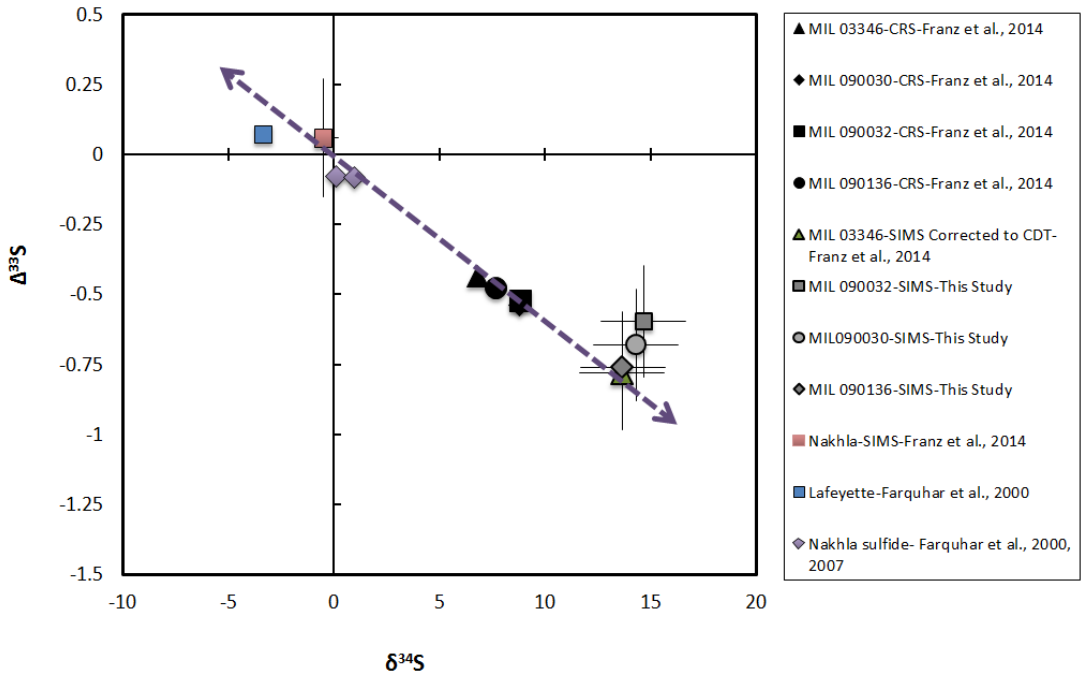

Figure 2. Plot of $\delta^{34}S$ vs. $\Delta^{33}S$ for bulk rock and average SIMS analyses of MIL 03346/090030/090032/09013 and other nakhlites. Bulk analyses on MIL pairs (black symbols) are attributed to (Franz et al., 2014). The SIMS data on MIL 03346 (green triangles) are attributed to (Franz et al., 2014). Additional bulk rock data on Nakhla and Lafayette is attributed to Farquhar et al., 2000, and 2007) All other SIMS points are from this study. Error bars on the SIMS data are reported as 2σ. The error bars on the bulk rock data are within the symbols.

4.2 X-Ray Map Modal Abundances

Modal abundances of pyroxene, olivine, mesostasis, magnetite, and sulfide are displayed in Table 6. A representative map is shown in Figure 3. The largest volume of pyroxene is hosted in MIL 090032. Furthermore, MIL 090032 displays the smallest amount of olivine and sulfide by an order of magnitude. Uncertainty on vol% (in Table 6) of phases was calculated using the method of van der Plas and Tobi

(1965). From modal abundances, we estimate a total of 360 ± 10 ppm S in MIL 090032, and 1300 ppm ± 50 S in MIL 090030 and MIL 090136. Using MIL 090030 as an example, in order to estimate ppm with an associated uncertainty, I used a bootstrap technique in excel. I first used the vol% modes generated using LISPIX in order to generate new randomly generated data sets using the uncertainties from van der Plaus and Tobi (1965). To generate the random numbers for the data sets I used the NORM.INV function in excel. Using the randomly generated modes, I additionally calculated a randomly generated wt% S value using 39.97 ± 1.40 wt% from Day et al. (2006) as the mean value. Next I created another randomly generated data set of phases and their associated densities with uncertainties. The densities were weighted by the mole fraction of endmembers. The combined density of phases was used in order to estimate the density of the whole rock. Using these synthetic density values, I was then able to calculate the ppm S using the following equation:

$$\frac{Vol\%\ of\ S}{density\ of\ the\ rock} * density\ of\ troilite * \frac{wt\ \%\ S}{100} * \frac{1}{100} * 1e^{6}.$$

Uncertainty was estimated by taking the standard deviation of all randomly generated ppm S values. The randomly generated data sets were created 1000 times.

Within this study, interest lies in the magnetite/sulfide vol% ratio, as it is directly related to the plausibility of the formation of magnetite from the reduction of assimilated sulfate upon the emplacement of the flow. MIL 090030 and MIL 090136 reveal magnetite to sulfide vol% ratio of 89%/11%. MIL 0900032 shows a higher magnetite/sulfide vol% ratio of 96.83%/3.17%.

Table 6. Modal Mineralogy of Miller Range Nakhlites

Sample	Total Pixels	Pyroxene	Olivine	Mesostasis	Magnetite	Sulfide
MIL 090030	656000	66.63	8.75	22.45	1.93	0.23
Uncertainty (+/- %)		0.06	0.03	0.05	0.02	0.01
MIL 090032	650000	70.97	1.00	26.07	1.90	0.06
Uncertainty (+/- %)		0.06	0.01	0.05	0.02	0.003
MIL 090136	1500000	60.70	4.91	32.33	1.83	0.23
Uncertainty (+/- %)		0.04	0.02	0.04	0.01	0.004

Uncertainties are reported as 2σ

Figure 3. Representative modal abundance map using LISPIX

Figure 3. The figure above is an image of an X-Ray map of MIL 090136 that has been processed in LISPIX in order to determine the modal mineralogy. The image highlights pyroxene (red), olivine (green), titanomagnetite (yellow), and sulfide (blue). Phases were characterized using Fe, Mg, Ca, S, and Ti. See methods sections for details on technique.

4.3 Electron Probe Microanalyzer Data

Table 7 displays representative major and minor compositions for pyroxene, olivine, and titano-magnetite (all data is presented in appendix). Core-rim analyses on olivine and pyroxene grains exhibit exaggerated zoning at rim/mesostasis boundaries as evidenced in Figure 4 below.

Figure 4. WDS magnesium x-ray map of MIL090030

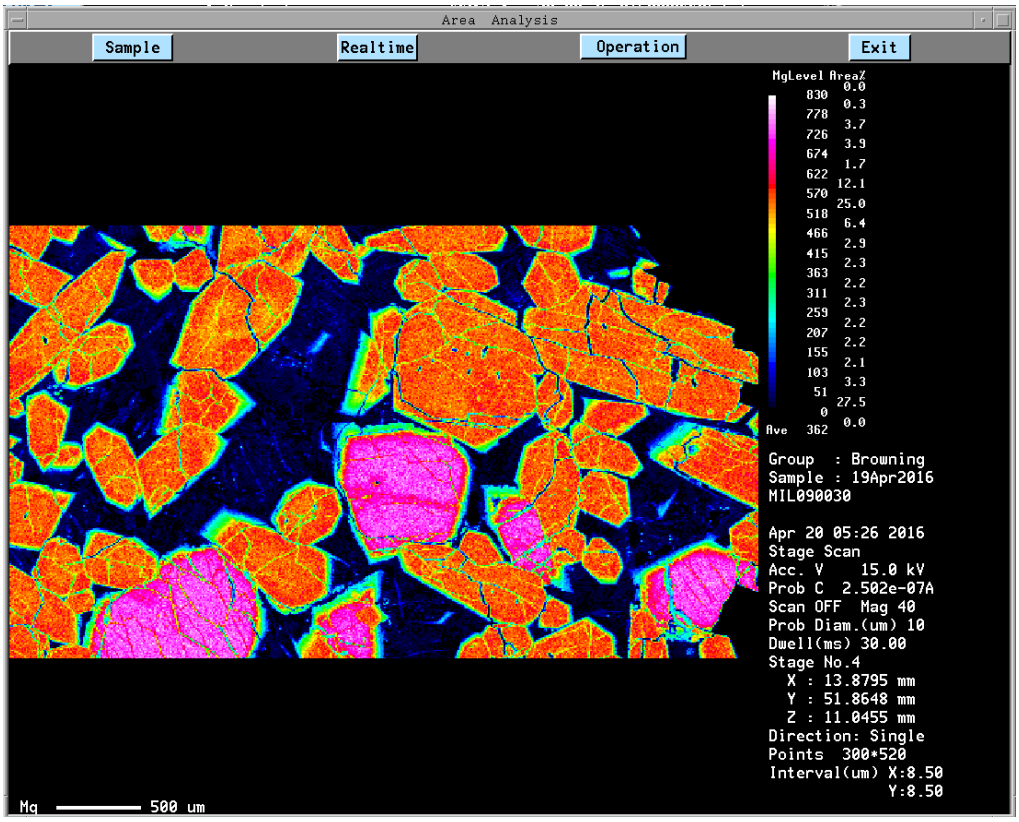

Figure 4. WDS x-ray map of magnesium in MIL 090030 composite 2. Phases rich in magnesium are highlighted in red and pink. Phases low in magnesum are dark blue. The phases visible in this image that are rich in magnesium are pyroxene (red) and olivine (pink). Note the zoning on the rims of pyroxene and olivine.

Rim analyses were taken at pyroxene-olivine junctions, however, exaggerated zoning was not observed. In MIL 090136 the pyroxene cores are in enriched in SiO_2 and MgO relative to the rims. Enrichments are as high as 4 wt% for SiO_2 and 7 wt%

for MgO. Alternatively the cores are depleted in Al_2O_3, TiO_2 and FeO relative to the rims. Depletions are as low as 3 wt% in Al_2O_3, 0.8 in TiO_2, and 7 wt% in FeO. Similarly in MIL 090136 the olivines cores are enriched in SiO_2 and MgO. Enrichments are as high as 4 wt% for SiO_2 and 14 wt% for MgO. The olivine cores in MIL090136 are depleted in FeO relative to the rims where the depletions are as low as 15 wt%. MIL 090032 exhibits similar zoning in pyroxenes as described for MIL 090136. On the contrary, the olivines in MIL 090032 do not exhibit zoning to the same degree as what was observed in MIL 090136. The olivine cores are enriched in MgO by 5 wt% relative to the rims but, no zoning is observed in SiO_2. Additionally the MIL 090032 core is only depleted in FeO by 8 wt%. Similar to MIL 090136 and MIL 090032, MIL 090030 displays similar enrichments and depletions in the pyroxene and olivines with the exception of FeO having a depletion as low as 9 wt% in the core relative to the rim. The olivine cores are enriched in SiO_2 by 3 wt % and MgO by 14 wt%.

The titanomagnetite grains display intergrown olivine and troilite grains, ulvospinel exsolution, and skeletal/elongated structures. From Figure 5, it becomes apparent that the titanomagnetite in the MIL pairs range from a pure magnetite composition to ulvospinel-rich compositions (uvsp ~0 to uvsp ~70). The EPMA data shows that magnetite grains with intergrown olivine have significantly more SiO_2 and almost no TiO_2.

Table 7. Representative EPMA data from MIL090136

Phase	Magnetite				Pyroxene				Olivine		
Comment		Attached to pyx	Attached to Ol	Intergrown FeS	Core	Rim Adjacent to mesostasis	Rim Adjacent to pyx	Rim Adjacent to olivine	Core	Rim Adjacent to pyx	Rim Adjacent to mesostasis
SiO_2	0.27	0.38	0.26	1.21	51.72	47.96	50.05	52.00	34.13	33.82	31.08
Al_2O_3	1.94	2.93	3.10	0.70	0.95	3.05	1.39	0.96	0.05	0.00	0.01
TiO_2	19.24	13.69	18.52	1.12	0.27	0.75	0.37	0.19	0.00	0.00	0.06
FeO	70.43	74.60	71.20	86.00	14.39	24.81	16.11	13.99	45.22	45.54	60.56
MgO	0.20	0.18	0.29	0.13	12.20	5.86	11.23	13.28	19.60	19.32	5.99
MnO	0.71	0.58	0.57	0.27	0.44	0.63	0.42	0.39	0.96	0.95	1.65
CaO	0.05	0.09	0.06	0.17	18.82	17.12	17.74	18.95	0.54	0.59	0.42
Cr_2O_3	0.00	0.02	0.07	0.01	0.23	0.01	0.10	0.40	0.01	0.01	0.00
NiO	0.00	0.00	0.03	0.00	0.03	0.02	0.03	0.06	0.06	0.06	0.04
Total	92.83	92.47	94.08	89.62	99.05	100.21	97.43	100.22	100.56	100.30	99.81

Figure 5. Spinel ternary plot

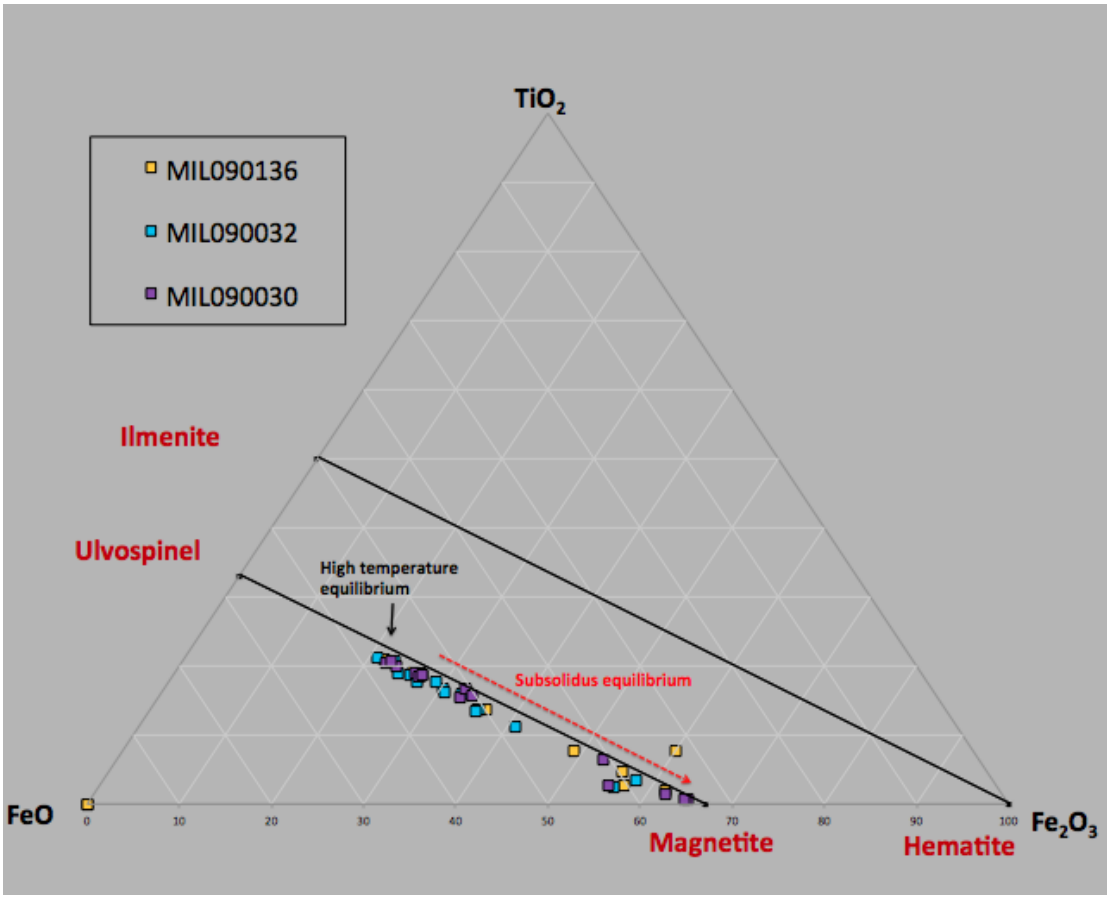

Figure 5. Ternary diagram showing the titano-magnetite composition.

Chapter 5: Discussion

5.1 The oxygen fugacity of the MIL pairs

Petrological evidence such as the presence of high amounts of Fe^{3+} in augite and magnetite, suggests that the MIL 03346 and its pairs are among the most oxidized nakhlites. Dyar et al (2005) report 23% Fe^{3+} in the whole rock and 24% (via Mössbauer spectroscopy) or ~13% (via elemental analysis and crystal chemistry) of total Fe^{3+} in pyroxene in MIL 03346, suggesting an oxygen fugacity of QFM +1.5. McCanta et al. (2009) arrive at a lower, but still oxidized oxygen fugacity estimates of QFM +0.5 for MIL 03346 pyroxenes. Hallis and Taylor (2011) and Udry et al. (2012) describe a mesostasis that consists of mainly glass with plagioclase, quartz, and pyroxene in addition to intercumulus titanomagnetite and sulfides, which is also consistent with an oxygen fugacity near or exceeding QFM.

Here, site assignments and cation charge balance from EPMA data, have been used to determine the Fe^{3+} content in magnetite. These constraints allow use of the oxygen barometer from O'Neill and Wall, (1987), recalibrated by Ballhaus et al. (1990), to determine a log fO_2 value :

$$\log(fO_2)_{P,T} = \log fO_2(FMQ)_{P,T} + 0.27 + \frac{2505}{T} + \frac{0.04P}{T} - 6\log X_{\frac{ol}{Fe}} - \frac{3200}{T}\left(1 - X_{\frac{ol}{Fe}}\right)^2 + 2\log\left(X_{\frac{sp}{Fe^{2+}}}\right) + 4\log\left(X_{\frac{sp}{Fe^{3+}}}\right) + \frac{2630}{T}\left(X_{\frac{sp}{Al}}\right)^2.$$

fO_2 = oxygen fugacity
FMQ= Fayalite Magnetite Quartz buffer
X= mole fraction
P=pressure (GPa)
T=temperature (K)
Ol=olivine
Sp=spinel

Fe=iron
Al=aluminum

Using the composition of magnetite and olivine, this oxybarometer calibration yields an oxygen fugacity of QFM (+3.5 ± 0.4) at the high temperature equilibrium composition of magnetite for MIL 090030/090032/090136, suggesting that the MIL pairs may be even more oxidized than MIL 03346 (QFM +1.5, Dyar et al., 2005), and other nakhlites such as NWA998 (FMQ -0.8), Y-000593 (FMQ -0.7), Nakhla (FMQ) and Lafayette (FMQ +0.1) (see Figure 6) (Szymanski et al., 2010; McCanta et al., 2009; Dyar et al., 2005).

Figure 6. Oxygen fugacity of MIL sulfides relative to the QFM buffer

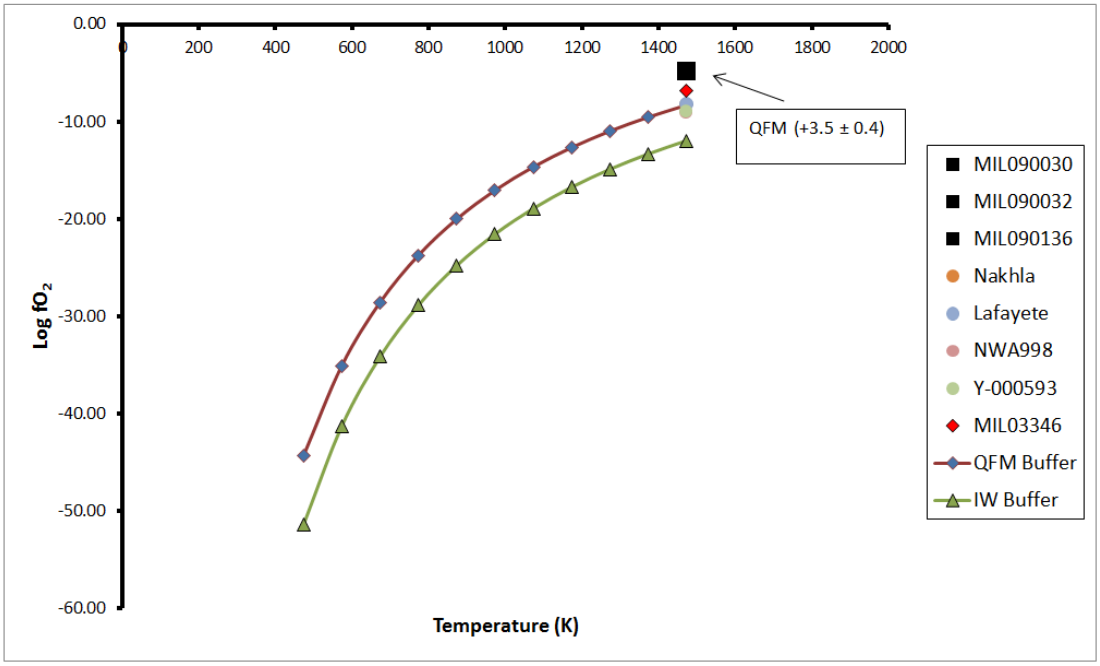

Figure 6. Plot of oxygen fugacity of various nakhlites relative to the QFM and IW buffer. The MIL sulfides are consistent with an oxygen fugacity of QFM +3.5 ± 0.4.

Various studies have explored the reason for the variable oxidation state of nakhlites, and specifically, the higher oxidation state of the MIL pairs. Rutherford et al., (2005) argue the oxidation wasn't a secondary process but rather, that MIL 03346 crystalized in an oxidized parental melt. McCubbin et al. (2009) suggest oxidation occurred at low temperature ($T < 200\ ^0C$) via acidic fluid alteration/weathering processes. Recently, Franz et al., (2014) have argued oxidation via sulfate assimilation and reduction, yielding the oxidation of Fe in the silicate phases.

Here, the hypothesis of oxidation via sulfate assimilation is explored further. The following endmember reactions:

(Rxn. 1) $13FeSiO_3 + CaSO_4 \rightleftharpoons FeS + 4Fe_3O_4 + CaSiO_3 + 12SiO_2$,

(Rxn. 2) $13Fe_2SiO_4 + 2CaSO_4 \rightleftharpoons 2FeS + 8Fe_3O_4 + Ca_2SiO_4 + 12SiO_4$,

(Rxn. 3) $55FeSiO_3 + 2KFe_3(OH)6(SO_4)_2 \rightleftharpoons 4FeS + 19Fe_3O_4 + 55SiO_2 + K_2O + 6H_2O$,

and

(Rxn. 4) $55Fe_2SiO_4 + 4KFe_3(OH)_6(SO_4)_2 \rightleftharpoons 8FeS + 38Fe_3O_4 + 55SiO_2 + 2K_2O + 12H_2O$,

can be used to illustrate how the modal abundance of magnetite that would be produced for the observed sulfide. The volume proportions of magnetite/troilite implied by reactions 1-4 are 91.9%/8.1%, 91.9%/8.1%, 92.2%/7.8%, 92.2%/7.8 respectively.

Image analysis using X-ray maps provide modal abundance data on all major and minor phases in the MIL meteorite pairs (refer to Table 6). The data suggest magnetite/sulfide volume (area) ratios of 89%/11%, 89%/11%, and 97%/3% for MIL 090030, MIL 090136, and MIL 090032 respectively. While variations in the Fe^{3+} of

the mineral phases prevent quantitative comparison with the ratios predicted above, the ratios determined by modal analysis are qualitatively similar to those predicted by the reactions. The difference in modal magnetite/sulfide between MIL 090032 and the other two MIL pairs could result from sample heterogeneity, chemical and physical processes occurring at high temperature, sulfide loss by high temperature degassing, different partitioning of Fe^{3+}, or loss of sulfide to weathering or plucking out of sulfide grains during preparation of the sections. I have observed evidence for sulfide plucked out of the section (see Figure 7), and cannot rule out that the MIL 090032 section experienced more sulfide loss than others.

Figure 7. Reflected light petrographic image of MIL090032

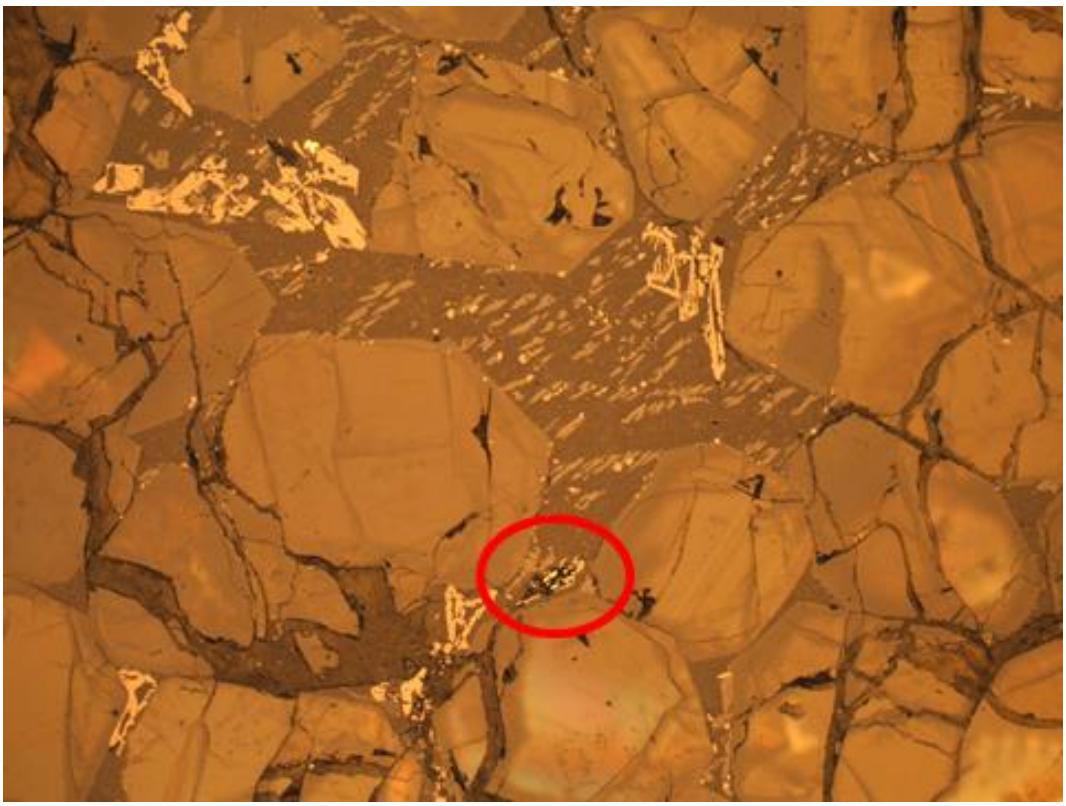

Figure 7. Above is a petrographic image of MIL090032. Note the red circle highlighting the sulfide grain. Most of the sulfide grain appears to be either plucked or scraped out.

Greater than 99% of the total Fe^{3+} is hosted in magnetite grains. The oxygen fugacity estimate of QFM (+3.5 ± 0.4) is higher than those presented in Dyar et al., (2005) (QFM +1.5) and (McCanta et al., (2009) (QFM +0.5) for MIL 03346. Compared to Dyar et al. (2005) who observe 23% of total Fe^{3+} in pyroxene in MIL 03346, my data for MIL090030/090032/090136, reported in table 7, reveal an insignificant fraction of Fe^{3+} in pyroxene and olivine (1% total). The observations made here for the magnetite/sulfide ratios are consistent with reduction of sulfate as the oxidizing process for these MIL pairs, as the reaction of reducing sulfate to sulfide requires a depletion of Fe^{2+} in the silicate phases (e.g. pyroxene) to form magnetite.

5.2 Estimates of Fe^{3+} content and understanding its relationship to S-isotope compositions

5.2.1 Model Background

The electron balance required for reduction of sulfate (to sulfide and possibly sulfur dioxide) is estimated using the ferric iron produced rather than the magnetite mode. The proportion of sulfide added by reduction of sulfate should scale with $\Delta^{33}S$ if sulfide added is properly mixed and not lost. Note, however, the exact relationship the added S and $\Delta^{33}S$ depends on the $\Delta^{33}S$ of the assimilated sulfate, but can be estimated using the Nakhla water soluble sulfate value, of which is interpreted to have been added during post solidification weathering rather than assimilated upon emplacement. The $\delta^{34}S$ of the added sulfide would need to be significantly positive (as observed in the MIL pairs) and might have been produced by a ^{34}S-enrichment

associated with degassing of SO_2 and/or H_2S. The sulfur presently in the samples (~1200 ppm for MIL 090030) must consist of some amount of sulfur introduced with the melt upon eruption (juvenile sulfur), and some proportion of sulfide sulfur added (from reduced assimilated sulfate). However, the amount does not necessarily need to exactly match the amount of sulfate reduced because degassing could play a role. Below, I explore how sulfate reduction, isotope mixing, and degassing are related in the MIL pairs by using a model to evaluate how the electron balance implied by Fe^{3+} can be reconciled with the isotopic balance implied by $\delta^{34}S$ and $\Delta^{33}S$, as well as the material balance of sulfur. Below I have provided a figure (Figure 8) that acts as a road map in understanding processes associated with isotope fractionation.

Figure 8. Roadmap for understanding processes associated with isotope fractionations

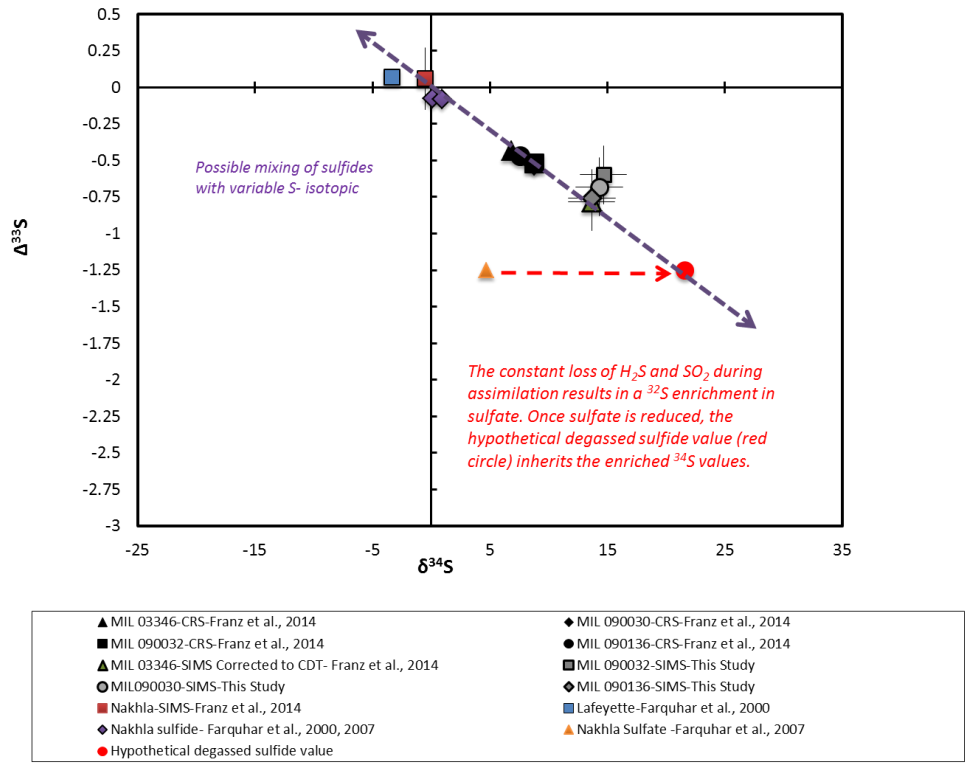

Figure 8. This figure displays $\delta^{34}S$ vs. $\Delta^{33}S$ for bulk rock and SIMS analyses on MIL 03346/090030/090032/09013. This figure explores how the S-isotope signature and sulfide should evolve according to our hypothesis of sulfate assimilation and reduction. I expect a constant loss of H_2S or SO_2 through degassing of the melt (dotted red line). From such degassing, I expect a fractionation in S that would result in sulfide being enriched in ^{34}S, yielding positive $\delta^{34}S$ values (red circle). The purple line with arrows represents a mixing line between MIL pairs, Nakhla and Lafayette sulfide.

5.2.2 Isotope mixing model

Martian meteorites typically display FeO contents of 20 wt% (Lodders 1998), or ~15 wt% Fe. Based on the major element composition of Nakhla (~15 wt% Fe, Lodders 1998) of which we assume is the starting composition of the melt, in order to reach an oxygen fugacity of QFM (+3.5 ± 0.4), 17% of the bulk iron must be oxidized. Such oxidation corresponds to the production of 2.5 wt% Fe^{3+} and, ~650 ppm sulfide S from the reduction of sulfate (6+) to sulfide (2-). Using image analysis, we observe 1300 ± 50 ppm S, 360 ± 10 ppm S, and 1300 ± 50 ppm S in MIL 090030, 090032, and 090136 respectively. Excluding MIL 090032 and considering the amount of S added using constraints from the magnetite grains (~700 ppm S) during assimilation and reduction, the estimated juvenile S concentration is ~ 600 ppm. Such values might be produced if roughly 45% of the original signature of the sulfate contaminant ($\Delta^{33}S$= -1.25‰ Farquhar et al. 2007) were to mix with the assumed juvenile signature ($\Delta^{33}S$=0‰, Franz et al. 2014). Using a simple mass balance ($\Delta^{33}Smix$ (‰) = XA*$\Delta^{33}SA$ + XB*$\Delta^{33}SB$), such mixing results in a $\Delta^{33}S$ value of –0.66‰. This estimate is indistinguishable from the average value measured via SIMS (this study), $\Delta^{33}S$= -0.68±0.12‰ (1 σ). The values of Nakhla water-soluble

sulfate are used as an endmember for these calculations to explore whether the assimilated sulfate could have had a similar composition.

When assimilating sulfate salts, it is expected that the sulfate salts record an S-isotopic signature reflecting its genetic history. Data from SIMS and bulk S isotope data (Franz et al., 2014) verify the presence of S-MIF in the sulfide phase of the MIL pairs, tracking the reduction of sulfates. However, we observe more positive $\delta^{34}S$ values and more negative $\Delta^{33}S$ values for MIL 090030, 090032, 090136 than measured by wet chemistry in Franz et al. (2014). In Figure 2, we observe an array associated with previously measured SIMS and bulk rock data from Franz et al. (2014) and Farquhar et al. (2007) and SIMS data (this study). The array projects through the origin (i.e. through the composition of juvenile S, $\delta^{34}S$= 0‰, $\Delta^{33}S$= 0‰), through sulfide SIMS measurements of Nakhla [endmember 1] and through measurements of the MIL pairs [endmember 2]. The observed array likely reflects a mixing of sulfur isotopic signatures among the nakhlites identified in their sulfide S isotopic composition. Note the more negative $\Delta^{33}S$ from SIMS versus wet chemistry data. We attribute such differences to more negative $\Delta^{33}S$ being hosted in larger sulfide blebs versus sulfide grains that were too small to analyze but were reflected in the bulk isotopic signature. We note that Lafayette may be shifted from the origin with a positive $\Delta^{33}S$ value (Farquhar et al., 2000) and a negative $\delta^{34}S$ (Farquhar et al., 2000). The values for this meteorite ($\delta^{34}S$= -4.3‰, $\Delta^{33}S$=0.071‰ ± 0.051 ‰) are significantly different than the value for juvenile S.

The SIMS data for MIL 090030/090032/090136 extend the array generated by other nakhlite sulfides toward more extreme ^{34}S-enriched S isotopic compositions,

suggesting they have assimilated and reduced the greatest amount of sulfate with S mass independent compositions. Assuming the S-isotope composition in Nakhla sulfate ($\delta^{34}S$= 4.7‰, $\Delta^{33}S$= -1.25‰, Farquhar et al., 2007) was the assimilated signature, we would expect the sulfide in MIL from reduced sulfate to have the same signature. However, as stated above, we had an initial composition of juvenile sulfur of at least ~600 ppm. Thus it is expected that mixing of S-isotope signatures would occur in the sulfide pool, forcing the $\Delta^{33}S$ and $\delta^{34}S$ values towards $\delta^{34}S$ =0 ‰, $\Delta^{33}S$ =0 ‰, the juvenile S signature.

The difference in $\delta^{34}S$ vs. $\Delta^{33}S$ in MIL sulfide ($\delta^{34}S$= 14.2 ‰, $\Delta^{33}S$= -0.679 ‰) vs. Nakhla sulfate ($\delta^{34}S$= 4.7‰ ± 0.2‰, $\Delta^{33}S$= -1.25‰ ± 0.01‰) can be explained by a difference in sulfate source with variable sulfur isotopic composition, as suggested by Farquhar et al. (2007). I explore the possibility that the assimilated sulfate started with the same composition as the late sulfate, but was fractionated by degassing of S-bearing gases during the reduction and assimilation process.

5.2.3 Degassing Model

Previous S-isotope studies on nakhlites report no evidence of degassing in the S-isotope composition. This is possibly due to reports of the melts being under saturated in S. If the melt assimilates sulfate salts, the isotopic composition of sulfide in the melt can be shifted if the sulfate is reduced to SO_2 (or H_2S) that is degassed during the reduction process. The residual sulfate can be enriched in the heavy isotope (^{34}S) from the loss of the light isotope (^{32}S) (Labidi et al., 2015; Mandeville et al., 2009). Continued reduction of sulfate may therefore produce sulfide that is also ^{34}S enriched. Considering that the SO_4-SO_2 fractionation is roughly 2‰ at 1200 °C

(Mandeville et al., 2009) (assuming that the degassing is occurring at this temperature for estimate purposes), degassing of 99% of an SO_2 product in a Rayleigh open system could account for a ~ 10‰ $^{34}S/^{32}S$ positive shift of $\delta^{34}S$ (see Figure 9). Such a shift is comparable in magnitude to that needed to explain the positive $\delta^{34}S$ of the MIL pairs. The amount of degassing suggests approximately 10 times the amount of assimilated S was assimilated, pushing the total S values in the early melt closer to S solubility estimates of ~2000 ppm S (Chevrier et al., 2011).

Figure 9. Modeled SO_2 and H_2S degassing

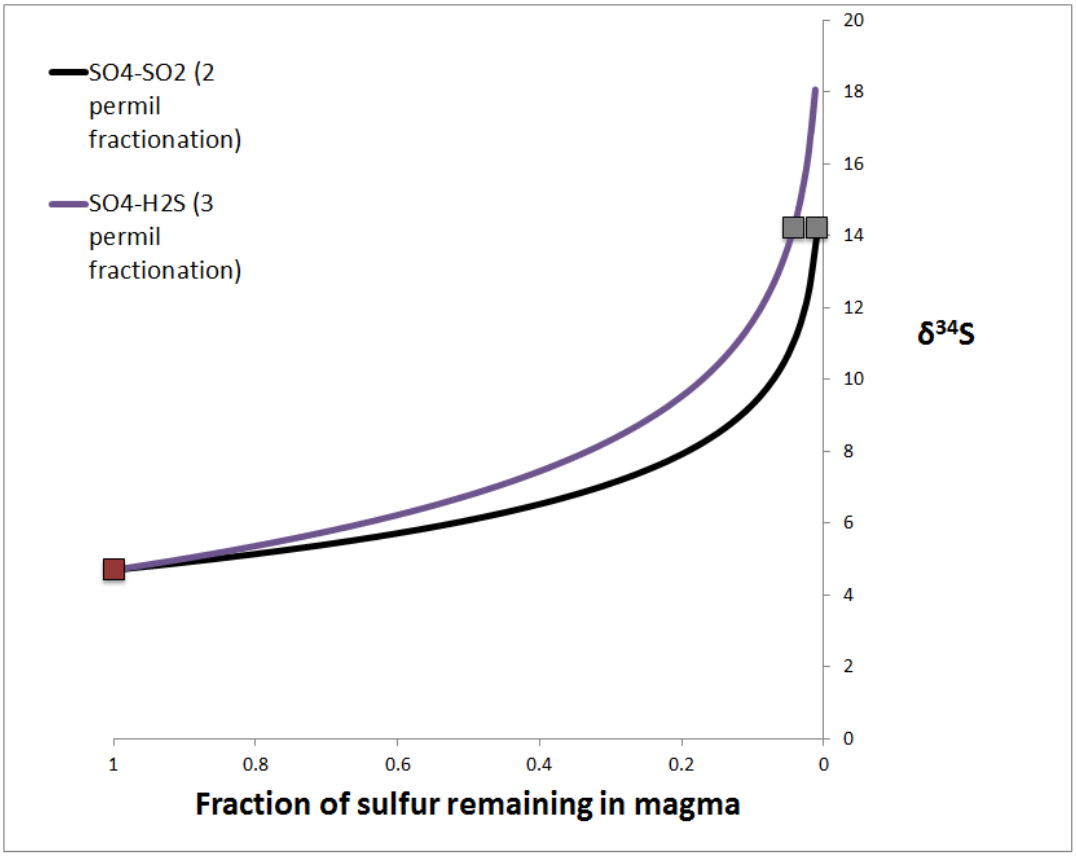

Figure 9. Above represents a model of SO_2 (black line) and H_2S (purple line) degassing from the MIL precursor melt. We assume an initial $\delta^{34}S$ value of 4.7 ‰, the composition of Nakhla (Farquhar et al., 2007). In order to reach the $\delta^{34}S$ values

observed in the MIL sulfides via SIMS (average $\delta^{34}S$ = 14.2 ‰) we estimate a loss of 60% of the SO_2 and 70% during degassing of H_2S.

Note that if instead of SO_2 degassing, H_2S is degassed under equilibrium from sulfate in the melt, the isotopic fractionation between dissolved sulfate and vapor phase is expected at ~3‰ (Mandeville et al., 2009). In this case, 96% of assimilated S would have to be degassed before sulfate reduction to account for the isotopic ~10‰ mismatches between Nakhla sulfate and MIL sulfides for $\delta^{34}S$. The fractionations associated with degassing may not directly match the values predicted by equilibrium because of diffusion limitation or kinetic effects associated with the process.

5.2.4 Combined model of redox, isotope mixing, and degassing

Independently, the mixing model and the degassing model are sufficient in explaining the data. However, when combined, meeting mass and charge balance becomes more difficult. In Table 8 below, I explore 3 possible scenarios that attempt to explain the isotope mass balance when considering reduction/oxidation, mixing, and degassing.

Table 8. Models to explain the S-Isotope data of the MIL Pairs.

Starting Parameters				
	Calculation Summary	MIL 090030	MIL 090032	MIL 090136
Electron balance	Fe^{3+} initial	**2.45E-04**	**2.34E-04**	**2.43E-04**
Electron balance	Sulfate reduced = 8*sulfide +2* Sulfur dioxide	2.45E-04	2.34E-04	2.43E-04
Material balance	Sulfide in rock = sulfide added + sulfide original	**1300**	**360**	**1300**
$\Delta^{33}S$ balance	$\Delta^{33}S$ sulfide = $\Delta^{33}S$ sulfate * (sulfide added + sulfide lost)/(sulfide in rock + sulfide lost)	-0.68	-0.60	-0.76
$\Delta^{33}S$ sulfate		-1.25	-1.25	-1.25
Proportion added from $\Delta^{33}S$		**0.544**	**0.48**	**0.608**
Fractionation factor needed for degassing				
From Juvenile S	15 permil - 2 permil	0.987	0.987	0.987
From added Sulfate S	15 permil - 5 permil	0.99	0.99	0.99

Scenario 1 - Overview: sulfate reduces to SO_2, degasses, reduces to sulfide, and equilibrates with the melt Assumptions reduction. 2. Sulfide is only lost through SO_2 degassing			
Sulfide added (ppm) = proportion * total observed	707	173	790
Initial sulfide (ppm)	593	187	510
Observed sulfide (ppm)	1300	360	1300
electrons from sulfide added	1.77E-04	4.32E-05	1.98E-04
Missing electrons	6.82E-05	1.91E-04	4.54E-05
Sulfur dioxide lost	3.41E-05	9.54E-05	2.27E-05
Sulfir dioxide lost in ppm	1091	3053	726
Sulfate reduced	0.0000562	0.0001008	0.0000474
Fraction degassed	0.989	0.988	0.989
Proportion of sulfur dioxide (assuming all sulfate is reduced	0.607	0.946	0.479
Fractionation factor needed for loss	1.012	1.004	1.017

Scenario 2- Overview: Sulfate reduces, equilibrates, and lastly degasses as SO_2 Assumptions: 1. Assume all electrons go to sulfide and isotope exchange occurs with all sulfide present			
Sulfide produced	980	936	972
Proportion of $\Delta^{33}S$ added	0.54	0.48	0.61
Total sulfide	1801	1950	1599
Initial sulfide	821	1014	627
Sulfide added	479	-654	673
Sulfide lost	501	1590	299
Fraction degassed	0.989	0.988	0.989
Proportion lost	0.51	1.70	0.31
Fractionation factor needed for lost.	1.016	N/A	1.031

Scenario 3 - Overview: Sulfate reduces, degasses as SO_2, and then eqiulibrates with the melt. Assumptions: 1. Assume all electrons go to sulfide, but no juvenile sulfur is lost, only sulfide produced by sulfate reduction degasses			
Sulfide produced (ppm)	980	936	972
Proportion of $\Delta^{33}S$ added	0.544	0.48	0.608
Total sulfide (ppm)	1300	360	1300
Initial sulfide (ppm)	593	187	510
Sulfide added (ppm)	707	173	790
Sulfide lost (ppm)	273	763	182
Sulfate reduced (ppm)	980	936	972
Sulfide lost to degassing	0.278	0.815	0.187
Fraction degassed	0.988	0.989	0.988
Fractionation factor needed for lost sulfide	1.036	1.007	1.058

In the model above, I set three main parameters in order to explore whether the S-isotope data can be explained by a redox plus degassing model. I determine the amount of electrons that are produced and taken up by sulfur using the Fe^{3+} content of the rock which is calculated using data for pyroxene, olivine, magnetite, and the mesostasis (mesostasis FeO was assumed to be similar to that analyzed by Dyar et al. (2005) for MIL 03346). The $\Delta^{33}S$ of sulfide from the MIL pairs is then used to constrain the isotope balance assuming that the $\Delta^{33}S$ of assimilated sulfate is similar to that of water soluble sulfate extracted from Nakhla and that sulfide present before assimilation had a $\Delta^{33}S$ of 0. The change of $\delta^{34}S$ between sulfide from MIL pairs and sulfate from the assimilant is then modeled using a Rayleigh equation for the three scenarios described in table 8 (and below).

In scenario 1, I assume the sulfide added is a product of sulfate reduction and there is a loss of sulfur dioxide. The assimilated sulfate first reduces to SO_2, degasses, and then undergoes an additional reduction to S(2-) in sulfide minerals. The model

calculation results for scenario 1 seem plausible considering the initial S required is comparable to previous estimates. However, scenario 1 (1) requires a significant amount of degassing of SO_2 (726 ppm – 3053 ppm), and (2) a large fractionation factor for MIL 090030 (~ 13 ‰ SO_4-SO_2 fractionation) and MIL090136 (~ 17 ‰ SO_4-SO_2 fractionation).

In scenario 2, I assume that all of the electrons donated go all the way to sulfide minerals and there is a complete isotope exchange with the sulfides. Thus, sulfate is reduced, it equilibrates with the melt and then later degasses as SO_2. Scenario 2 does not work. The amount of juvenile S required to fulfill the scenario is too high to be reasonable. Note MIL 090032 requires a negative amount of juvenile S and MIL 090030/090136 require amounts > 600 ppm S. This suggests that if degassing of sulfide occurred, there was a separation of sulfide originally in the melt and sulfide produced from reduction of sulfate.

Lastly, in scenario 3, I again assume all of the electrons go to sulfide, but no juvenile S is degassed; only S produced from sulfate reduction was degassed. The sulfate is reduced, it equilibrates with the melt, and then degasses. Scenario 3 could work considering the amount of juvenile S is comparable to previous estimates and the amount degassed is comparable or less than the amount that was added during assimilation. On the other hand, the fractionation factors required to meet the difference in $\delta^{34}S$ between Nakhla and the MIL pairs are larger than expected, suggesting (like in scenario 1) that the starting (or assimilated) $\delta^{34}S$ composition was more positive than that observed in Nakhla.

This analysis suggests that the reduction of sulfate, coupled with the oxidation of Fe^{2+}, played a significant role in the late magmatic evolution of the MIL pairs but, the isotopic composition of assimilated sulfur was not produced by degassing of sulfide or sulfur dioxide using any reasonable estimates of fractionation factors. This would also be consistent with the argument that sulfur did not reach saturation in the melts as a result of sulfate assimilation. Assimilation of a ^{34}S-enriched, anomalous sulfate component that is different than that seen in Nakhla also provides a way to produce the straight array observed in figure 2.

5.3 A discussion of the location of MIL within the nakhlite melt

The depth of various nakhlites within the nakhlite cumulate has been a subject of discussion. Some (e.g. Mickouchi et al., 2006) have placed MIL 03346 at the top of the flow and Nakhla in the middle. On the contrary, other studies (e.g. Richter et al., 2016) place MIL 03346 at the base of the flow assuming that rapid cooling rates are better explained by bottom cooling. In light of the two conflicting arguments I explore the two possibilities in the context of the information provided in this thesis.

Our data show a negative $\Delta^{33}S$ signature (in sulfide or reduced sulfate) in the MIL pairs relative to Nakhla sulfide and an even more negative $\Delta^{33}S$ in Nakhla sulfate relative to MIL sulfide. In the context of arguments for "base of flow" crystallization, the base appears to be a more likely environment for assimilated anomalous sulfate. However, note that Nakhla also demonstrates having an anomalous sulfide fraction (Farquhar et al., (2000, 2007)), suggesting Nakhla may have been above MIL in the flow. Thus, Nakhla would demonstrate less reducing conditions in the form of anomalous sulfate and sulfide.

When considering arguments for "top of flow" crystallization, the incorporation of S-MIF is no longer done through assimilation upon emplacement but rather incorporation from the raining out of sulfate salts. In this scenario it is no longer the base that is the portion of the flow that gets SO_4^{2-}, it is the top of the flow that is more reducing. Similar to the last scenario, Nakhla would be adjacent to MIL so that the anomalous sulfate could easily be incorporated in a less reducing environment. That being said, considering the amount of sulfate needed to oxidize the MIL pairs to QFM +3.5 ± 0.4 is much higher than what appears likely for the process of raining out sulfate salts onto the flow. The sulfur isotope evidence points more strongly towards "base of flow" crystallization.

Chapter 6: Conclusion

A summary of the arguments presented in this thesis is illustrated Figure 10. We observe an anomalous S-isotope signature hosted in the sulfide phase of the MIL nakhlites that is demonstrative of reduction-oxidation processes in the melt. The redox reactions involving sulfate provide a good explanation for the presence of high amounts of ferric iron (yielding an fO_2 of QFM +3.5 ± 0.4) and can account for most of the ferric Fe (2.34E-04 to 2.45E-04). However, there appears to be an electron imbalance, which in the absence of S- degassing requires assimilation of an additional oxidant such as perchlorate, chlorate, nitrate, or hydrogen-peroxide (Chevrier and Mathé, 2007; Dehouck et al., 2016; Kounaves et al., 2014). Models presented in this study were not capable of reconciling the $\delta^{34}S$ with a degassing model and imply assimilated sulfate had a different $\delta^{34}S$ than late sulfate extracted from Nakhla.

However, some loss is allowed. This implies a degree of geographic or temporal variability in the $\delta^{34}S$ of sulfate on Mars.

The processes of assimilation and redox require a position in the nakhlite cumulate flow for MIL that is conducive for assimilation of sulfate. Given the amounts of sulfate assimilated, it seems more likely that salts are being assimilated from soils beneath the flow, rather than incorporating rapidly deposited anomalous atmospheric sulfate at the top of the nakhlite flow. I propose a stratigraphy that is different from what was proposed by Mikouchi et al., (2006) who place MIL at the top of the nakhlite flow. In agreement with Richter et al., (2016), I place MIL at the base of the nakhlite cumulate flow.

Figure 10. Summary of arguments

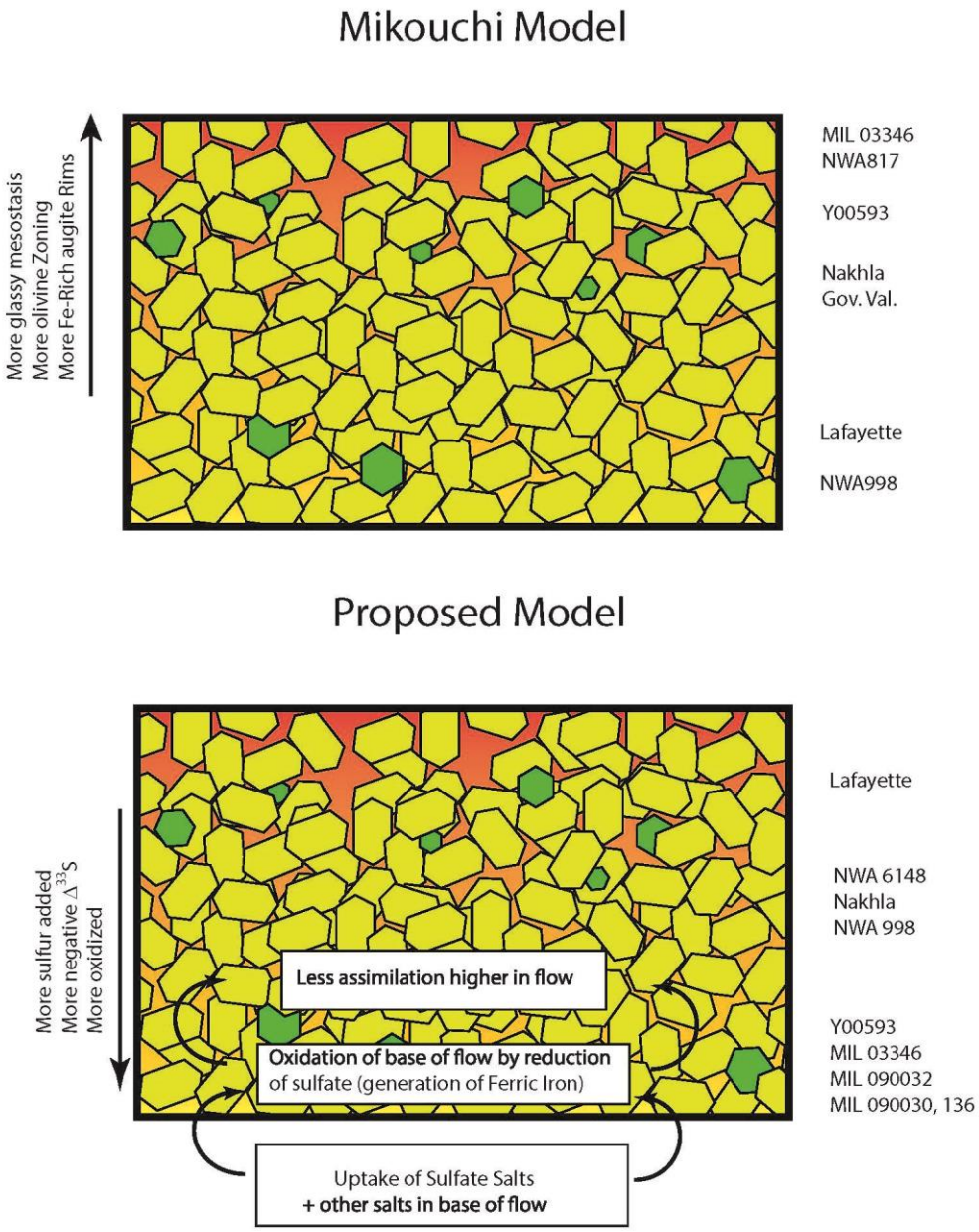

This study examined the source of oxidation in MIL 090030/090032/090136/03346 and constrained the role of sulfate assimilation and

reduction as a cause of oxidation of the MIL pairs. Assimilation and reduction of SO_4^{2-} yields troilite and magnetite. The S-isotope composition of sulfides measured via SIMS (this study) and sequential acidifications of whole rock samples (conducted for this thesis, published in Franz et al., (2014)) yield a negative $\Delta^{33}S$ for the sulfide phase of which results from the reduction of sulfate with an anomalous $\Delta^{33}S$.

Previous studies have stated the MIL pairs are the most oxidized nakhlites among all nakhlites (Udry et al. 2012). Estimates in this study suggest an oxygen fugacity of QFM +3.5 ± 0.4, the highest fO_2 recorded for nakhlites studied to date. In order to reach such high oxygen fugacity, we estimate the addition of ~700 ppm S (in the form of sulfate that is then reduced) and a juvenile S content of ~ 600, considering total sulfide content estimates using image analysis (~1300 ppm S). The addition of S with a mass-independent signal to a melt with juvenile mass-dependent sulfur generates a mixing array that passes through the origin with Nakhla (Franz et al. 2014), other Nakhlites, and the MIL pairs (this study) defining a series with progressive addition of a negative $\Delta^{33}S$ and positive $\delta^{34}S$ component. Tests that assume the assimilated sulfur isotopic composition was that of water –soluble sulfate in Nakhla ($\Delta^{33}S$ = -1.25‰ ± 0.01‰, Farquhar et al., (2007)) that was fractionated by degassing of SO_2 and H_2S from the melt suggests another process was responsible for the ^{34}S enrichment seen in the added sulfur. To balance the electrons from sulfate reduction, degassing is not supported as a viable explanation and suggests that the assimilated sulfate had a high $\delta^{34}S$ that is constant through the nakhlites except Nakhla.

The S-isotope data, fO_2 values, and degassing estimates are vital in testing the feasibility of sulfate assimilation and reduction that ultimately caused the oxidation of the MIL pairs. The results strongly imply the assimilation of sulfate salts on the Martian surface was vital in the oxidation of the MIL nakhlites. Future work for this study should involve analyzing the S-isotope composition of nakhlites such as NWA 10153. Righter et al., 2016 suggest NWA 10153 possibly samples a more enriched mantle source or underwent crustal assimilation upon eruption of the melt. It would be interesting to see where NWA 10153 plots in S-isotope space relative to the other nakhlites in order to see if I observe similar interpretations to that suggested by Righter et al. (2016).

Additionally, a more in depth characterization will aid in understanding the causes of S-isotope heterogeneities among all the nakhlites and other Martian meteorite groups. It remains a possibility that the MIL pairs assimilated an S-isotope signature different from that observed in Nakhla. Additional analyses may reveal better constraints on the assimilated signature. As more powerful mass spectrometers become available, I see it as important to reanalyze nakhlites such as Lafayette and Nakhla in order to decrease the uncertainties on the measurements and reassess arguments for location within the nakhlite cumulate pile based on S-isotope evidence.

Appendices

i. X-Ray Maps

Figure 11. MIL090030 composite 1-calcium x-ray map

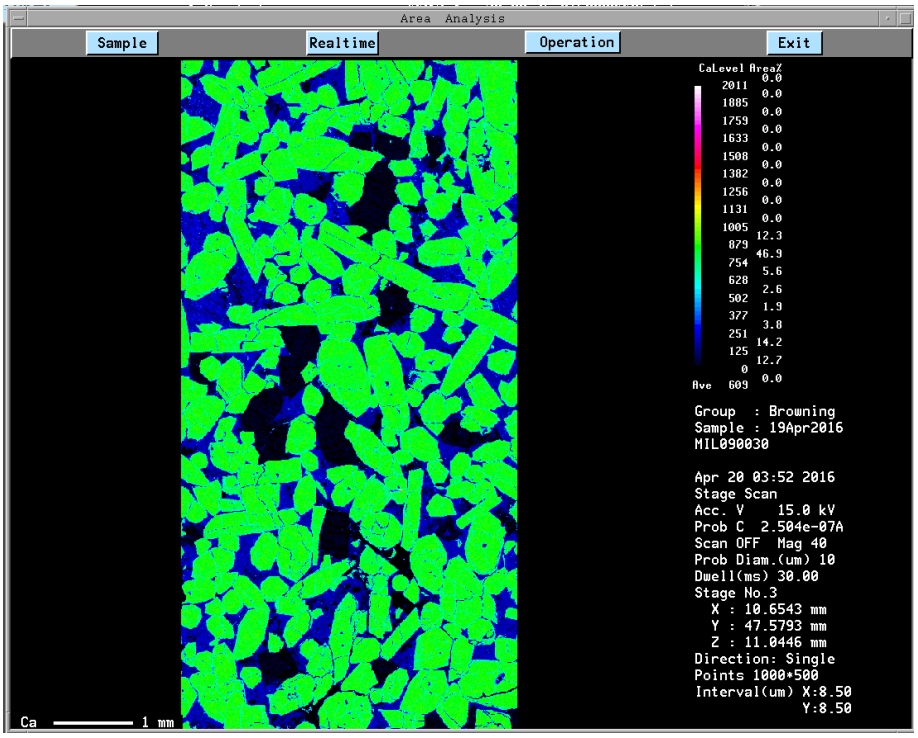

Figure 11. WDS x-ray map of calcium in MIL 090030 composite 1. Phases rich in calcium are highlighted in green. Phases low in calcium are blue. The calcium rich phase is pyroxene.

Figure 12. MIL090030 composite 2-calcium x-ray map

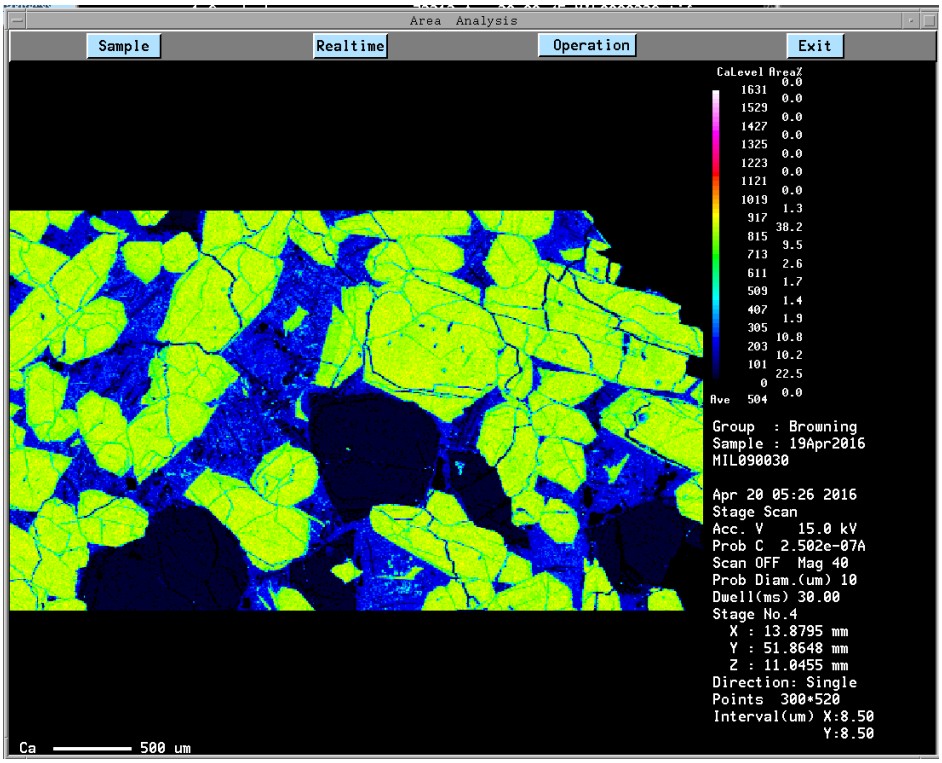

Figure 12. WDS x-ray map of calcium in MIL 090030 composite 2. Phases rich in calcium are highlighted in green/yellow. Phases low in calcium are blue. The calcium rich phase is pyroxene.

Figure 13. MIL090030 composite 1- iron x-ray map

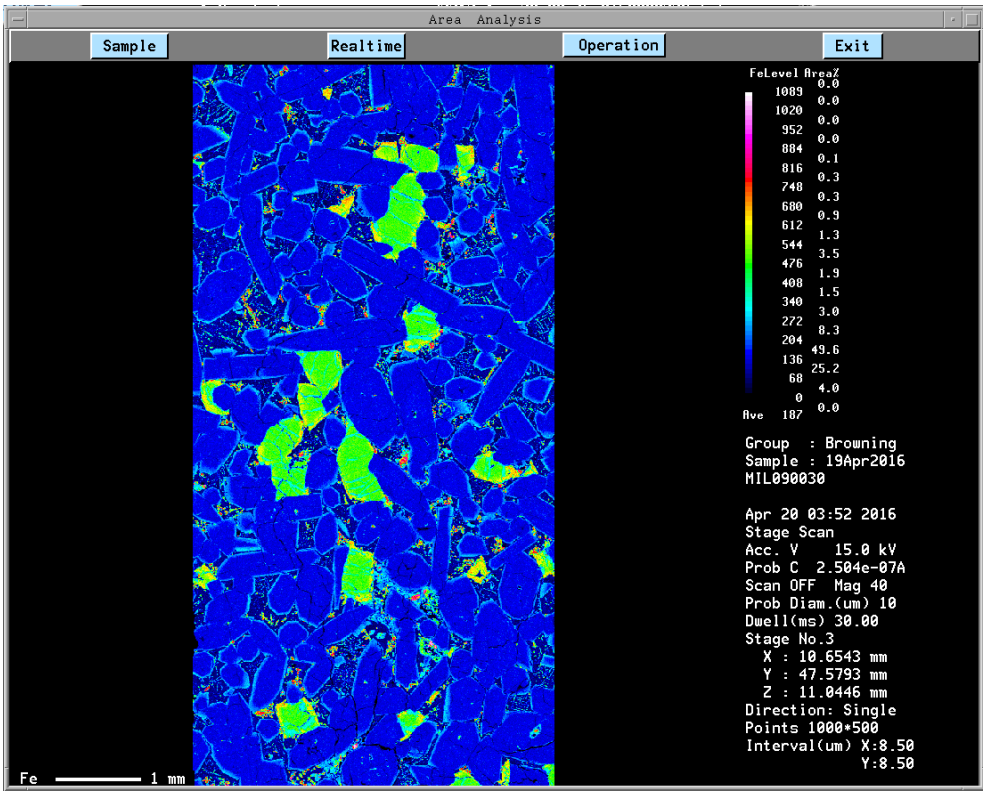

Figure 13. WDS x-ray map of iron in MIL 090030 composite 1. Phases rich in iron are highlighted in green/yellow and pink/red. Phases low in iron are blue. The phases visible in this image that are rich in iron are olivine and titanomagnetite. Note the iron rich rims on the pyroxene (blue).

Figure 14. MIL090030 composite 2 - iron x-ray map

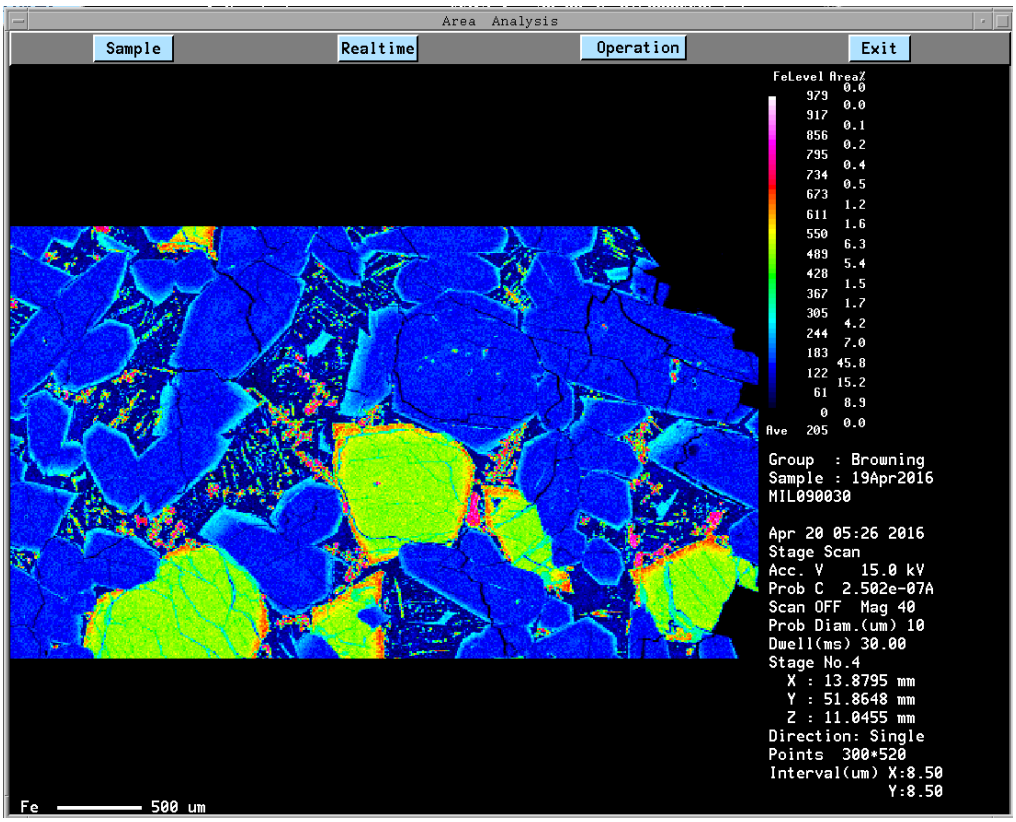

Figure 14. WDS x-ray map of iron in MIL 090030 composite 2. Phases rich in iron are highlighted in green/yellow and pink/red. Phases low in iron are blue. The phases visible in this image that are rich in iron are olivine and titanomagnetite. Note the iron rich rims on the pyroxene (light blue) and the olivine (red).

Figure 15. MIL090030 composite 1 - magnesium x-ray map

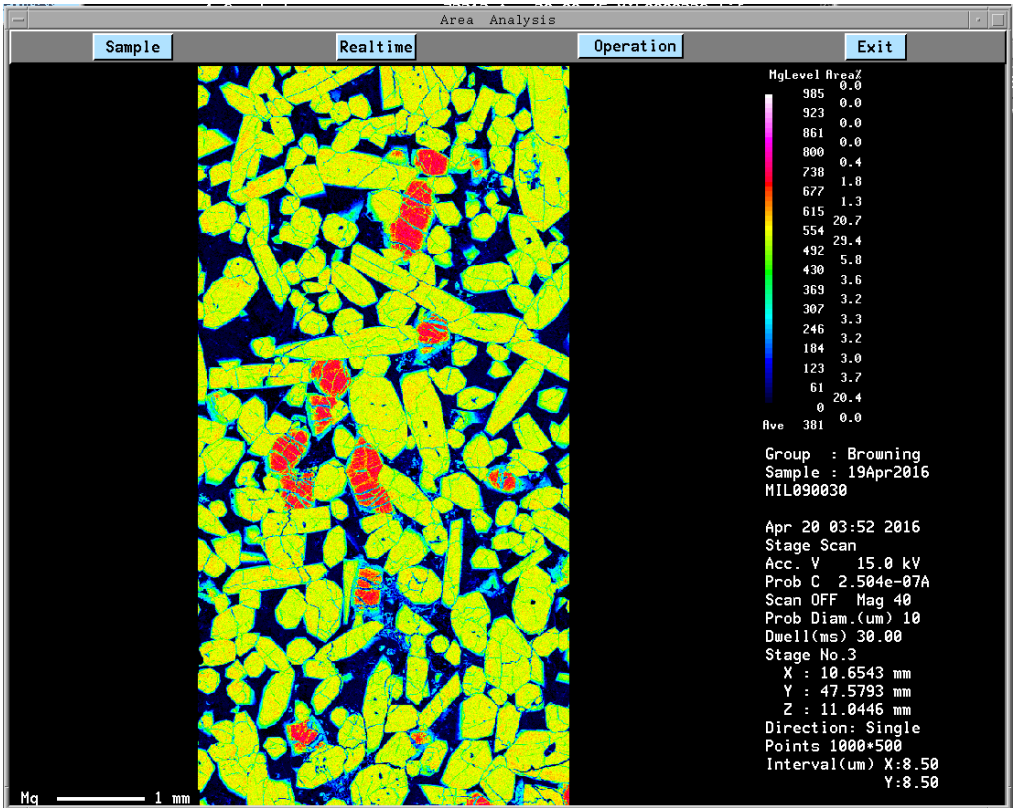

Figure 15. WDS x-ray map of magnesium in MIL 090030 composite 1. Phases rich in magnesium are highlighted in yellow and red. Phases low in magnesum are light blue. The phases visible in this image that are rich in magnesium are pyroxene (yellow) and olivine (red).

Figure 16. MIL090030 composite 2 - magnesium x-ray map

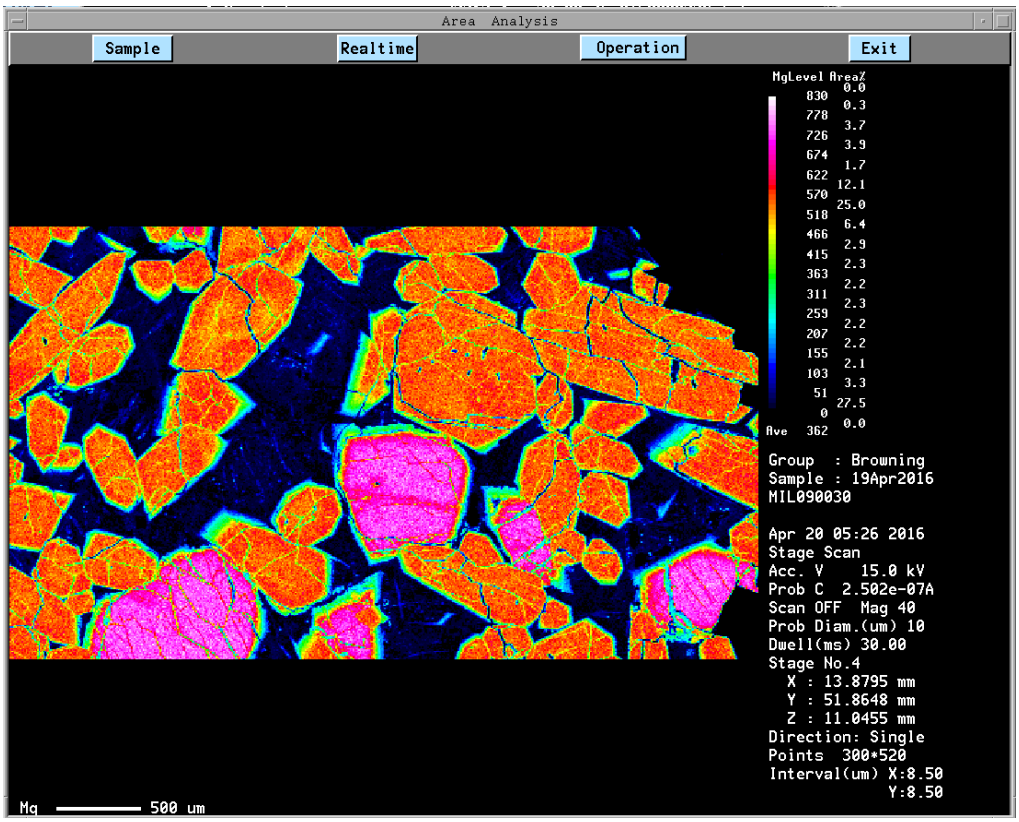

Figure 16. WDS x-ray map of magnesium in MIL 090030 composite 2. Phases rich in magnesium are highlighted in red and pink. Phases low in magnesum are dark blue. The phases visible in this image that are rich in magnesium are pyroxene (red) and olivine (pink). Note the zoning on the rims of pyroxene and olivine.

Figure 17. MIL 090030 composite 1 - sulfur x-ray map

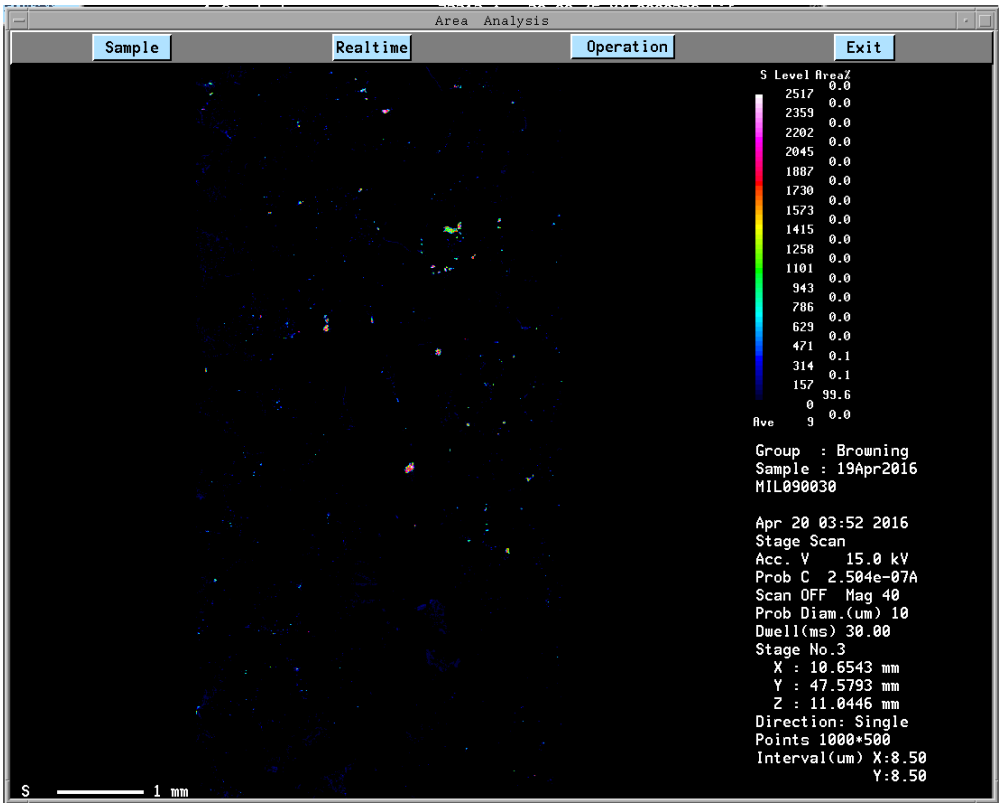

Figure 17. WDS x-ray map of sulfur in MIL 090030 composite 1. Phases rich in sulfur are highlighted in green and red. Phases low in sulfur are dark blue. The phase visible in this image that is rich in sulfur is troilite.

Figure 18. MIL090030 composite 2 - sulfur x-ray map

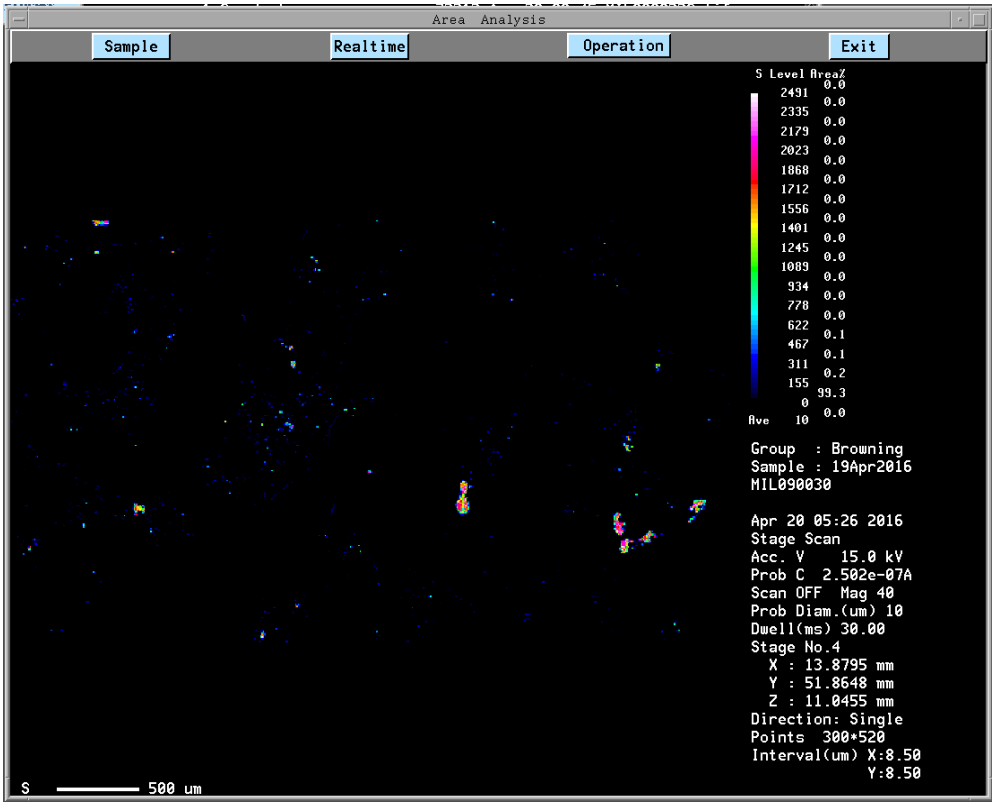

Figure 18. WDS x-ray map of sulfur in MIL 090030 composite 1. Phases rich in sulfur are highlighted in green and red. Phases low in sulfur are dark blue. The phase visible in this image that is rich in sulfur is troilite.

Figure 19. MIL090030 composite 1 - titanium x-ray mapsMIL090030-Titanium

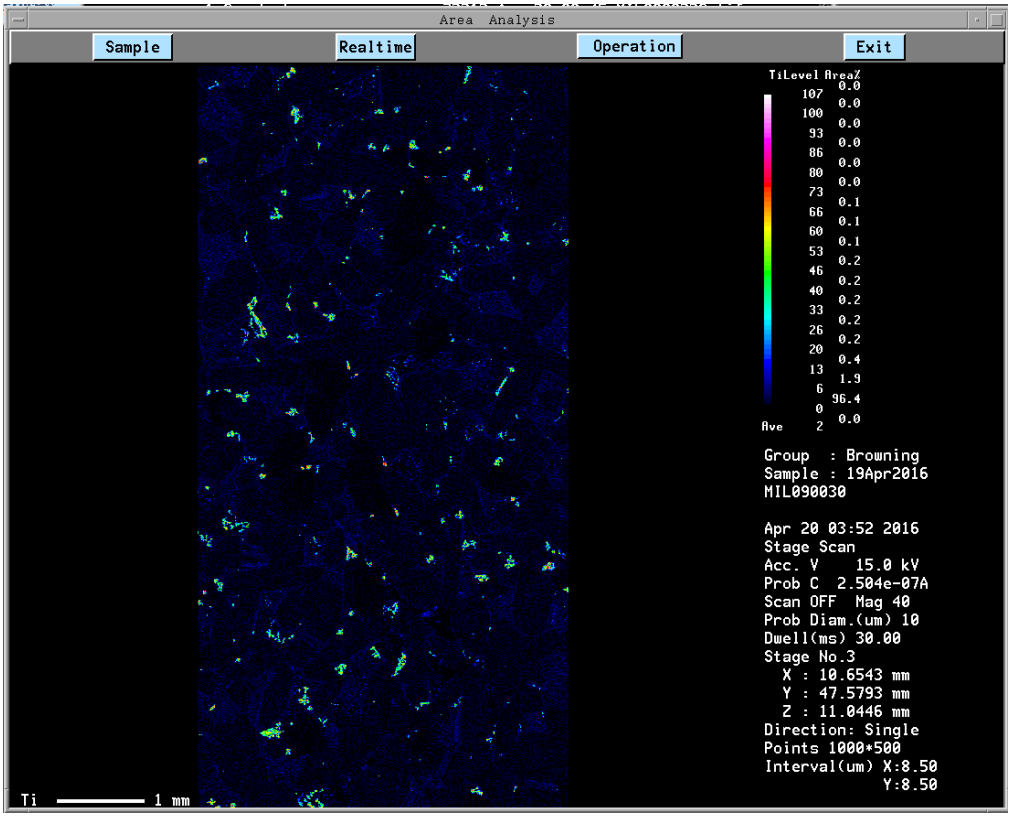

Figure 19. WDS x-ray map of titanium in MIL090030 composite 1. Phases rich in titanium are highlighted in green. Phases low in titanium are dark blue. The phase visible in this image that is rich in titanium is titanomagnetite.

Figure 20. MIL090030 composite 2 - titanium x-ray map

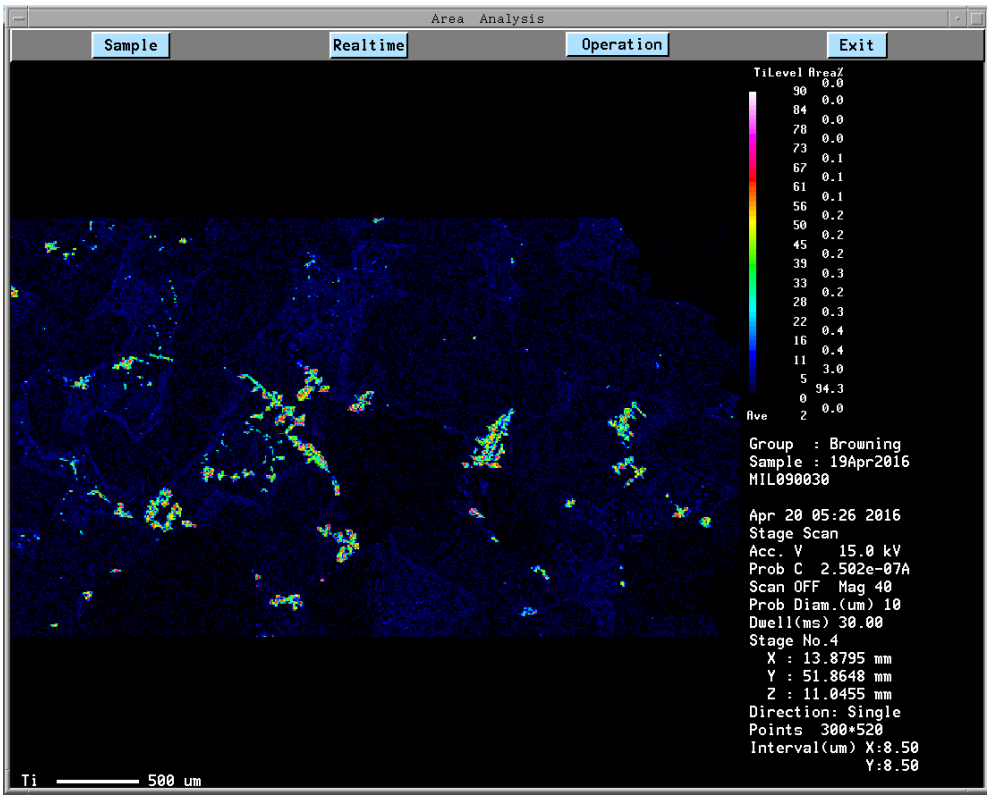

Figure 20. WDS x-ray map of titanium in MIL090030 composite 2. Phases rich in titanium are highlighted in green. Phases low in titanium are dark blue. The phase visible in this image that is rich in titanium is titanomagnetite.

Figure 21. MIL090032 composite 1 - calcium x-ray map

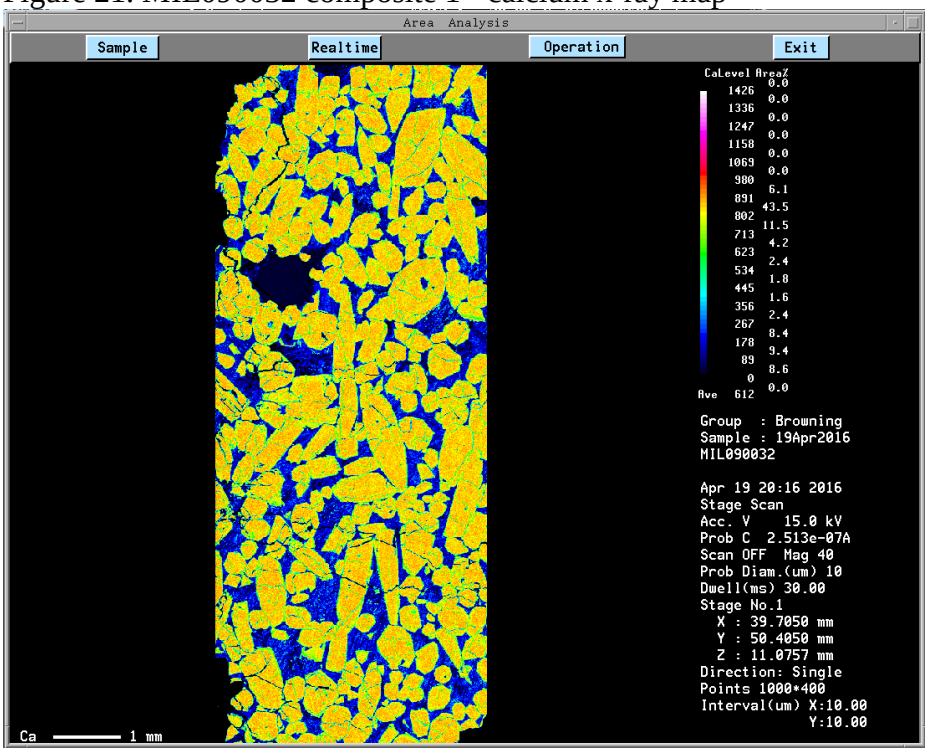

Figure 21. WDS x-ray map of calcium in MIL 090032 composite 1. Phases rich in calcium are highlighted in yellow. Phases low in calcium are blue. The calcium rich phase is pyroxene.

Figure 22. MIL090032 composite 2 - calcium x-ray map

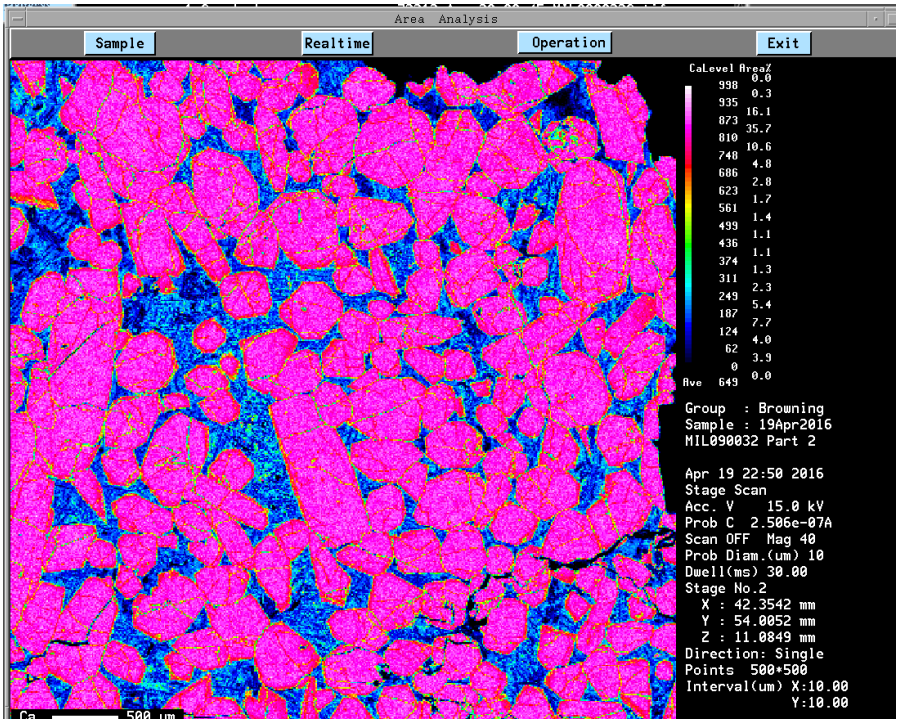

Figure 22. WDS x-ray map of calcium in MIL 090032 composite 2. Phases rich in calcium are highlighted in pink. Phases low in calcium are blue. The calcium rich phase is pyroxene.

Figure 23. MIL090032 Composite 1 - iron x-ray map

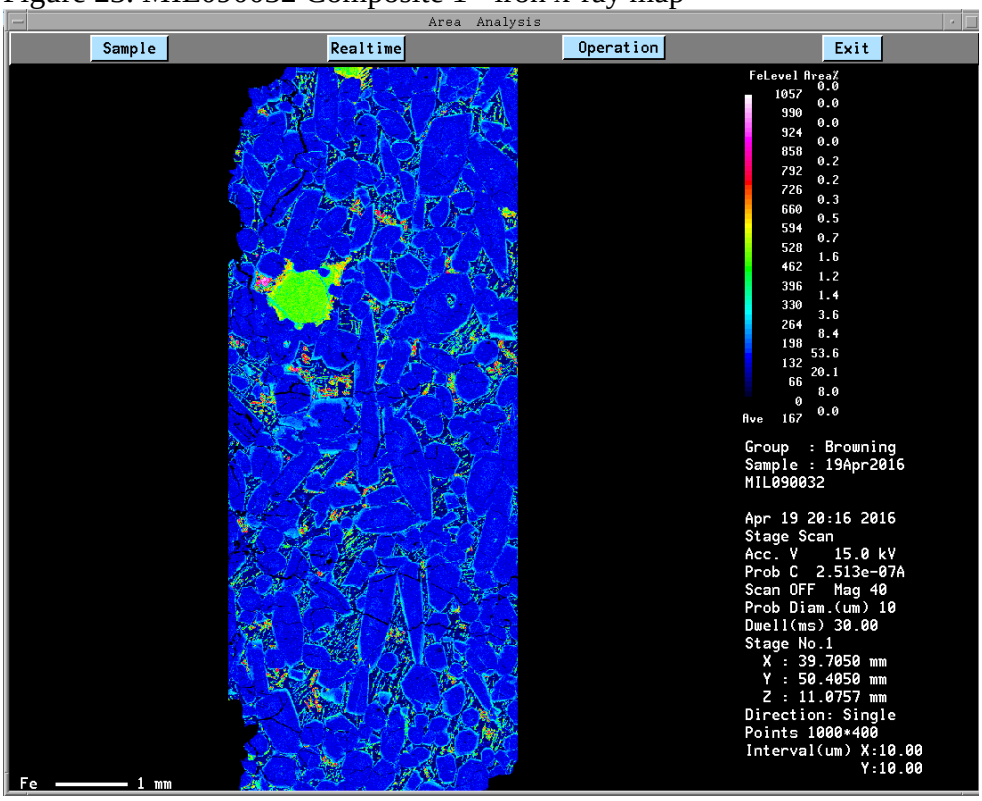

Figure 23. WDS x-ray map of iron in MIL090032 composite 1. Phases rich in iron are highlighted in green/yellow and pink/red. Phases low in iron are blue. The phases visible in this image that are rich in iron are olivine and titanomagnetite. Note the iron rich rims on the pyroxene (blue).

Figure 24. MIL090032 composite 2 - iron x-ray map

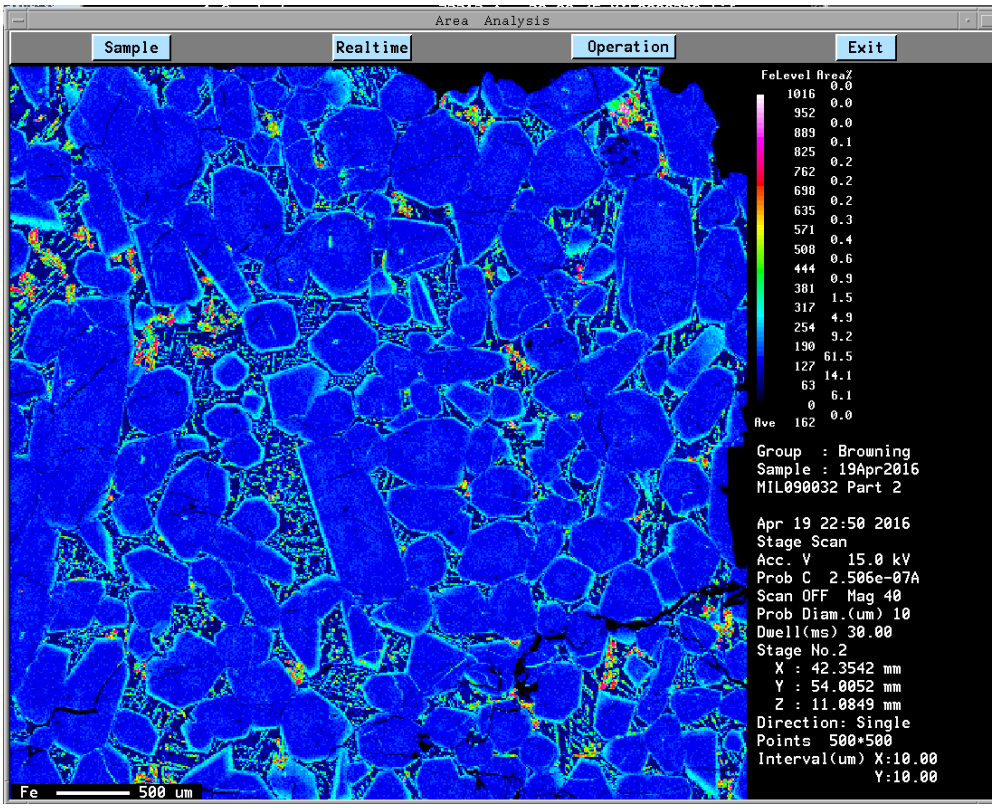

Figure 24. WDS x-ray map of iron in MIL090032 composite 1. Phases rich in iron are highlighted in green/yellow and pink/red. Phases low in iron are blue. The phases visible in this image that are rich in iron are olivine and titanomagnetite. Note the iron rich rims on the pyroxene (blue).

Figure 25. MIL090032 composite 1 - sulfur x-ray map

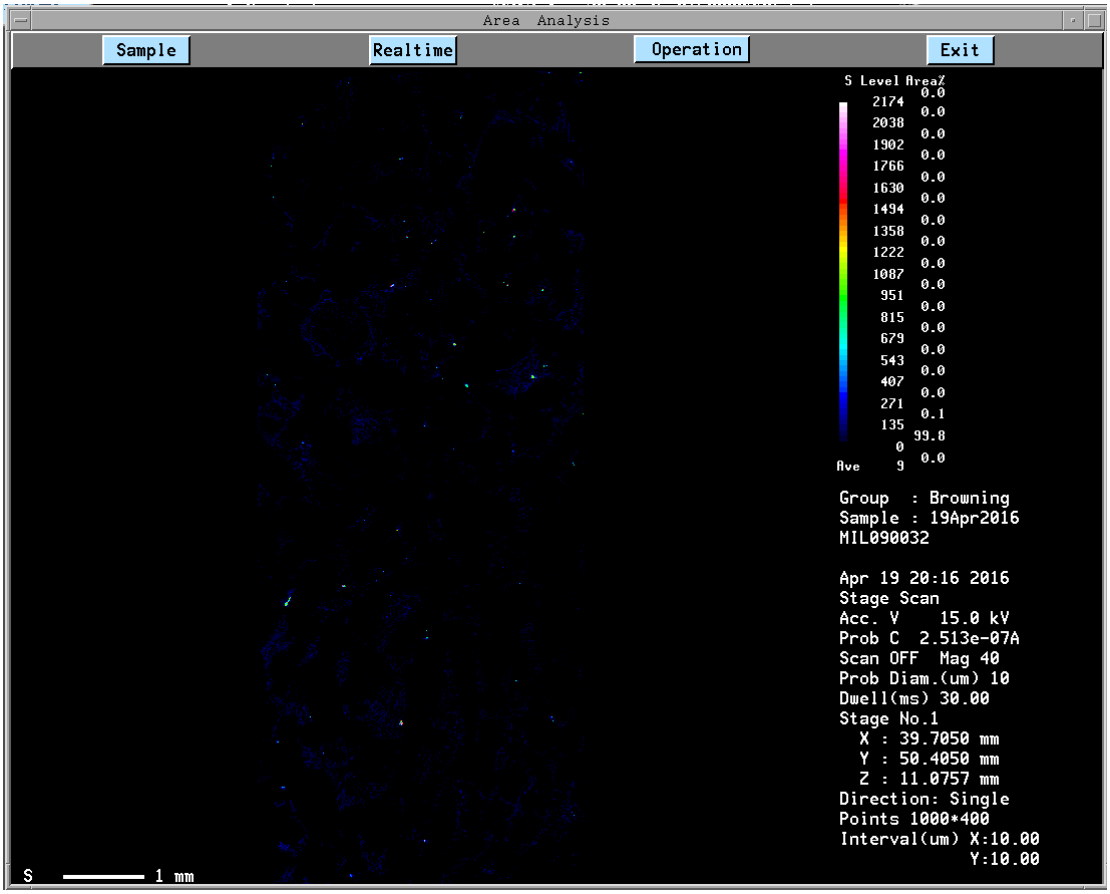

Figure 25. WDS x-ray map of sulfur in MIL090032 composite 1. Phases rich in sulfur are highlighted in green and red. Phases low in sulfur are dark blue. The phase visible in this image that is rich in sulfur is troilite.

Figure 26. MIL090032 composite 2 - sulfur x-ray map

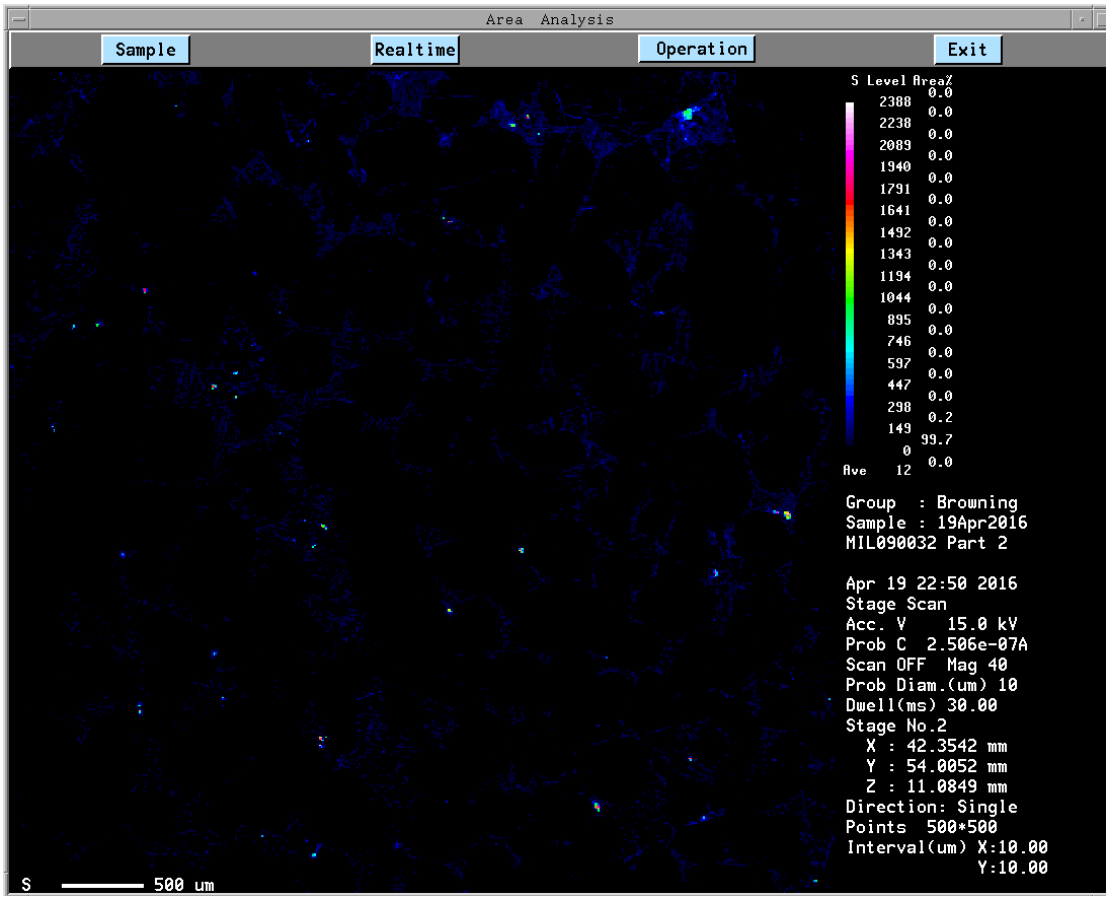

Figure 26. WDS x-ray map of sulfur in MIL090032 composite 2. Phases rich in sulfur are highlighted in green and red. Phases low in sulfur are dark blue. The phase visible in this image that is rich in sulfur is troilite.

Figure 27. MIL090032 composite 1 – magnesium x-ray map

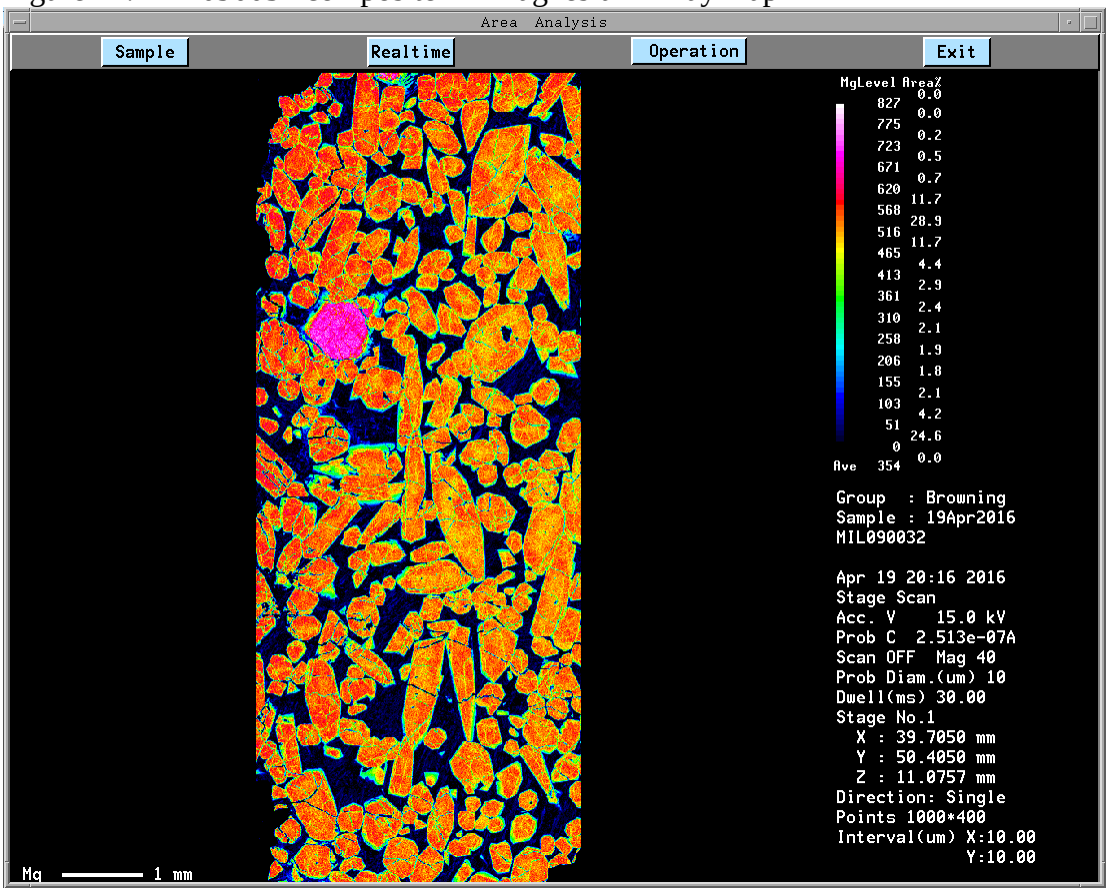

Figure 27. WDS x-ray map of magnesium in MIL090032 composite 1. Phases rich in magnesium are highlighted in red/orange and pink. Phases low in magnesum are dark blue. The phases visible in this image that are rich in magnesium are pyroxene (red/orange) and olivine (pink). Note the zoning on the rims of pyroxene and olivine.

Figure 28. MIL090032 composite 2 - magnesium x-ray map

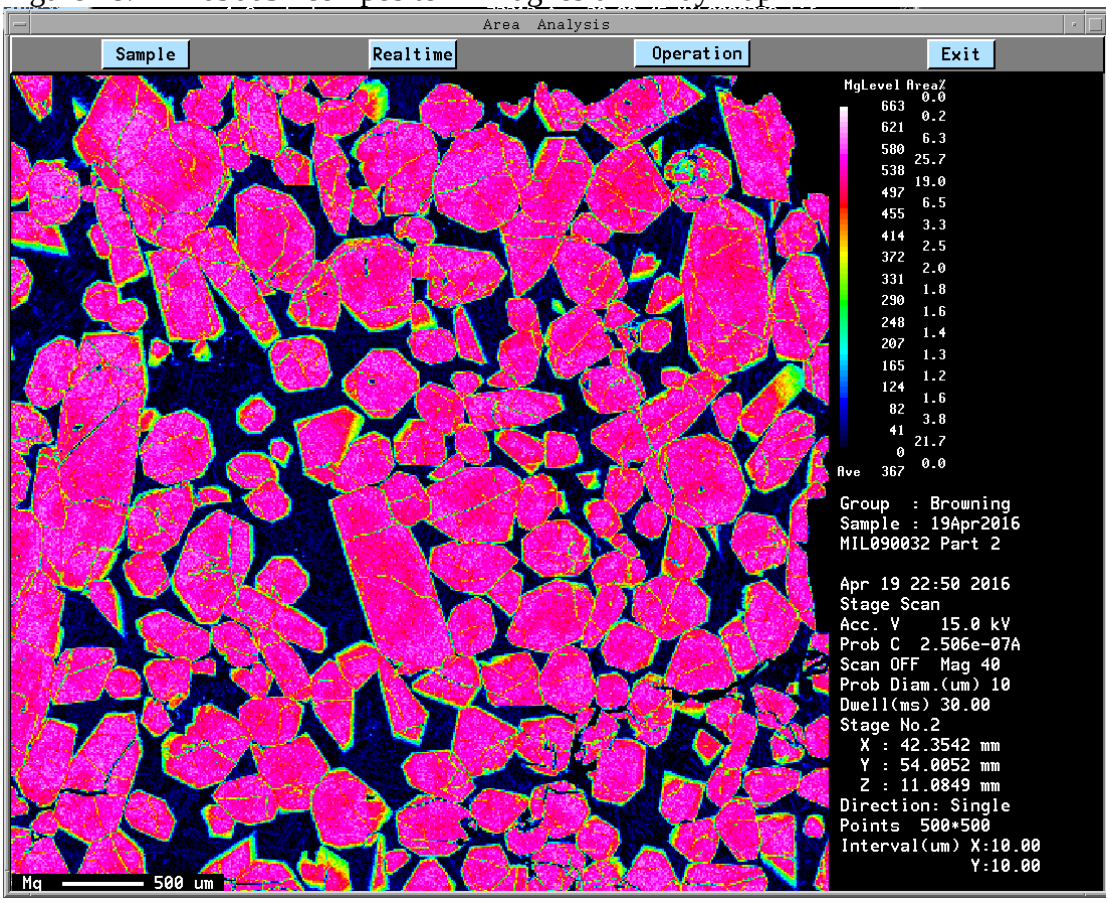

Figure 28. WDS x-ray map of magnesium in MIL090032 composite 2. Phases rich in magnesium are highlighted in red/orange and pink. Phases low in magnesum are dark blue. The phase visible in this image that is rich in magnesium is pyroxene (red/orange). Note the zoning on the rims of pyroxene.

Figure 29. MIL090032 composite 1 - titanium x-ray map

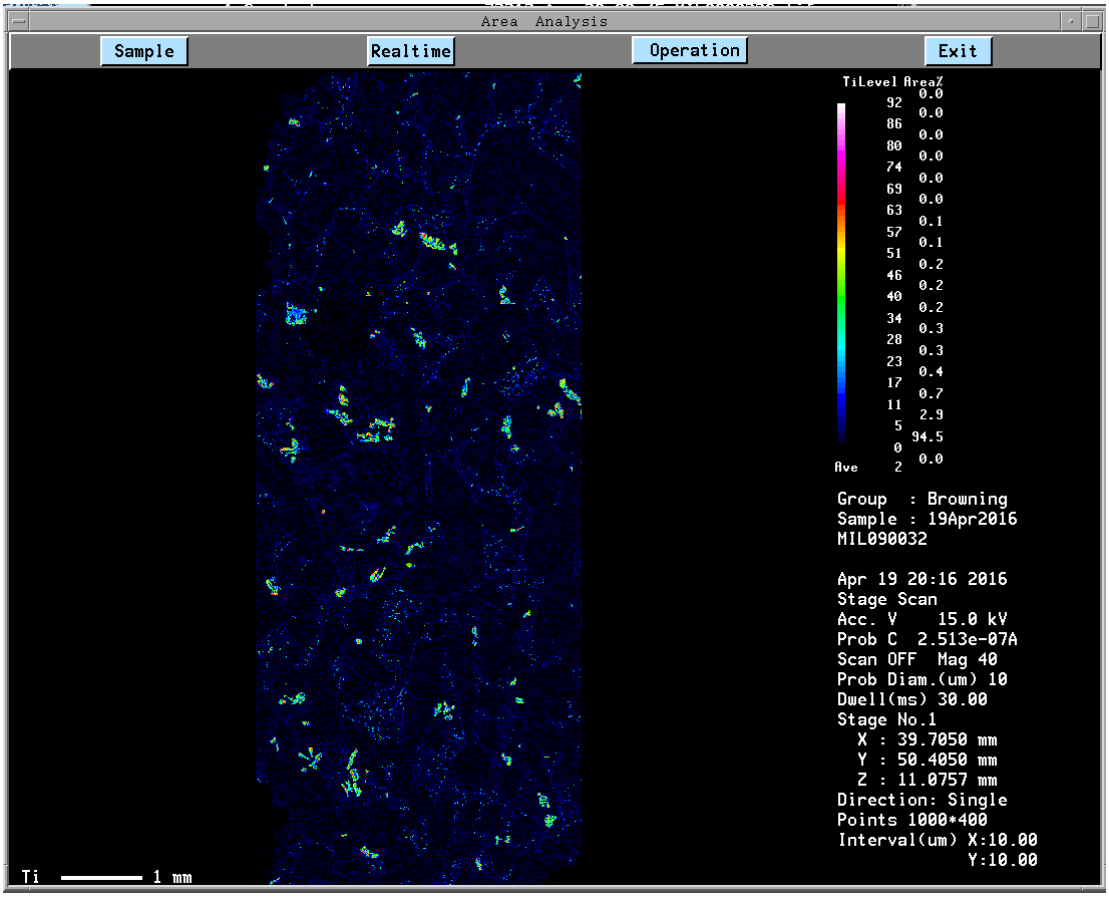

Figure 29. WDS x-ray map of titanium in MIL090032 composite 1. Phases rich in titanium are highlighted in green. Phases low in titanium are dark blue. The phase visible in this image that is rich in titanium is titanomagnetite.

Figure 30. MIL090032 composite 2 - titanium x-ray map

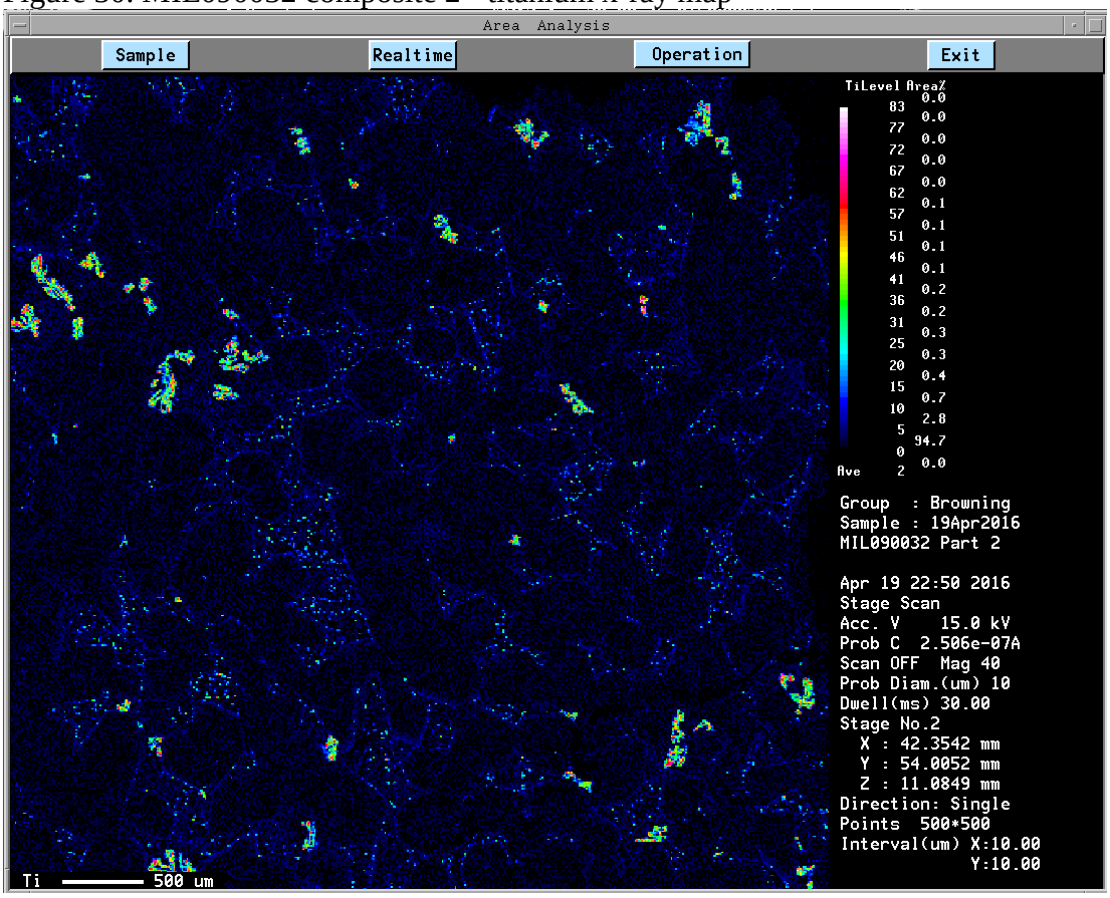

Figure 30. WDS x-ray map of titanium in MIL090032 composite 2. Phases rich in titanium are highlighted in green. Phases low in titanium are dark blue. The phase visible in this image that is rich in titanium is titanomagnetite.

Figure 31. MIL090136 composite 1 – calcium x-ray map

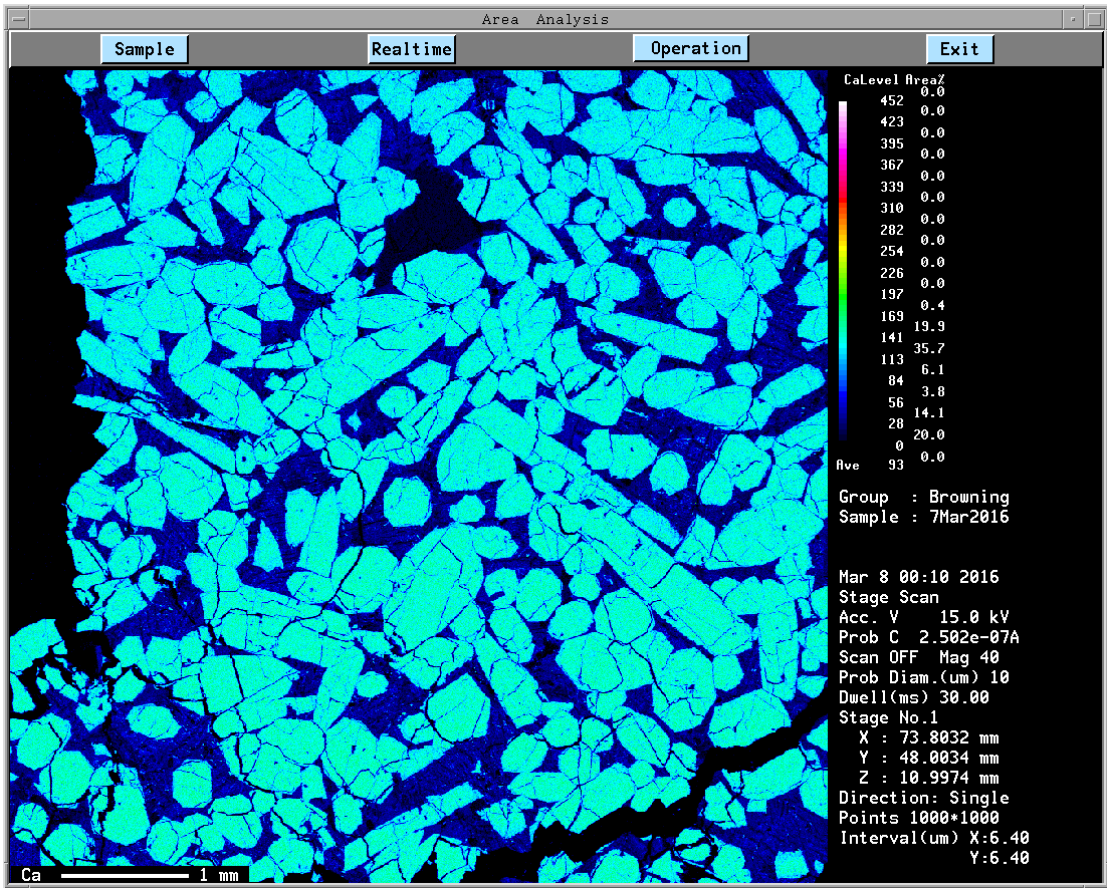

Figure 31. WDS x-ray map of calcium in MIL090136 composite 1. Phases rich in calcium are highlighted in light blue. Phases low in calcium are dark blue. The calcium rich phase is pyroxene.

Figure 32. MIL090136 composite 2 – calcium x-ray map

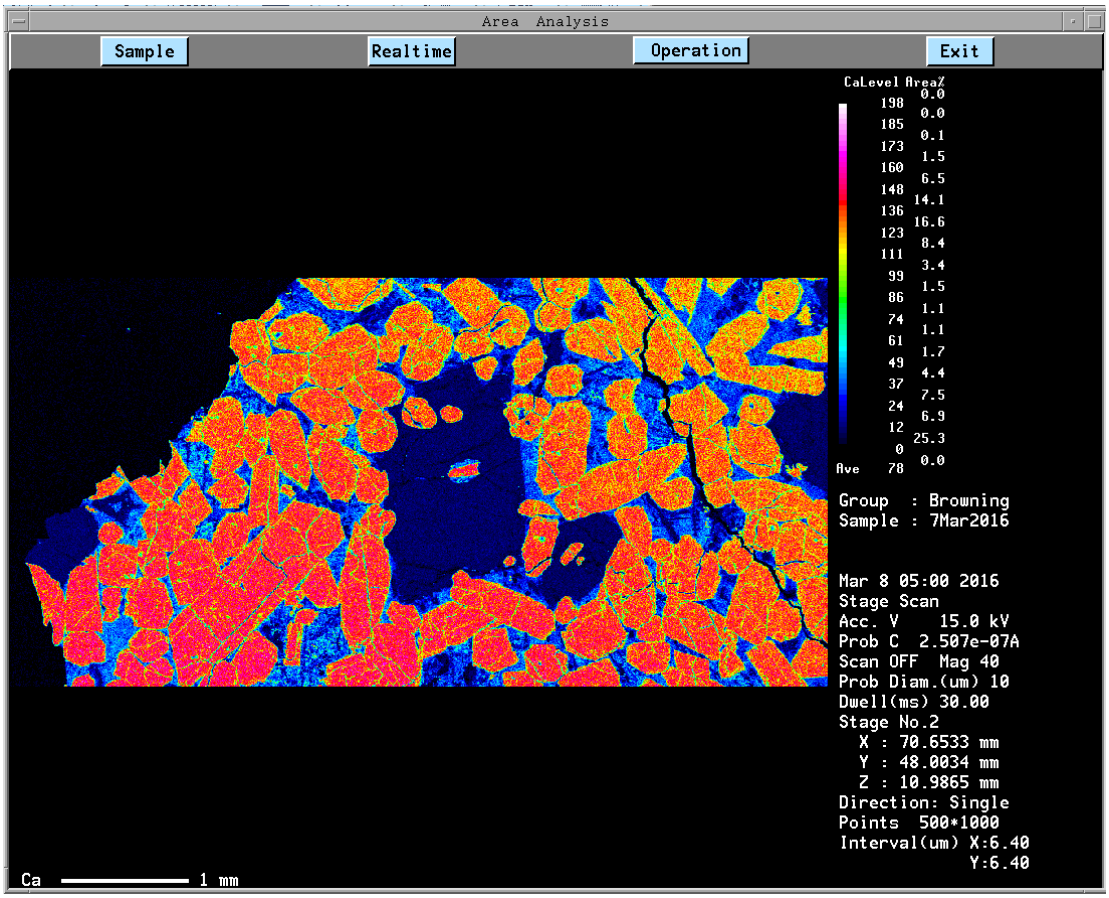

Figure 32. WDS x-ray map of calcium in MIL090136 composite 2. Phases rich in calcium are highlighted in red/orange. Phases low in calcium are blue. The calcium rich phase is pyroxene.

Figure 33. MIL090136 composite 1 - magnesium x-ray map

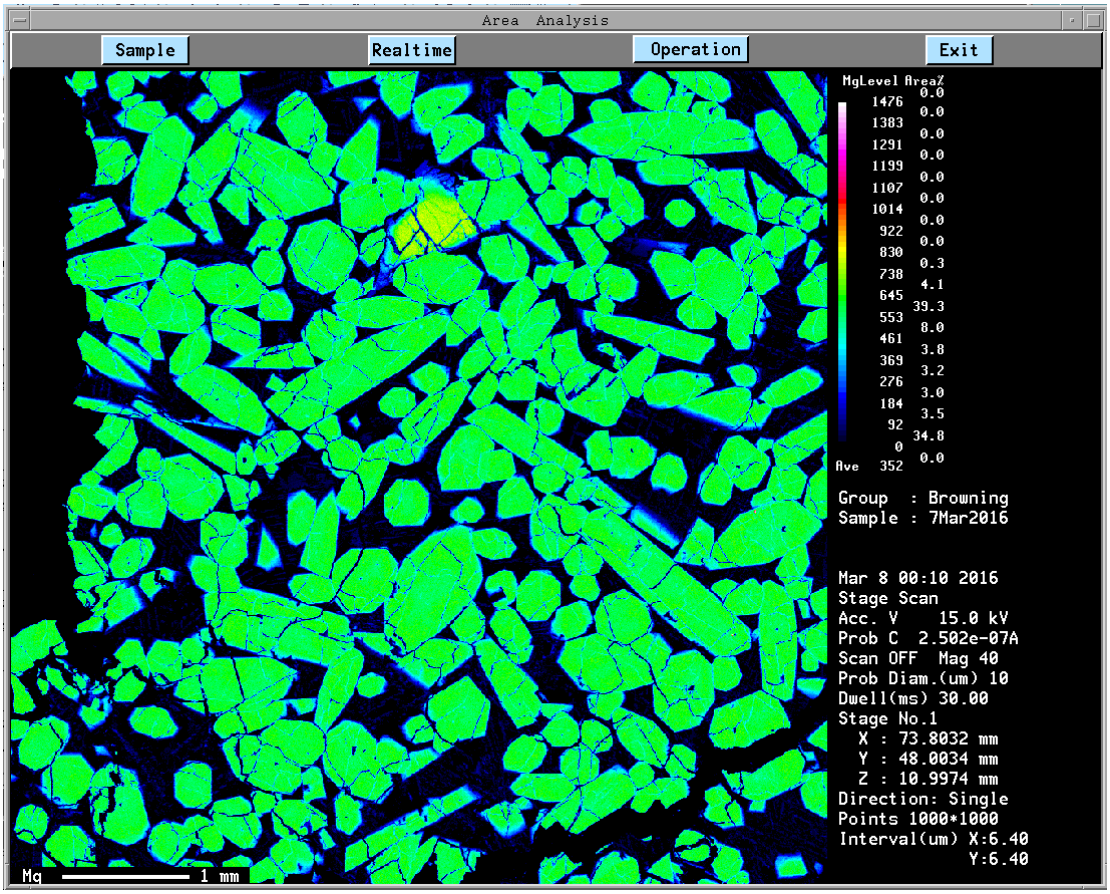

Figure 33. WDS x-ray map of magnesium in MIL090136 composite 1. Phases rich in magnesium are highlighted in green and yellow. Phases low in magnesum are dark blue. The phases visible in this image that are rich in magnesium are pyroxene (green) and olivine (yellow). Note the zoning on the rims of pyroxene and olivine.

Figure 34. MIL090136 composite 2 - magnesium x-ray map

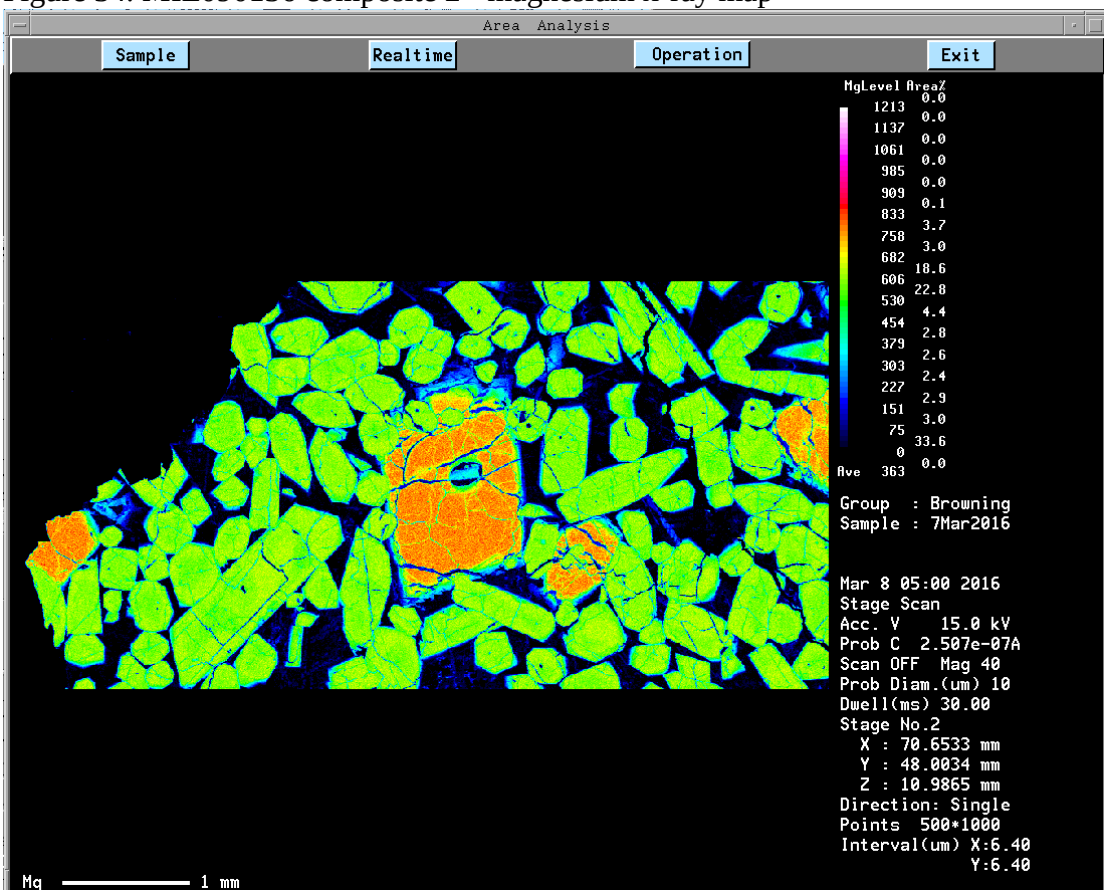

Figure 34. WDS x-ray map of magnesium in MIL090136 composite 2. Phases rich in magnesium are highlighted in orange and green. Phases low in magnesum are dark blue. The phases visible in this image that are rich in magnesium are pyroxene (green) and olivine (orange). Note the zoning on the rims of pyroxene and olivine.

Figure 35. MIL090136 composite 1 - iron x-ray map

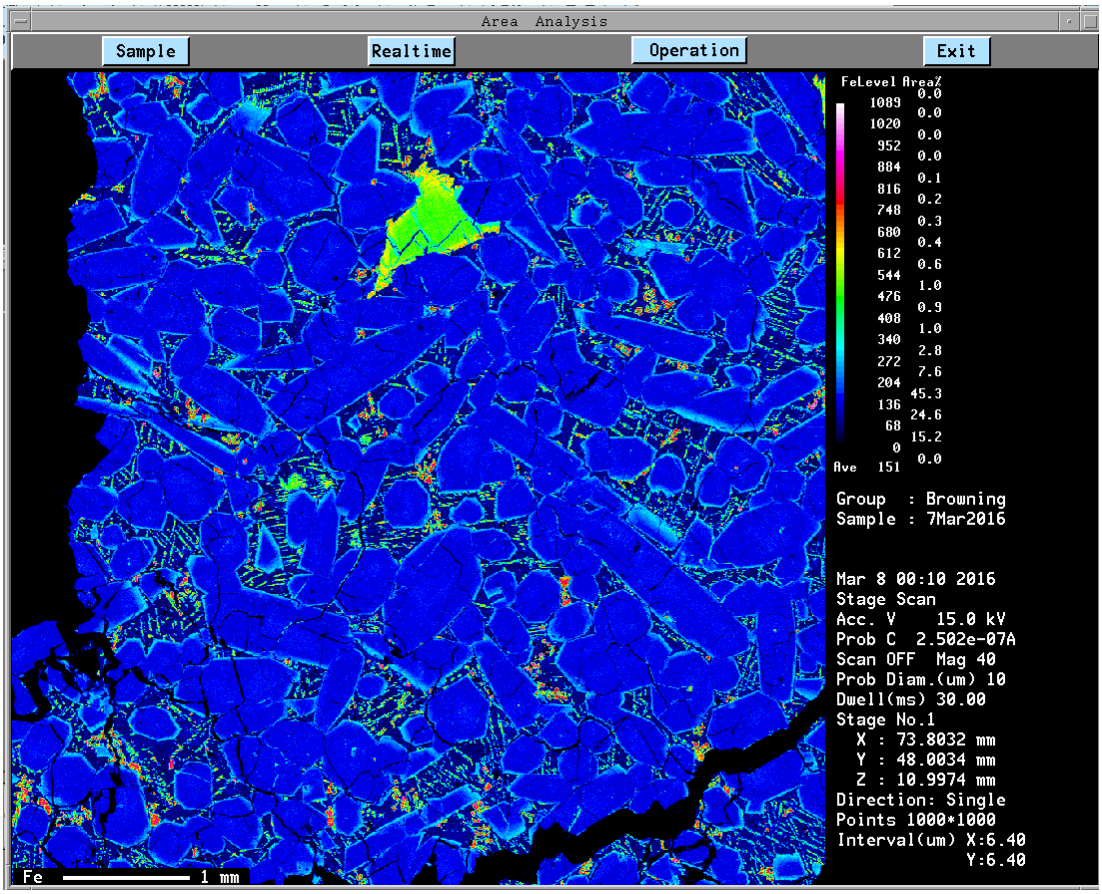

Figure 35. WDS x-ray map of iron in MIL090136 composite 1. Phases rich in iron are highlighted in green/yellow and pink/red. Phases low in iron are blue. The phases visible in this image that are rich in iron are olivine and titanomagnetite. Note the iron rich rims on the pyroxene (blue).

Figure 36. MIL090136 composite 2 - iron x-ray map

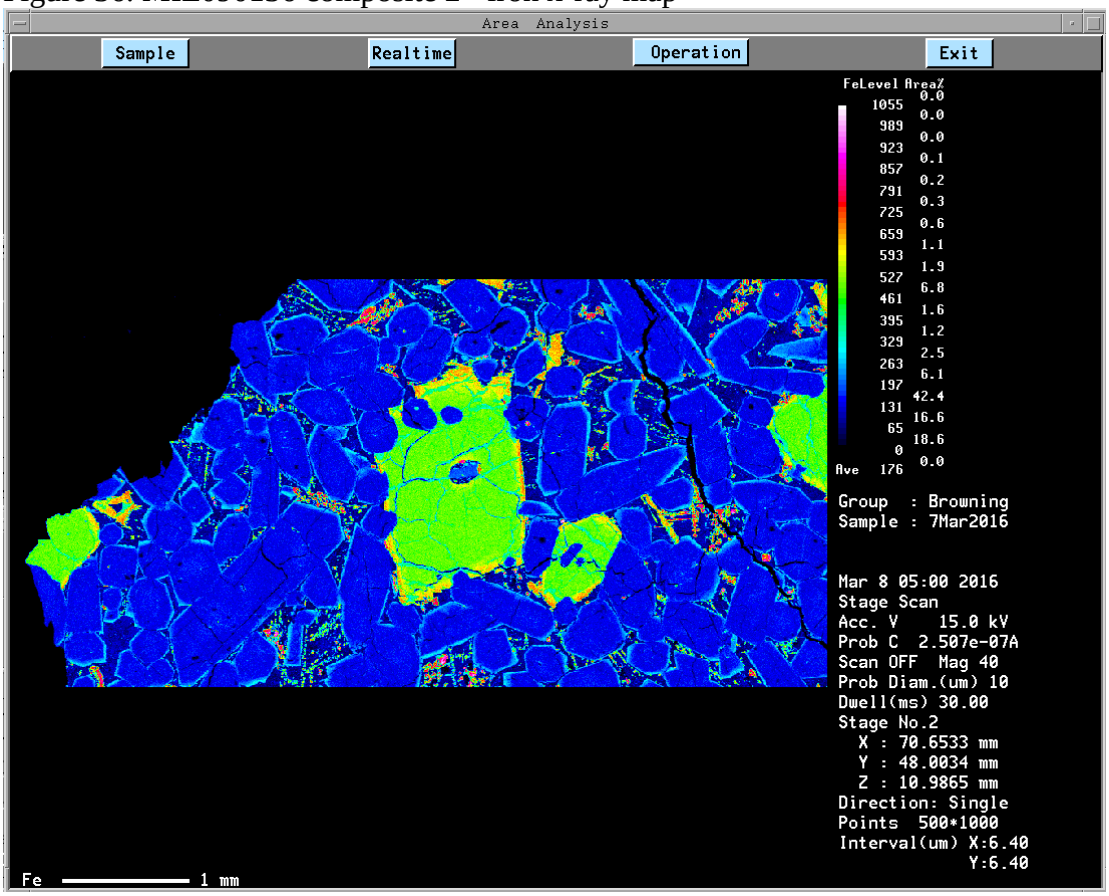

Figure 36. WDS x-ray map of iron in MIL090136 composite 2. Phases rich in iron are highlighted in green/yellow and pink/red. Phases low in iron are blue. The phases visible in this image that are rich in iron are olivine and titanomagnetite. Note the iron rich rims on the pyroxene and olivine.

Figure 37. MIL090136 composite 1 - sulfur x-ray map

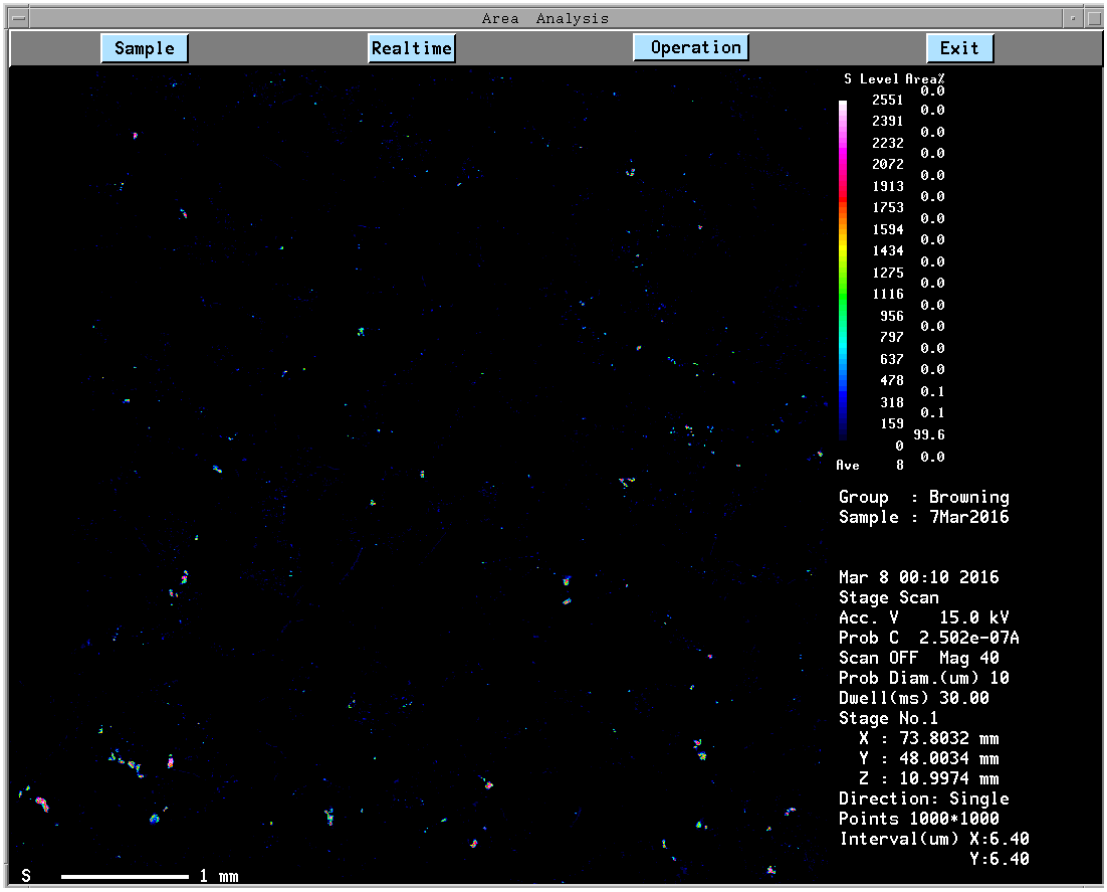

Figure 37. WDS x-ray map of sulfur in MIL090136 composite 1. Phases rich in sulfur are highlighted in green and red. Phases low in sulfur are dark blue. The phase visible in this image that is rich in sulfur is troilite.

Figure 38. MIL090136 composite 2 - sulfur x-ray map

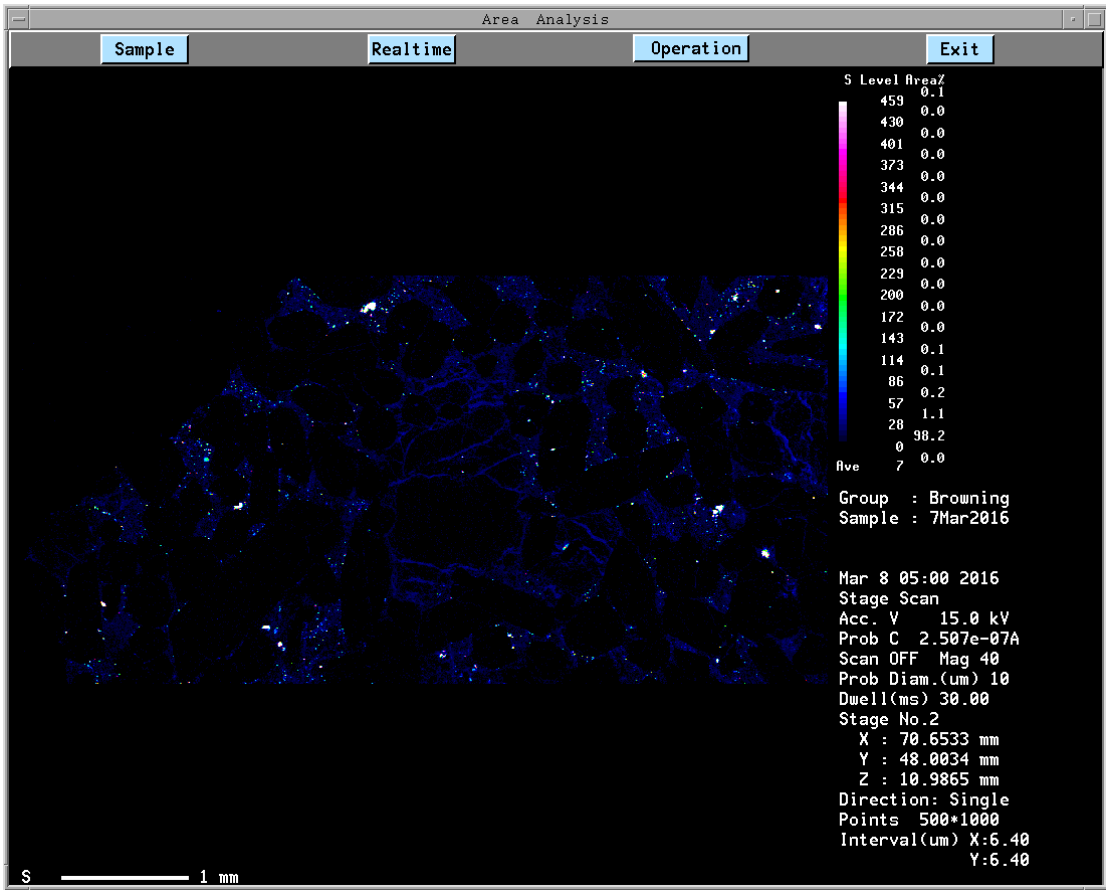

Figure 38. WDS x-ray map of sulfur in MIL090136 composite 2. Phases rich in sulfur are highlighted in green and red. Phases low in sulfur are dark blue. The phase visible in this image that is rich in sulfur is troilite.

Figure 39. MIL090136 composite 1 - titanium x-ray map

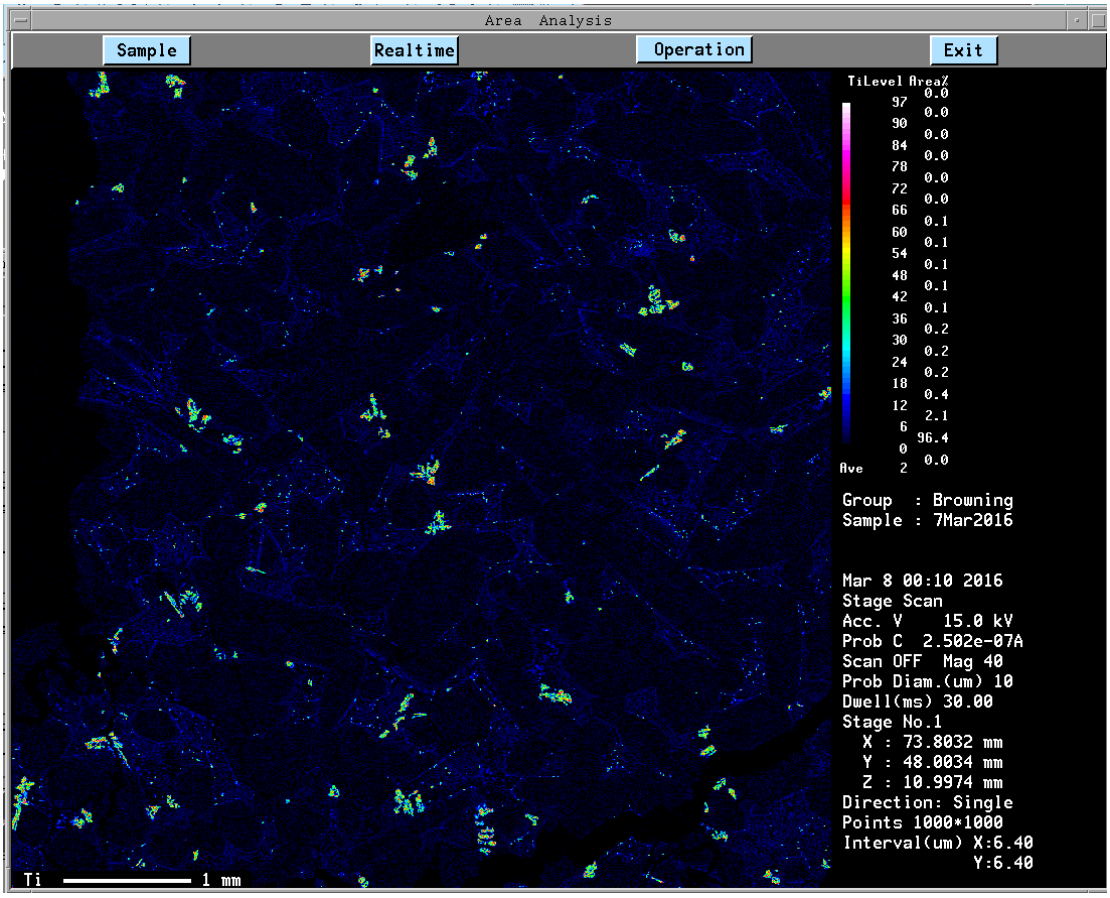

Figure 39. WDS x-ray map of titanium in MIL090136 composite 1. Phases rich in titanium are highlighted in green. Phases low in titanium are dark blue. The phase visible in this image that is rich in titanium is titanomagnetite.

Figure 40. MIL090136 composite 2 - titanium x-ray map

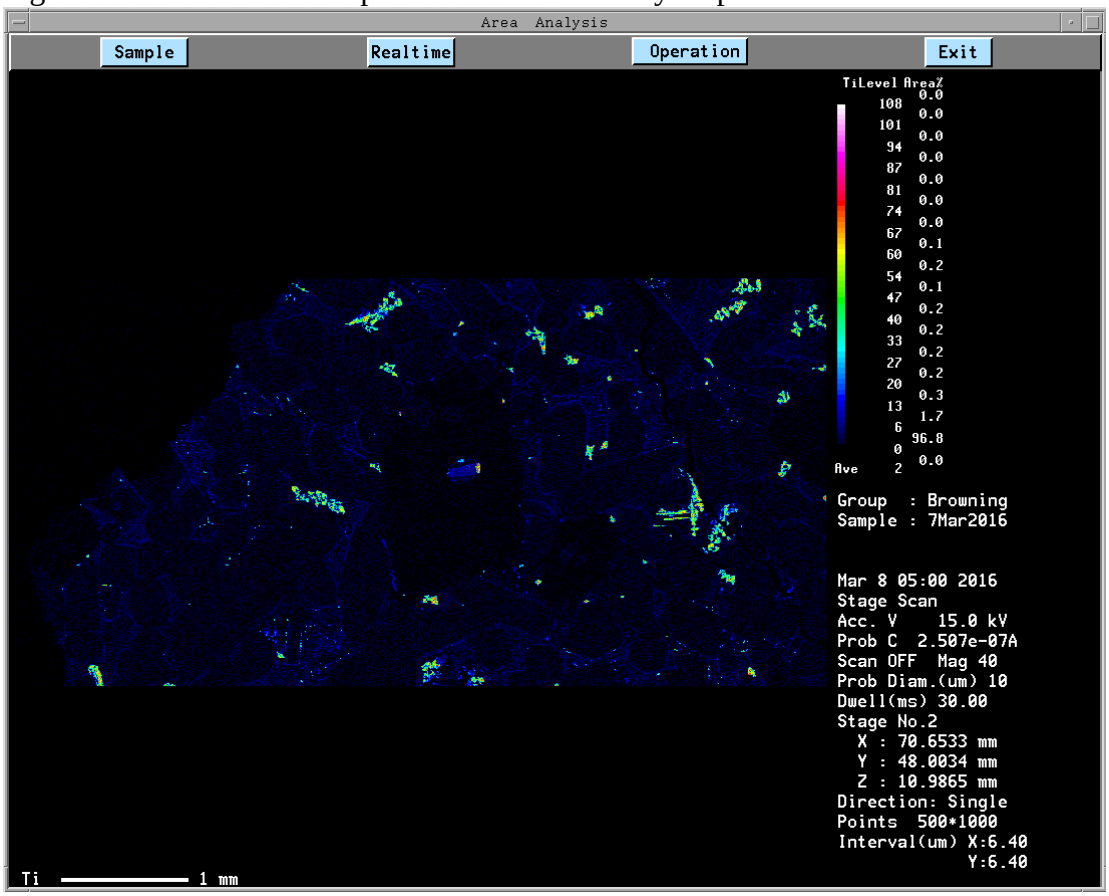

Figure 40. WDS x-ray map of titanium in MIL090136 composite 2. Phases rich in titanium are highlighted in green. Phases low in titanium are dark blue. The phase visible in this image that is rich in titanium is titanomagnetite.

ii. BSE Images of MIL090136

Figure 41. BSE image of MIL090136

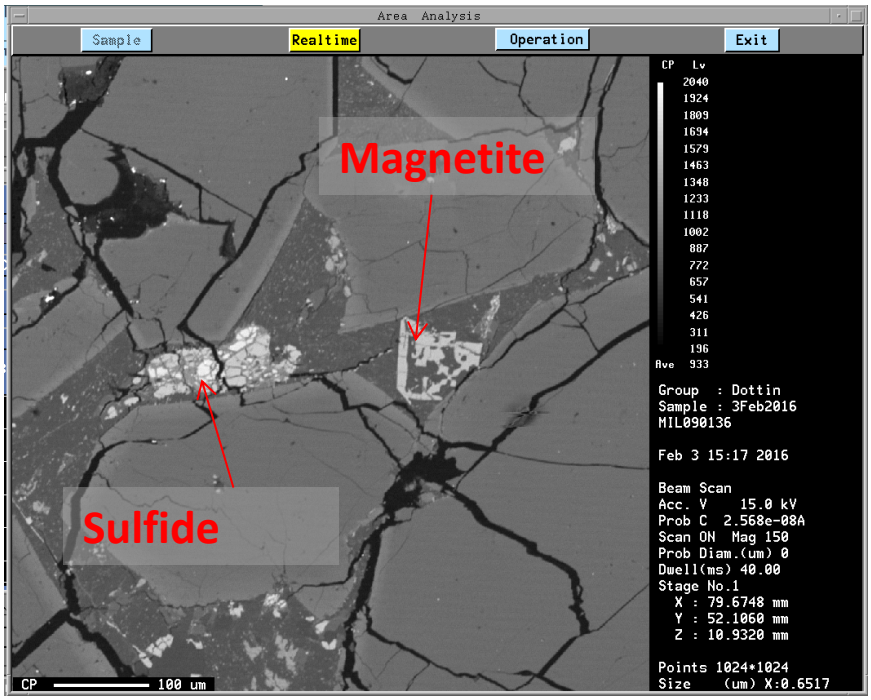

Figure 41. Back scattered electron image of MIL090136 highlighting the presence of sulfide and magnetite.

Figure 42. BSE image 2 of MIL090136

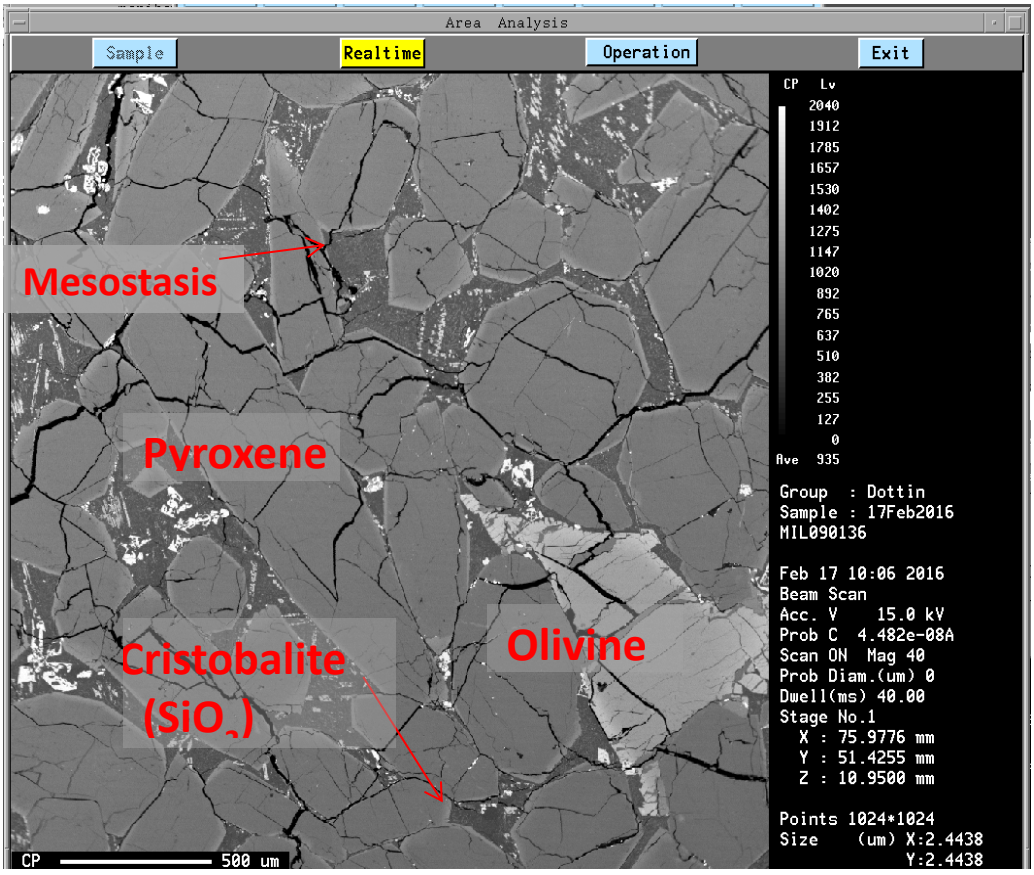

Figure 42. Back scattered electron image of MIL090136 highlighting the presence of mesostasis, pyroxene, cristobalite, and olivine.

iii. Electron Probe Microanalyzer (EPMA) data

Table 9. Major and minor element composition of pyroxene, olivine and magnetite in the MIL pairs (wt. %).

Phase	Olivine Grain #1					
MIL 090136	Core	Core	Rim	Rim	Rim	Rim
Comment			Adjacent to pyx	Adjacent to pyx	Adjacent to mesostasis	Adjacent to mesostasis
SiO_2	34.13	34.19	33.82	34.03	30.92	31.08
Al_2O_3	0.05	0.04	0.00	0.02	0.02	0.01
TiO_2	0.00	0.01	0.00	0.06	0.01	0.06
FeO	45.22	45.36	45.54	45.10	60.87	60.56
MgO	19.60	19.40	19.32	19.02	5.76	5.99
MnO	0.96	0.96	0.95	1.00	1.59	1.65
CaO	0.54	0.54	0.59	0.55	0.30	0.42
Cr_2O_3	0.01	0.00	0.01	0.00	0.00	0.00
NiO	0.059	0.021	0.057	0.041	0.021	0.035
Total	100.56	100.52	100.30	99.82	99.50	99.81

Phase	Olivine Grain #3					
MIL 090136	Core	Core	Rim	Rim	Rim	Rim
Comment			Adjacent to pyx	Adjacent to pyx	Adjacent to mesostasis	Adjacent to mesostasis
SiO_2	34.17	34.20	34.09	34.11	31.85	31.77
Al_2O_3	0.00	0.02	0.01	0.01	0.02	0.08
TiO_2	0.00	0.02	0.01	0.00	0.04	0.04
FeO	45.25	45.23	45.52	45.34	56.31	57.00
MgO	19.25	19.26	19.43	19.54	8.95	8.71
MnO	1.02	0.97	0.97	0.93	1.29	1.36
CaO	0.55	0.55	0.59	0.55	0.49	0.53
Cr_2O_3	0.04	0.00	0.00	0.01	0.07	0.00
NiO	0.000	0.000	0.000	0.004	0.041	0.000
Total	100.29	100.25	100.61	100.50	99.07	99.49

MIL090136
Olivine Grain #2

Core	Core	Rim Adjacent to pyx	Rim Adjacent to pyx	Rim Adjacent to mesostasis	Adjacent to mesostasis
33.97	34.27	34.03	34.21	31.01	31.32
0.01	0.02	0.02	0.01	0.03	0.01
0.01	0.01	0.00	0.02	0.01	0.03
45.01	45.07	45.50	44.90	60.48	59.74
19.45	19.37	19.19	19.51	5.83	6.72
0.97	0.98	0.94	0.96	1.42	1.38
0.54	0.57	0.54	0.55	0.47	0.58
0.01	0.03	0.00	0.04	0.00	0.00
0.038	0.000	0.042	0.000	0.006	0.000
100.01	100.32	100.26	100.20	99.26	99.78

Olivine Grain #4

Core	Core	Rim Adjacent to pyx	Rim Adjacent to pyx
33.97	33.99	33.64	34.01
0.01	0.04	0.07	0.02
0.00	0.02	0.01	0.00
44.59	45.32	45.31	45.56
19.16	19.49	17.91	18.94
1.06	0.99	0.90	1.00
0.49	0.58	0.55	0.60
0.01	0.00	0.00	0.03
0.059	0.027	0.039	0.003
99.35	100.47	98.43	100.16

Phase	Pyroxene Grain #1				Pyroxene Grain #2			
MIL 090136	Core	Core	Rim	Rim	Core	Core	Rim	Rim
Comment			Adjacent to mesostasis	Adjacent to mesostasis			Adjacent to mesostasis	Adjacent to mesostasis
SiO_2	51.72	51.48	47.96	48.27	51.61	51.92	47.28	46.75
Al_2O_3	0.95	0.97	3.05	2.89	0.96	0.92	3.55	3.89
TiO_2	0.27	0.28	0.75	0.71	0.27	0.28	0.91	1.06
FeO	14.39	14.54	24.81	22.47	14.06	12.99	24.22	26.82
MgO	12.20	12.34	5.86	7.31	12.90	13.18	5.46	5.07
MnO	0.44	0.46	0.63	0.57	0.43	0.38	0.68	0.70
CaO	18.82	19.14	17.12	17.45	19.15	18.97	17.38	16.20
Cr_2O_3	0.229	0.216	0.011	0.029	0.281	0.328	0.007	0.000
NiO	0.025	0.000	0.024	0.000	0.000	0.033	0.000	0.000
Total	99.05	99.43	100.21	99.70	99.67	98.99	99.49	100.50

Phase	Pyroxene Grain #3		Pyroxene Grain #4					
MIL 090136	Core	Rim	Core	Core	Rim	Rim	Rim	Rim
Comment		Adjacent to mesostasis			Adjacent to mesostasis	Adjacent to mesostasis	Adjacent to pyx	Adjacent to pyx
SiO_2	49.96	44.91	52.02	52.12	51.09	49.99	50.05	50.89
Al_2O_3	1.91	5.85	0.93	0.94	1.33	1.73	1.39	1.39
TiO_2	0.49	1.68	0.28	0.21	0.34	0.45	0.37	0.31
FeO	18.80	25.95	13.87	13.50	17.16	19.76	16.11	15.83
MgO	9.84	2.15	12.93	13.33	11.49	9.92	11.23	11.75
MnO	0.50	0.53	0.44	0.44	0.51	0.54	0.42	0.44
CaO	18.10	19.03	19.08	18.86	18.30	17.89	17.74	18.47
Cr_2O_3	0.052	0.031	0.352	0.344	0.092	0.047	0.100	0.136
NiO	0.000	0.016	0.000	0.007	0.000	0.000	0.028	0.000
Total	99.64	100.15	99.89	99.76	100.31	100.33	97.43	99.22

Phase	Pyroxene Grain #5				Pyroxene Grain #6			
MIL 090136	Core	Core	Rim	Rim	Core	Core	Rim	Rim
Comment			Adjacent to mt-rich	Adjacent to mt- rich mesostasis			Adjacent to olivine	Adjacent to olivine
SiO_2	52.29	52.14	51.64	51.58	51.81	51.88	51.30	52.00
Al_2O_3	0.90	0.92	1.13	1.15	1.00	1.27	0.92	0.96
TiO_2	0.24	0.19	0.29	0.26	0.33	0.32	0.26	0.19
FeO	13.58	13.58	14.86	14.95	14.03	14.49	13.31	13.99
MgO	13.33	13.17	12.47	12.23	12.84	12.69	13.12	13.28
MnO	0.38	0.40	0.41	0.46	0.42	0.46	0.40	0.39
CaO	18.79	18.78	19.09	18.59	19.09	18.44	18.60	18.95
Cr_2O_3	0.385	0.333	0.247	0.240	0.409	0.517	0.374	0.404
NiO	0.000	0.000	0.016	0.000	0.000	0.008	0.017	0.055
Total	99.90	99.52	100.15	99.45	99.93	100.07	98.31	100.22

Phase	Olivine Grain 1				Olivine Grain 2				Olivine Grain 3					
Comment MIL090032	Core	Core	Rim Adjacent to Pyx	Rim Adjacent to Pyx	Core	Core	Rim Adjacent to Pyx	Rim Adjacent to Pyx	Core	Core	Rim Adjacent to Pyx	Rim Adjacent to Pyx	Rim Adjacent to Mesostasis	Rim Adjacent to Mesostasis
SiO_2	34.30	34.48	33.91	33.82	34.46	34.54	34.26	34.12	30.75	32.84	31.39	30.86	30.73	31.19
Al_2O_3	0.01	0.04	0.01	0.00	0.01	0.03	0.04	0.02	0.10	0.04	0.04	0.08	0.02	0.01
TiO_2	0.00	0.02	0.00	0.04	0.00	0.00	0.00	0.01	0.00	0.01	0.00	0.00	0.06	0.11
FeO	45.35	45.56	45.64	47.46	44.92	45.17	43.89	45.06	52.80	54.20	53.19	52.13	59.79	60.08
MgO	19.87	19.63	17.80	17.36	19.62	19.75	19.40	19.42	10.50	11.68	10.73	9.82	5.31	5.62
MnO	0.93	0.92	0.90	0.94	0.96	0.95	0.90	0.92	1.11	1.16	1.19	1.19	1.55	1.51
CaO	0.59	0.52	0.50	0.58	0.56	0.55	0.64	0.65	0.48	0.52	0.44	0.36	0.13	0.15
Cr_2O_3	0.00	0.01	0.00	0.00	0.00	0.00	0.07	0.04	0.00	0.00	0.00	0.00	0.02	0.00
NiO	0.01	0.03	0.00	0.00	0.00	0.02	0.00	0.00	0.00	0.02	0.00	0.00	0.00	0.00
Total	101.07	101.23	98.76	100.20	100.55	101.01	99.20	100.24	95.74	100.47	96.97	94.43	97.61	98.66

Phase	Pyroxene Grain 1						Pyroxene Grain 2					
Comment	Core	Core	Rim Adjacent	Rim Adjacent	Rim Adjacent	Rim Adjacent	Core	Core	Rim Adjacent	Rim Adjacent	Rim Adjacent	Rim Adjacent
MIL090032			to Ol	to Ol	to Pyx	to Pyx			to Pyx	to Pyx	to Mesostasis	to Mesostasis
SiO_2	52.41	52.31	52.41	51.85	51.79	52.44	52.25	51.90	52.28	52.42	47.48	47.29
Al_2O_3	0.89	0.87	0.95	0.93	1.21	0.93	0.94	0.93	0.97	0.93	4.01	4.04
TiO_2	0.21	0.25	0.20	0.21	0.30	0.20	0.32	0.29	0.20	0.23	0.76	0.79
FeO	13.79	13.37	13.56	14.18	15.23	13.86	14.55	14.44	13.74	13.53	25.91	25.59
MgO	13.09	13.14	12.84	12.95	12.33	13.03	12.64	12.25	13.09	13.29	4.35	4.21
MnO	0.42	0.40	0.39	0.74	0.41	0.46	0.44	0.52	0.40	0.41	0.55	0.57
CaO	18.95	18.83	19.09	18.63	18.66	19.01	18.86	18.86	19.05	19.17	17.49	17.47
Cr_2O_3	0.29	0.33	0.37	0.32	0.18	0.36	0.17	0.11	0.29	0.39	0.00	0.00
NiO	0.00	0.00	0.02	0.01	0.00	0.00	0.03	0.00	0.03	0.00	0.00	0.00
Total	100.06	99.49	99.83	99.82	100.12	100.29	100.20	99.30	100.05	100.39	100.55	99.96

Phase	Pyroxene Grain 3				Pyroxene Grain 4				Pyroxene Grain 5			
Comment MIL090032	Core	Core	Rim Adjacent to Pyx	Rim Adjacent to Pyx	Core	Core	Rim Adjacent to Mesostasis	Rim Adjacent to Mesostasis	Core	Core	Rim Adjacent to Mesostasis	Rim Adjacent to Mesostasis
SiO_2	52.40	51.80	52.23	52.19	52.41	52.77	48.04	50.50	52.32	52.16	49.22	48.97
Al_2O_3	0.86	1.02	0.98	0.95	0.95	0.85	2.29	1.87	0.96	0.96	1.98	2.04
TiO_2	0.26	0.30	0.29	0.28	0.25	0.20	0.63	0.48	0.18	0.31	0.54	0.60
FeO	14.30	14.70	14.69	14.09	13.38	13.72	25.95	18.83	14.13	14.17	22.20	23.86
MgO	12.77	12.66	12.83	12.99	13.18	13.30	5.79	10.18	12.69	12.87	8.01	7.38
MnO	0.41	0.45	0.47	0.41	0.43	0.41	0.70	0.48	0.38	0.38	0.57	0.61
CaO	19.03	18.63	18.88	19.15	18.94	19.16	15.80	17.08	19.12	19.14	16.75	16.33
Cr_2O_3	0.19	0.15	0.27	0.31	0.37	0.23	0.02	0.09	0.38	0.28	0.03	0.01
NiO	0.01	0.00	0.00	0.00	0.01	0.03	0.00	0.04	0.00	0.00	0.00	0.00
Total	100.24	99.71	100.63	100.36	99.92	100.67	99.22	99.56	100.16	100.27	99.30	99.80

Phase	Olivine Grain 1						Olivine Grain 2			
Commen	Core	Core	Rim Adjacent	Rim Adjacent	Altered Rim	Altered Rim	Core	Core	Rim Adjacent	Rim Adjacent
MIL090030			to Altered Ol Rim	to Altered Ol Rim					to Pyx	to Pyx
SiO_2	34.28	34.45	33.99	33.98	31.80	32.12	34.24	34.44	34.12	33.79
Al_2O_3	0.01	0.03	0.03	0.03	0.06	0.02	0.01	0.02	0.01	0.03
TiO_2	0.00	0.00	0.00	0.01	0.02	0.02	0.00	0.01	0.01	0.00
FeO	44.74	44.39	46.30	46.67	56.50	55.01	44.73	44.79	44.50	45.11
MgO	19.94	19.99	18.15	18.15	9.04	10.69	20.12	20.10	19.71	19.10
MnO	0.89	0.93	0.99	0.96	1.41	1.25	0.94	0.91	0.90	0.95
CaO	0.56	0.55	0.54	0.53	0.52	0.58	0.53	0.52	0.55	0.52
Cr_2O_3	0.00	0.00	0.00	0.00	0.02	0.03	0.02	0.00	0.02	0.01
NiO	0.01	0.05	0.01	0.00	0.00	0.00	0.02	0.03	0.02	0.00
Total	100.43	100.38	100.02	100.33	99.37	99.72	100.60	100.80	99.84	99.54

Phase	Olivine Grain 3				Olivine Grain 4				Olivine Grain 5			
Comment	Core	Core	Rim Adjacent	Rim Adjacent	Core	Core	Rim Adjacent	Rim Adjacent	Core	Core	Rim Adjacent	Rim Adjacent
MIL090030			to Mesostasis	to Mesostasis			to Pyx	to Pyx			to Pyx	to Pyx
SiO_2	34.37	34.32	31.00	31.28	34.36	34.47	34.08	34.33	34.26	34.28	33.85	34.04
Al_2O_3	0.03	0.01	0.04	0.02	0.02	0.01	0.03	0.01	0.00	0.01	0.01	0.00
TiO_2	0.00	0.01	0.03	0.05	0.02	0.00	0.00	0.00	0.04	0.00	0.04	0.00
FeO	44.88	44.73	60.36	59.66	44.73	44.67	44.69	44.47	44.56	44.80	45.00	46.02
MgO	19.74	19.79	5.70	6.52	20.09	19.97	19.43	19.89	19.92	20.02	19.00	18.53
MnO	0.92	0.98	1.58	1.59	0.94	0.92	0.98	0.92	0.91	0.90	0.96	0.89
CaO	0.57	0.52	0.50	0.57	0.56	0.58	0.57	0.59	0.56	0.54	0.58	0.53
Cr_2O_3	0.00	0.01	0.00	0.01	0.00	0.00	0.00	0.03	0.03	0.00	0.03	0.05
NiO	0.01	0.01	0.00	0.00	0.00	0.03	0.01	0.00	0.01	0.00	0.06	0.00
Total	100.51	100.39	99.20	99.69	100.72	100.65	99.78	100.24	100.28	100.55	99.53	100.06

Phase	Pyroxene Grain 1				Pyroxene Grain 2			
Comment	Core	Core	Rim Adjacent	Rim Adjacent	Core	Core	Rim Adjacent	Rim Adjacent
MIL090030			to Ol	to Ol			to Mesostasis	to Mesostasis
SiO_2	51.93	51.81	52.10	51.84	51.70	51.98	51.67	47.66
Al_2O_3	0.93	1.03	1.12	0.87	1.13	1.10	0.96	3.71
TiO_2	0.22	0.30	0.40	0.20	0.29	0.31	0.25	0.91
FeO	13.92	13.71	13.80	13.36	13.85	13.89	14.09	22.92
MgO	12.85	12.85	13.12	13.11	12.77	13.03	12.92	6.04
MnO	0.40	0.40	0.40	0.41	0.37	0.40	0.40	0.57
CaO	18.74	18.83	18.79	18.80	18.52	18.85	18.45	18.06
Cr_2O_3	0.46	0.48	0.37	0.35	0.45	0.50	0.33	0.00
NiO	0.00	0.00	0.00	0.01	0.00	0.03	0.00	0.00
Total	99.46	99.41	100.11	98.96	99.09	100.09	99.05	99.87

Phase	Pyroxene Grain 3				Pyroxene Grain 4				Pyrxene Grain 5			
Commen MIL090030	Core	Core	Rim Adjacent to Ol	im Adjacent to Ol	Core	Core	Rim Adjacent to Mesostasis	Rim Adjacent to Mesostasis	Core	Core	Rim Adjacent to Pyx	Rim Adjacent to Pyx
SiO_2	52.01	51.92	52.32	52.08	51.53	51.61	50.44	51.08	51.84	51.79	51.83	51.95
Al_2O_3	1.02	1.01	0.89	0.91	1.01	1.04	1.81	1.20	1.01	0.99	0.94	0.93
TiO_2	0.32	0.25	0.25	0.26	0.32	0.27	0.46	0.34	0.30	0.30	0.27	0.29
FeO	13.76	13.61	13.97	14.11	13.74	14.00	17.14	15.24	14.01	14.15	13.49	13.62
MgO	12.85	12.71	13.18	12.99	12.60	12.73	10.52	11.91	12.68	12.74	12.96	12.96
MnO	0.41	0.39	0.39	0.39	0.45	0.43	0.44	0.38	0.37	0.39	0.41	0.43
CaO	19.10	18.82	18.92	19.12	19.01	18.95	18.13	18.75	18.89	18.93	19.06	18.99
Cr_2O_3	0.42	0.41	0.35	0.32	0.40	0.43	0.04	0.15	0.43	0.40	0.34	0.28
NiO	0.00	0.00	0.00	0.00	0.00	0.04	0.00	0.02	0.00	0.01	0.00	0.02
Total	99.89	99.11	100.28	100.18	99.07	99.48	98.96	99.08	99.52	99.69	99.31	99.46

Phase	Mt Grain 1	Mt Grain 2	Mt Grain 3	Mt Grain 4	Mt Grain 5	Mt Grain 6	Mt Grain 7	Mt Grain 8	Mt Grain 9	Mt Grain 10	Mt Grain 11	Mt Grain 12	Mt Grain 13	Mt Grain 14	Mt Grain 15
Comment MIL090032				Intergrown FeS	With SIMS Spot	Adjacent to Pyx			Adjacent to Ol	Adjacent to Ol	Adjacent to Pyx				
SiO_2	0.21	0.30	0.28	2.04	0.25	0.24	0.26	0.86	0.25	0.17	0.19	0.28	0.25	0.25	0.26
Al_2O_3	2.83	2.99	2.93	0.79	3.05	2.79	3.45	0.86	3.35	3.10	3.03	2.75	2.06	2.37	2.40
TiO_2	11.31	16.58	18.69	2.43	13.78	18.52	13.51	3.56	17.68	21.23	19.05	16.07	17.76	15.85	20.64
FeO	77.37	72.76	70.21	84.74	74.80	71.14	74.48	86.72	70.35	67.75	68.21	72.40	72.12	74.07	69.60
MgO	0.13	0.12	0.18	0.13	0.15	0.15	0.13	0.11	0.22	0.42	0.41	0.16	0.16	0.18	0.19
MnO	0.41	0.54	0.55	0.24	0.52	0.60	0.42	0.18	0.57	0.54	0.55	0.55	0.59	0.52	0.60
CaO	0.07	0.05	0.07	0.29	0.13	0.09	0.06	0.03	0.05	0.05	0.07	0.11	0.04	0.06	0.05
Cr_2O_3	0.02	0.02	0.05	0.00	0.02	0.00	0.00	0.00	0.08	0.21	0.13	0.06	0.04	0.01	0.01
NiO	0.00	0.00	0.02	0.00	0.00	0.00	0.01	0.00	0.00	0.01	0.00	0.02	0.00	0.00	0.00
Total	92.35	93.36	92.98	90.67	92.71	93.53	92.32	92.33	92.54	93.49	91.65	92.40	93.03	93.32	93.75

Phase	Mt Grain 1	Mt Grain 2	Mt Grain 3	Mt Grain 4	Mt Grain 5	Mt Grain 6	Mt Grain 7	Mt Grain 8	Mt Grain 9	Mt Grain 10	Mt Grain 11	Mt Grain 12	Mt Grain 13	Mt Grain 14	Mt Grain 15
Comment MIL090136		Atached to Pyx	Attached to Ol		Intergrown Ol	Intergrown Ol	Intergrown FeS	Intergrown FeS		Intergrown FeS	Adjacent to Ol				
SiO_2	0.27	0.38	0.26	1.67	31.51	42.56	0.36	0.23	0.23	1.21	0.54	0.31	0.18	0.23	0.08
Al_2O_3	1.94	2.93	3.10	0.63	0.03	0.73	1.95	0.89	2.06	0.70	2.00	1.83	2.76	0.85	0.00
TiO_2	19.24	13.69	18.52	2.63	0.01	0.06	20.88	1.93	16.09	1.12	7.58	18.92	13.75	4.77	0.00
FeO	70.43	74.60	71.20	85.68	60.43	34.46	68.24	87.67	74.85	86.00	81.92	71.05	75.59	84.62	76.30
MgO	0.20	0.18	0.29	0.13	6.24	4.17	0.22	0.05	0.14	0.13	0.19	0.18	0.13	0.08	0.01
MnO	0.71	0.58	0.57	0.19	1.64	0.82	0.68	0.20	0.62	0.27	0.35	0.68	0.51	0.25	0.06
CaO	0.05	0.09	0.06	0.27	0.29	0.19	0.11	0.10	0.06	0.17	0.17	0.04	0.04	0.13	0.08
Cr_2O_3	0.00	0.02	0.07	0.00	0.00	0.00	0.03	0.02	0.01	0.01	0.04	0.04	0.04	0.00	0.05
NiO	0.00	0.00	0.03	0.00	0.00	0.00	0.00	0.01	0.00	0.00	0.00	0.00	0.00	0.00	0.00
Total	92.83	92.47	94.08	91.21	100.15	82.99	92.47	91.09	94.06	89.62	92.78	93.05	93.00	90.93	76.57

Phase	Mt Grain 1	Mt Grain 2	Mt Grain 3	Mt Grain 4	Mt Grain 5	Mt Grain 6	Mt Grain 7	Mt Grain 8	Mt Grain 9	Mt Grain 10	Mt Grain 11	Mt Grain 12	Mt Grain 13	Mt Grain 14	Mt Grain 15
Comment		Elongagted					Spotted								
MIL090030															
SiO_2	0.21	0.21	0.16	0.42	0.19	0.21	1.46	0.26	0.41	0.26	0.15	0.28	0.24	0.17	0.23
Al_2O_3	1.82	2.12	2.60	2.53	3.24	2.77	0.96	0.35	0.73	0.37	0.90	2.05	2.50	1.63	2.10
TiO_2	19.97	18.69	18.92	20.55	18.43	15.36	2.75	0.70	1.49	0.64	6.39	16.58	18.57	15.57	20.72
FeO	68.62	70.98	70.70	68.68	70.85	73.32	83.26	89.41	87.61	88.88	83.34	75.16	71.23	74.69	68.76
MgO	0.23	0.17	0.15	0.23	0.32	0.33	0.13	0.05	0.04	0.08	0.10	0.24	0.27	0.16	0.21
MnO	0.54	0.69	0.66	0.71	0.56	0.52	0.24	0.13	0.16	0.18	0.34	0.47	0.52	0.51	0.69
CaO	0.07	0.02	0.06	0.09	0.03	0.04	0.20	0.04	0.03	0.11	0.09	0.05	0.09	0.06	0.04
Cr_2O_3	0.05	0.01	0.00	0.07	0.00	0.01	0.01	0.00	0.00	0.03	0.01	0.06	0.06	0.03	0.00
NiO	0.00	0.00	0.00	0.00	0.00	0.00	0.00	0.00	0.00	0.00	0.01	0.00	0.02	0.05	0.00
Total	91.52	92.89	93.23	93.29	93.61	92.55	89.01	90.93	90.47	90.55	91.32	94.89	93.49	92.88	92.76

iii. Counting Statistic error on EPMA analyses

Table 10. Uncertainty due to counting statistics reported in relative (%)-MIL090136 Olivine

Uncertainty Due to Counting Statistics (Rel %) MIL090136-Olivine

Comment	No.	SiO2	Al2O3	TiO2	FeO	MgO	MnO	CaO	Cr2O3	NiO
MIL090136 ol #1 core	34	0.36	26.43	100.00	0.28	0.51	3.22	3.34	417.49	42.46
MIL090136 ol #1 core	35	0.36	31.35	261.46	0.28	0.51	3.13	3.26	100.00	121.66
MIL090136 ol #1 rim-adjacent to pyx	36	0.36	365.65	100.00	0.28	0.51	3.21	3.04	168.71	44.41
MIL090136 ol #1 rim-adjacent to pyx	37	0.36	68.91	35.84	0.28	0.51	3.09	3.24	100.00	64.00
MIL090136 ol #1 rim-adjacent to meso	38	0.38	71.43	217.23	0.24	1.00	2.29	5.23	661.71	126.07
MIL090136 ol #1 rim-adjacent to meso	39	0.38	124.27	36.75	0.24	0.98	2.21	3.98	100.00	72.98
MIL090136 ol #2 core	40	0.36	100.31	203.54	0.28	0.51	3.19	3.33	189.09	67.24
MIL090136 ol #2 core	41	0.36	61.98	147.23	0.28	0.51	3.10	3.17	67.49	100.00
MIL090136 ol #2 rim-adjacent to pyx	42	0.36	83.46	100.00	0.28	0.51	3.29	3.27	100.00	60.48
MIL090136 ol #2 rim-adjacent to pyx	43	0.36	215.72	116.07	0.28	0.51	3.21	3.24	52.50	100.00
MIL090136 ol #2 rim-adjacent to meso	44	0.38	40.04	243.09	0.24	0.99	2.51	3.69	100.00	457.78
MIL090136 ol #2 rim-adjacent to meso	45	0.38	168.61	67.43	0.24	0.92	2.52	3.19	1713.50	100.00
MIL090136 ol #3 core	46	0.36	100.00	100.00	0.28	0.51	2.97	3.26	54.18	100.00
MIL090136 ol #3 core	47	0.36	80.38	82.70	0.28	0.51	3.11	3.23	551198.44	100.00
MIL090136 ol #3 rim-adjacent to pyx	48	0.36	157.22	261.01	0.28	0.51	3.14	3.00	100.00	100.00
MIL090136 ol #3 rim-adjacent to pyx	49	0.36	147.77	100.00	0.28	0.51	3.20	3.23	357.43	713.05
MIL090136 ol #3 rim-adjacent to meso	50	0.37	62.67	48.18	0.25	0.78	2.64	3.54	31.37	62.59
MIL090136 ol #3 rim-adjacent to meso	51	0.37	19.95	48.53	0.25	0.80	2.52	3.35	100.00	100.00
MIL090136 ol #4 core	52	0.36	119.57	100.00	0.28	0.51	2.92	3.56	159.82	42.59
MIL090136 ol #4 core	53	0.36	30.95	86.14	0.28	0.51	3.13	3.06	1678.73	97.88
MIL090136 ol #4 rim-adjacent to pyx	54	0.36	20.06	247.83	0.28	0.53	3.34	3.25	100.00	63.94
MIL090136 ol #4 rim-adjacent to pyx	55	0.36	64.87	100.00	0.28	0.52	3.08	3.05	78.91	792.34
MIL090136 ol #5 core	56	0.36	106.10	198.47	0.28	0.51	3.14	3.25	100.00	56.84
MIL090136 ol #5 core	57	0.36	100.00	100.00	0.28	0.51	3.21	3.08	100.00	2330.33
MIL090136 ol #5 rim adjacent to pyx	58	0.36	65.97	100.00	0.28	0.51	3.29	3.10	114.14	146.85
MIL090136 ol #5 rim adjacent to pyx	59	0.36	29.15	363.44	0.28	0.51	3.14	3.41	67.44	100.00

Table 11. Uncertainty due to counting statistics reported in relative (%)- MIL090030 Pyroxene

Uncertainty Due to Counting Statistics (Rel %) MIL090136-Pyroxene

Comment	No.	SiO2	Al2O3	TiO2	FeO	MgO	MnO	CaO	Cr2O3	NiO
MIL090136 Pyx #1 Core	10	0.28	2.39	8.88	0.52	0.60	5.55	0.39	10.91	96.00
MIL090136 Pyx #1 Core	11	0.28	2.24	8.52	0.52	0.59	5.43	0.39	11.36	100.00
MIL090136 Pyx #1 rim	12	0.29	1.17	3.72	0.39	0.91	4.32	0.41	214.40	100.88
MIL090136 Pyx #1 rim	13	0.29	1.19	3.97	0.41	0.80	4.56	0.40	78.32	100.00
MIL090136 Pyx #2 CORE	14	0.28	2.27	8.74	0.53	0.58	5.69	0.39	8.76	100.00
MIL090136 Pyx #2 CORE	15	0.28	2.40	8.45	0.55	0.57	6.43	0.39	7.74	73.14
MIL090136 Pyx #2 rim	16	0.30	1.07	3.29	0.40	0.94	4.06	0.40	341.63	100.00
MIL090136 Pyx #2 rim	17	0.30	1.02	2.98	0.37	0.99	4.00	0.42	100.00	100.00
MIL090136 Pyx #3 core	18	0.29	1.51	5.32	0.45	0.68	5.16	0.40	44.34	100.00
MIL090136 Pyx #3 rim	19	0.30	0.81	2.14	0.38	1.57	5.02	0.38	74.21	160.20
MIL090136 Pyx #4 core	20	0.28	2.33	7.89	0.53	0.58	5.48	0.39	7.20	100.00
MIL090136 Pyx #4 core	21	0.28	2.29	10.92	0.54	0.57	5.61	0.39	7.55	331.15
MIL090136 Pyx #4 rim	22	0.28	1.85	7.38	0.47	0.62	4.91	0.40	26.27	100.00
MIL090136 Pyx #4 rim	23	0.29	1.62	5.89	0.44	0.67	4.61	0.40	49.00	100.00
MIL090136 Pyx #4 rim-pyx	24	0.29	1.82	6.58	0.49	0.63	6.05	0.40	24.54	86.86
MIL090136 Pyx #4 rim-pyx	25	0.28	1.84	7.66	0.49	0.61	5.67	0.39	17.83	100.00
MIL090136 Pyx #5 core	26	0.28	2.39	9.03	0.54	0.57	6.18	0.39	6.64	100.00
MIL090136 Pyx #5 core	27	0.28	2.38	12.26	0.54	0.57	5.93	0.39	7.69	100.00
MIL090136 Pyx #5 rim-mt rich meso	28	0.28	2.07	8.29	0.51	0.59	5.97	0.39	9.95	149.26
MIL090136 Pyx #5 rim-mt rich meso	29	0.28	2.03	9.29	0.51	0.60	5.34	0.39	10.18	100.00
MIL090136 Pyx #6 core	30	0.28	2.22	7.35	0.53	0.58	5.65	0.39	6.58	100.00
MIL090136 Pyx #6 core	31	0.28	1.91	7.63	0.52	0.58	5.34	0.39	5.06	287.64
MIL090136 Pyx #6 rim-adjacent to ol	32	0.28	2.33	8.96	0.54	0.57	6.22	0.39	6.43	136.71
MIL090136 Pyx #6 rim-adjacent to ol	33	0.28	2.25	12.22	0.53	0.57	6.30	0.39	6.07	41.11

Table 12. Uncertainty due to counting statistics reported in relative (%) MIL 09030 and MIL 090032-Olivine

Uncertainty due to Counting Statistics (Relative %) MIL090032 and MIL090030-Olivine

Comment	No.	SiO2	Al2O3	TiO2	FeO	MgO	MnO	CaO	Cr2O3	NiO
MIL32-Olivine grain 1-core	12.00	0.36	93.59	100.00	0.28	0.50	3.29	2.95	100.00	207.33
MIL32-Olivine grain 1-core	13.00	0.36	31.70	85.55	0.28	0.51	3.39	3.34	160.66	94.75
MIL32-Olivine grain 1-rim adj. to pyx	14.00	0.36	128.31	100.00	0.28	0.54	3.53	3.51	100.00	100.00
MIL32-Olivine grain 1-rim adj. to pyx	15.00	0.36	100.00	55.47	0.27	0.54	3.36	3.05	100.00	100.00
MIL32-Olivine grain 2- core	16.00	0.36	100.81	100.00	0.28	0.51	3.18	3.21	100.00	100.00
MIL32-Olivine grain 2- core	17.00	0.36	40.43	100.00	0.28	0.51	3.26	3.33	100.00	120.64
MIL32-Olivine grain 2- rim adj. pyx	18.00	0.36	33.60	524.41	0.28	0.51	3.35	2.83	28.76	7094.85
MIL32-Olivine grain 2- rim adj. pyx	19.00	0.36	63.35	257.40	0.28	0.51	3.34	2.81	48.73	100.00
MIL32-Olivine grain 3- core	20.00	0.38	15.41	100.00	0.26	0.72	2.92	3.58	100.00	100.00
MIL32-Olivine grain 3- core	21.00	0.37	40.92	169.67	0.25	0.68	2.88	3.42	100.00	169.54
MIL32-Olivine grain 3-rim adj pyx	22.00	0.38	38.33	100.00	0.26	0.71	2.79	4.04	100.00	100.00
MIL32-Olivine grain 3-rim adj pyx	23.00	0.38	19.77	100.00	0.26	0.75	2.80	4.70	100.00	100.00
MIL32-Olivine grain 3-rim adj meso	24.00	0.38	82.27	37.63	0.24	1.05	2.33	11.21	110.54	100.00
MIL32-Olivine grain 3-rim adj meso	25.00	0.38	113.97	21.12	0.24	1.02	2.37	9.76	100.00	100.00
MIL30-olivine grain 1-core	50.00	0.36	125.10	100.00	0.28	0.50	3.36	3.10	4102.47	183.22
MIL30-olivine grain 1-core	51.00	0.36	42.13	100.00	0.28	0.50	3.36	3.20	1159.34	54.12
MIL30-olivine grain 1-rim adj alt rim	52.00	0.36	49.65	100.00	0.28	0.53	3.13	3.26	484.69	261.92
MIL30-olivine grain 1-rim adj alt rim	53.00	0.36	48.82	211.55	0.27	0.53	3.28	3.37	100.00	100.00
MIL30-olivine grain 1-alt rim	54.00	0.37	22.75	147.28	0.25	0.78	2.50	3.44	109.12	100.00
MIL30-olivine grain 1-alt rim	55.00	0.37	60.98	93.84	0.25	0.72	2.74	3.03	78.29	100.00
MIL30-olivine grain 2-core	56.00	0.36	279.37	100.00	0.28	0.50	3.15	3.29	118.52	150.18
MIL30-olivine grain 2-core	57.00	0.36	70.99	206.16	0.28	0.50	3.44	3.39	100.00	84.26
MIL30-olivine grain 2-rim adj pyx	58.00	0.36	202.33	434.52	0.28	0.51	3.35	3.11	93.43	160.87
MIL30-olivine grain 2-rim adj pyx	59.00	0.36	40.96	725.79	0.28	0.51	3.27	3.35	169.13	100.00
MIL30-olivine grain 3-core	60.00	0.36	49.40	100.00	0.28	0.51	3.37	3.04	1036.01	439.39
MIL30-olivine grain 3-core	61.00	0.36	109.89	147.55	0.28	0.51	3.15	3.39	270.14	180.94
MIL30-olivine grain 3-rim adj meso	62.00	0.38	36.07	79.41	0.24	1.01	2.37	3.59	100.00	100.00
MIL30-olivine grain 3-rim adj meso	63.00	0.38	80.14	47.12	0.24	0.94	2.30	3.12	168.96	100.00
MIL30-olivine grain 4-core	64.00	0.36	55.49	99.58	0.28	0.50	3.28	3.17	100.00	100.00
MIL30-olivine grain 4-core	65.00	0.36	126.51	100.00	0.28	0.50	3.39	2.99	100.00	88.20
MIL30-olivine grain 4-rim adj pyx	66.00	0.36	53.54	100.00	0.28	0.51	3.19	3.11	100.00	177.41
MIL30-olivine grain 4-rim adj pyx	67.00	0.36	114.35	100.00	0.28	0.50	3.39	2.96	85.30	100.00
MIL30-olivine grain 5-core	68.00	0.36	100.00	59.32	0.28	0.50	3.35	3.11	70.77	389.45
MIL30-olivine grain 5-core	69.00	0.36	234.96	100.00	0.28	0.50	3.44	3.29	100.00	100.00
MIL30-olivine grain 5-rim adj pyx	70.00	0.36	114.87	54.82	0.28	0.52	3.21	3.08	69.82	43.34
MIL30-olivine grain 5-rim adj pyx	71.00	0.36	472.97	100.00	0.28	0.52	3.38	3.35	46.88	100.00

Table 13. Uncertainty due to counting statistics reported in relative (%)- MIL090030 and MIL090032 Pyroxene

Uncertainty due to Counting Statistics (Relative %) MIL090032 and MIL090030-Pyroxene

Comment	No.	SiO2	Al2O3	TiO2	FeO	MgO	MnO	CaO	Cr2O3	NiO
MIL32-pyroxene grain 1-core	26	0.28	2.41	10.95	0.53	0.57	5.84	0.39	8.43	646.69
MIL32-pyroxene grain 1-core	27	0.28	2.45	9.44	0.54	0.57	6.15	0.39	7.59	100.00
MIL32-pyroxene grain 1- rim adj OL	28	0.28	2.29	11.58	0.53	0.58	6.02	0.39	6.68	128.39
MIL32-pyroxene grain 1- rim adj OL	29	0.28	2.29	11.49	0.52	0.58	3.86	0.39	7.82	316.71
MIL32-pyroxene grain 1- rim adj pyx	30	0.28	2.02	8.11	0.50	0.60	6.13	0.39	12.95	100.00
MIL32-pyroxene grain 1- rim adj pyx	31	0.28	2.37	11.51	0.53	0.58	5.57	0.39	6.71	910.69
MIL32-pyroxene grain 2- core	32	0.28	2.31	7.62	0.51	0.59	5.67	0.39	13.14	72.52
MIL32-pyroxene grain 2- core	33	0.28	2.36	8.49	0.52	0.60	4.93	0.39	21.68	6375.17
MIL32-pyroxene grain 2-rim adj pyx	34	0.28	2.24	12.36	0.53	0.57	6.24	0.39	8.66	84.94
MIL32-pyroxene grain 2-rim adj pyx	35	0.28	2.30	9.82	0.54	0.57	5.77	0.39	6.32	100.00
MIL32-pyroxene grain 2-rim adj meso	36	0.30	1.00	3.88	0.38	1.07	4.93	0.40	3949.66	100.00
MIL32-pyroxene grain 2-rim adj meso	37	0.30	0.99	3.73	0.38	1.08	4.79	0.40	100.00	521.36
MIL32-pyroxene grain 3-core	38	0.28	2.52	9.27	0.52	0.58	6.17	0.39	12.75	232.45
MIL32-pyroxene grain 3-core	39	0.28	2.18	8.16	0.51	0.59	5.65	0.39	15.28	100.00
MIL32-pyroxene grain 3-rim adj pyx	40	0.28	2.27	8.04	0.51	0.58	5.24	0.39	9.20	100.00
MIL32-pyroxene grain 3-rim adj pyx	41	0.28	2.29	8.85	0.52	0.58	6.14	0.39	7.57	100.00
MIL32-pyroxene grain 4-core	42	0.28	2.29	9.30	0.54	0.57	5.70	0.39	6.69	387.14
MIL32-pyroxene grain 4-core	43	0.28	2.46	12.00	0.53	0.57	6.09	0.39	10.56	74.92
MIL32-pyroxene grain 4-rim adj meso	44	0.29	1.36	4.52	0.38	0.91	3.95	0.42	121.94	100.00
MIL32-pyroxene grain 4-rim adj meso	45	0.29	1.54	5.45	0.45	0.66	5.44	0.41	26.85	55.66
MIL32-pyroxene grain 5-core	46	0.28	2.28	13.78	0.52	0.59	6.27	0.39	6.55	100.00
MIL32-pyroxene grain 5-core	47	0.28	2.29	7.65	0.52	0.58	6.67	0.39	8.39	491.95
MIL32-pyroxene grain 5-rim adj meso	48	0.29	1.50	4.82	0.41	0.76	4.87	0.41	69.93	100.00
MIL32-pyroxene grain 5-rim adj meso	49	0.29	1.47	4.62	0.39	0.80	4.50	0.42	301.71	100.00
MIL30-pyroxene grain 1-core	72	0.28	2.33	10.51	0.53	0.58	6.28	0.39	5.49	530.61
MIL30-pyroxene grain 1-core	73	0.28	2.16	7.89	0.53	0.58	6.44	0.39	5.31	100.00
MIL30-pyroxene grain 1-rim adj OL	74	0.28	2.09	6.11	0.53	0.57	6.13	0.39	6.52	100.00
MIL30-pyroxene grain 1-rim adj OL	75	0.28	2.43	12.16	0.54	0.57	6.11	0.39	7.15	159.70
MIL30-pyroxene grain 2-core	76	0.28	2.06	8.39	0.53	0.58	6.75	0.39	5.56	100.00
MIL30-pyroxene grain 2-core	77	0.28	2.08	8.07	0.53	0.58	6.33	0.39	4.96	82.27
MIL30-pyroxene grain 2-rim adj meso	78	0.28	2.30	9.20	0.52	0.58	6.11	0.39	7.72	100.00
MIL30-pyroxene grain 2-rim adj meso	79	0.30	1.04	3.36	0.40	0.88	4.77	0.40	100.00	100.00
MIL30-pyroxene grain 3-core	80	0.28	2.19	7.58	0.53	0.58	5.81	0.39	5.75	100.00
MIL30-pyroxene grain 3-core	81	0.28	2.22	9.56	0.53	0.58	6.22	0.39	6.15	699.06
MIL30-pyroxene grain 3-rim adj OL	82	0.28	2.41	9.42	0.53	0.57	6.07	0.39	6.98	100.00
MIL30-pyroxene grain 3-rim adj OL	83	0.28	2.37	8.98	0.52	0.58	6.39	0.39	7.75	6309.79
MIL30-pyroxene grain 4-core	84	0.28	2.19	7.40	0.53	0.59	5.34	0.39	6.12	560.12
MIL30-pyroxene grain 4-core	85	0.28	2.19	9.42	0.53	0.58	5.83	0.39	5.79	61.00
MIL30-pyroxene grain 4-rim adj meso	86	0.29	1.55	5.58	0.47	0.65	5.81	0.40	64.13	100.00
MIL30-pyroxene grain 4-rim adj meso	87	0.28	2.02	7.27	0.50	0.61	6.74	0.39	15.66	148.66
MIL30-pyroxene grain 5-core	88	0.28	2.26	8.16	0.53	0.58	6.78	0.39	5.72	1632.77
MIL30-pyroxene grain 5-core	89	0.28	2.29	7.91	0.52	0.58	6.26	0.39	6.08	184.09
MIL30-pyroxene grain 5-rim adj pyx	90	0.28	2.38	8.63	0.53	0.58	5.96	0.39	7.46	489.06
MIL30-pyroxene grain 5-rim adj pyx	91	0.28	2.38	8.31	0.53	0.58	5.69	0.39	8.58	152.17

Table 14. Uncertainty due to counting statistics reported in relative (%)- MIL090030/32/136- Magnetite

Uncertainty Due to Counting Statistics (Relative %) MIL 090030/090032/090136

Comment	No.	SiO2	Al2O3	TiO2	FeO	MgO	MnO	CaO	Cr2O3	NiO
TEST	1	8.46	1.31	0.47	0.22	8.74	4.87	57.63	100.00	100.00
MIL090136 Magnetite Grain 1	2	7.07	1.66	0.49	0.22	9.45	4.09	30.27	100.00	100.00
MIL0901Magnetite Grain 2-attatched to p	3	5.40	1.30	0.58	0.21	9.93	4.85	17.34	99.66	100.00
MIL090136Magnetite Grain 3-attached to	4	7.22	1.26	0.50	0.22	7.17	5.17	22.87	33.74	101.03
MIL090136 Magnetite Grain 4	5	1.94	3.62	1.50	0.20	14.64	12.85	6.14	851.24	100.00
1MIL090136 Mt Grain 5- intergrown OL?	6	0.38	45.08	273.49	0.24	0.96	2.26	5.71	100.00	100.00
1MIL090136 Mt Grain 6-INTERGROWN OL	7	0.32	2.72	33.47	0.32	1.12	3.54	7.52	100.00	100.00
MIL090136 Mt Grain 7-INTERGROWN FeS	8	5.73	1.63	0.47	0.22	8.48	4.28	13.39	90.35	100.00
MIL090136 Mt Grain 8-INTERGROWN FeS	9	8.82	2.80	1.84	0.19	36.17	12.33	15.23	97.15	219.55
MIL090136 Mt Grain 10	10	8.03	1.60	0.54	0.21	12.30	4.54	24.02	272.18	100.00
MIL090136 Mt Grain 10b-intergrown FeS	11	2.39	3.28	2.69	0.19	15.15	9.01	9.72	159.34	100.00
MIL090136 Mt Grain 11-adj OL	12	4.16	1.63	0.81	0.20	9.86	7.73	8.87	57.71	100.00
MIL090136 Mt Grain 12	13	6.44	1.72	0.49	0.22	10.21	4.20	38.71	54.20	100.00
MIL090136 Mt Grain 13	14	10.63	1.35	0.58	0.21	13.15	5.52	34.19	50.69	100.00
MIL090136 Mt Grain 14	15	8.72	2.86	1.04	0.20	21.27	10.52	11.93	100.00	100.00
MIL090136 Mt Grain 15	16	24.73	362696.13	1261.97	0.21	142.49	40.17	19.48	43.61	100.00
MIL090032 Mt Grain 1	17	9.25	1.32	0.65	0.21	13.54	6.38	21.80	91.82	100.00
MIL090032 Mt Grain 2	18	6.55	1.28	0.53	0.21	14.39	5.11	28.94	129.28	100.00
MIL090032 Mt Grain 3	19	6.92	1.28	0.50	0.22	10.00	5.09	21.71	43.71	149.43
MIL090032 Mt Grain 4-intergrown FeS	20	1.71	2.96	1.57	0.20	14.71	10.27	5.98	100.00	1942.50
MIL090032 Mt Grain 5-with sims point	21	7.37	1.28	0.58	0.21	12.06	5.13	11.61	131.35	100.00
MIL090032 Mt Grain 6-adj pyx	22	7.77	1.33	0.50	0.22	11.82	4.73	17.37	100.00	100.00
MIL090032 Mt Grain 7	23	7.48	1.20	0.59	0.21	13.36	6.30	23.50	551.17	477.28
MIL090032 Mt Grain 8	24	3.02	2.89	1.24	0.19	16.37	13.43	42.30	100.00	100.00
MIL090032 Mt Grain 9-adj ol	25	7.37	1.20	0.51	0.22	8.58	5.00	28.69	29.19	100.00
MIL090032 Mt Grain 10-adj OL	26	11.00	1.25	0.47	0.22	5.24	5.21	25.66	11.25	223.85
MIL090032 Mt Grain 11-adj pyx	27	9.45	1.27	0.49	0.22	5.31	4.97	23.10	17.65	100.00
MIL090032 Mt Grain 12	28	6.87	1.34	0.54	0.21	11.39	5.06	14.59	36.93	125.03
MIL090032 Mt Grain 13	29	7.75	1.58	0.51	0.21	10.81	4.85	33.10	61.66	100.00
MIL090032 Mt Grain 14	30	7.57	1.47	0.54	0.21	10.27	5.41	26.05	160.01	100.00
MIL090032 Mt Grain 15	31	7.12	1.45	0.47	0.22	9.90	4.89	30.42	365.52	100.00
MIL090030 Mt Grain 1	32	8.66	1.72	0.48	0.22	8.07	5.31	20.88	42.40	100.00
MIL090030 Mt Grain 2-elongated	33	8.67	1.56	0.50	0.22	10.82	4.23	71.60	258.39	100.00
MIL090030 Mt Grain 3	34	11.17	1.39	0.50	0.22	12.46	4.47	26.11	100.00	2600.66
MIL090030 Mt Grain 4	35	4.93	1.40	0.47	0.22	8.33	4.00	16.67	34.82	100.00
MIL090030 Mt Grain 5	36	9.70	1.21	0.50	0.22	6.22	5.04	46.67	100.00	100.00
MIL090030 Mt Grain 6	37	8.72	1.34	0.55	0.21	6.10	5.34	39.85	309.31	100.00
MIL090030 Mt Grain 7-spotted	38	2.10	2.64	1.47	0.20	13.72	10.20	8.04	171.97	100.00
MIL090030 Mt Grain 8	39	7.82	5.40	3.86	0.19	38.39	18.12	39.67	100.00	100.00
MIL090030 Mt Grain 9	40	5.19	3.25	2.21	0.19	47.38	15.83	45.32	100.00	663.34
MIL090030 Mt Grain 10	41	7.37	5.38	4.26	0.19	22.22	13.04	13.29	60.44	100.00
MIL090030 Mt Grain 11	42	12.85	2.72	0.89	0.20	17.79	7.75	16.84	243.56	261.03
MIL090030 Mt Grain 12	43	6.89	1.60	0.53	0.21	7.88	5.60	28.37	37.04	100.00
MIL090030 Mt Grain 13	44	8.06	1.42	0.50	0.22	7.29	5.30	16.05	37.69	183.72
MIL090030 Mt Grain 14	45	10.92	1.82	0.55	0.21	11.36	5.50	25.32	68.88	57.67
MIL090030 Mt Grain 15	46	8.39	1.55	0.47	0.22	8.92	4.34	32.66	100.00	100.00

vi. Color Phase Maps using LISPIX

Color Scheme: Red= pyx; Green=Ol; Yellow= Ti-Mt; Blue=Sulfide; Black=mesostasis; Pink=no rock/slide

Figure 43. MIL090136 color phase map of composite 1 and composite 2.

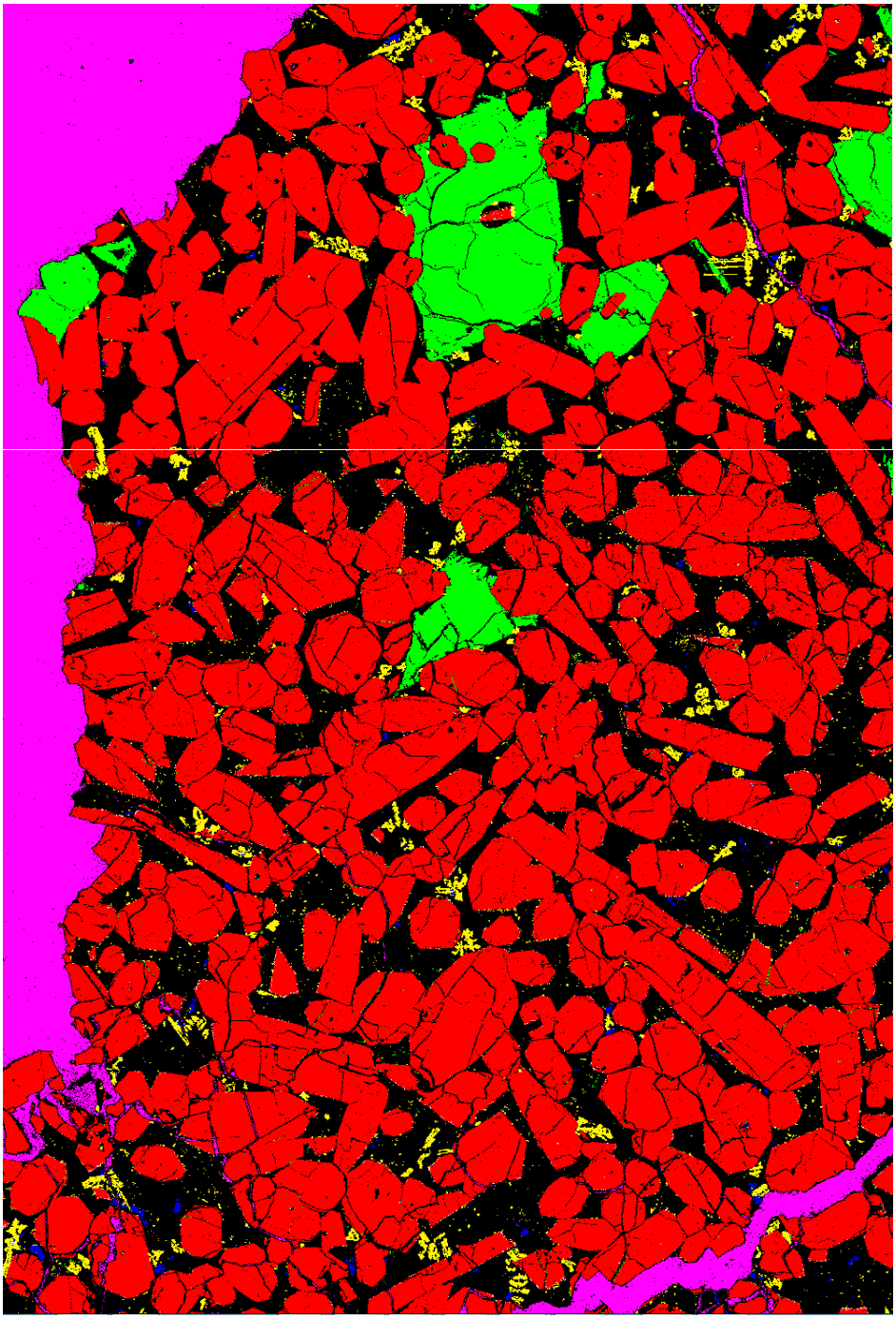

Figure 43. Color phase map of composite 1 and composite 2 of MIL090136. Color phase maps were made in the LISPIX program and used in order to determine the modal abundance of phases. Color Scheme: red= pyroxene; green= olivine; yellow= titano-magnetite; blue= sulfide; black=mesostasis; pink=no rock/slide.

Figure 44. MIL090032 color phase map of composite 1

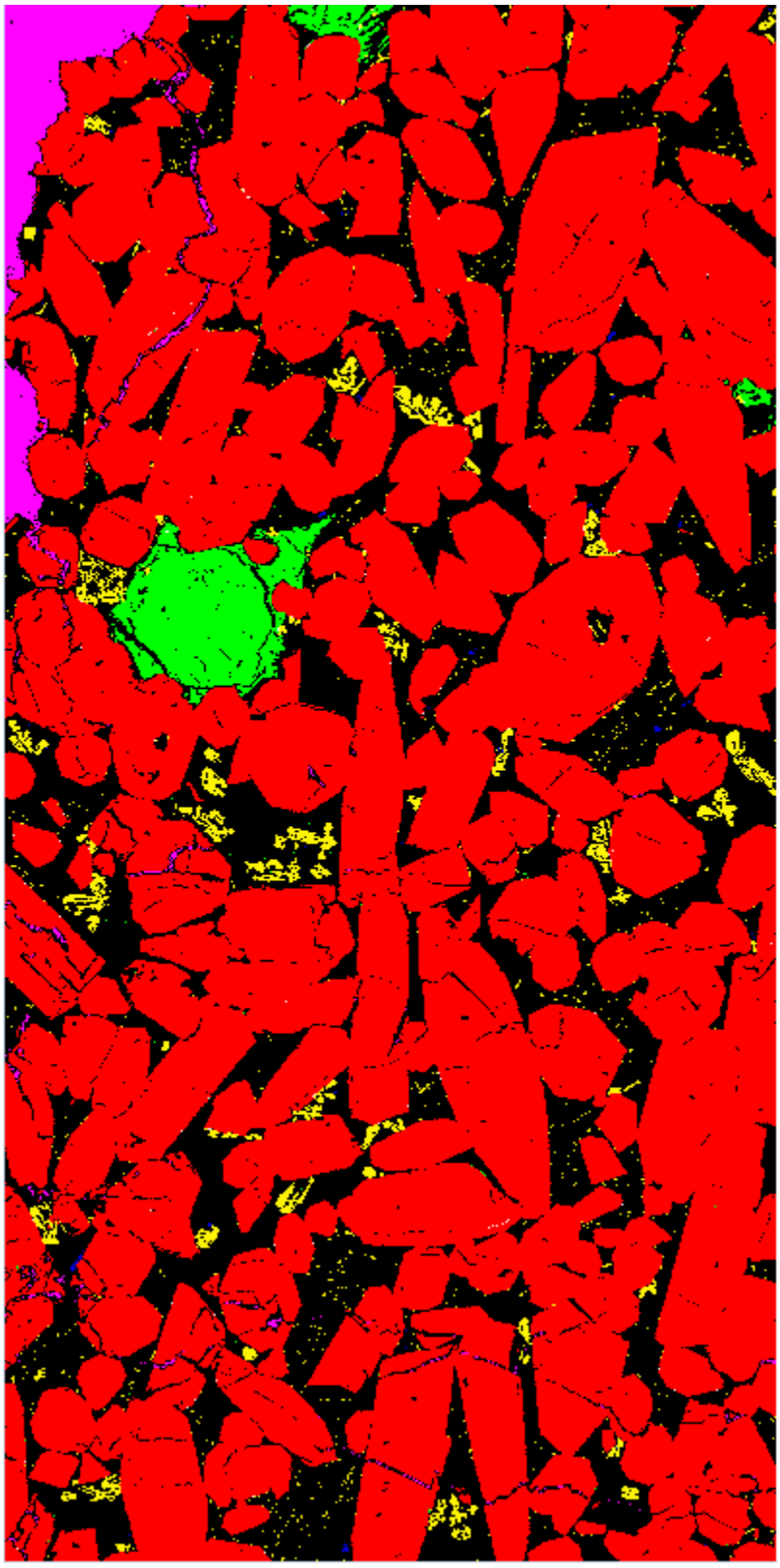

Figure 44. Color phase map of composite 1 of MIL090032. Color phase maps were made in the LISPIX program and used in order to determine the modal abundance of

phases. Color Scheme: red= pyroxene; green= olivine; yellow= titano-magnetite; blue= sulfide; black=mesostasis; pink=no rock/slide.

Figure 45. MIL090032 color phase map of composite 2

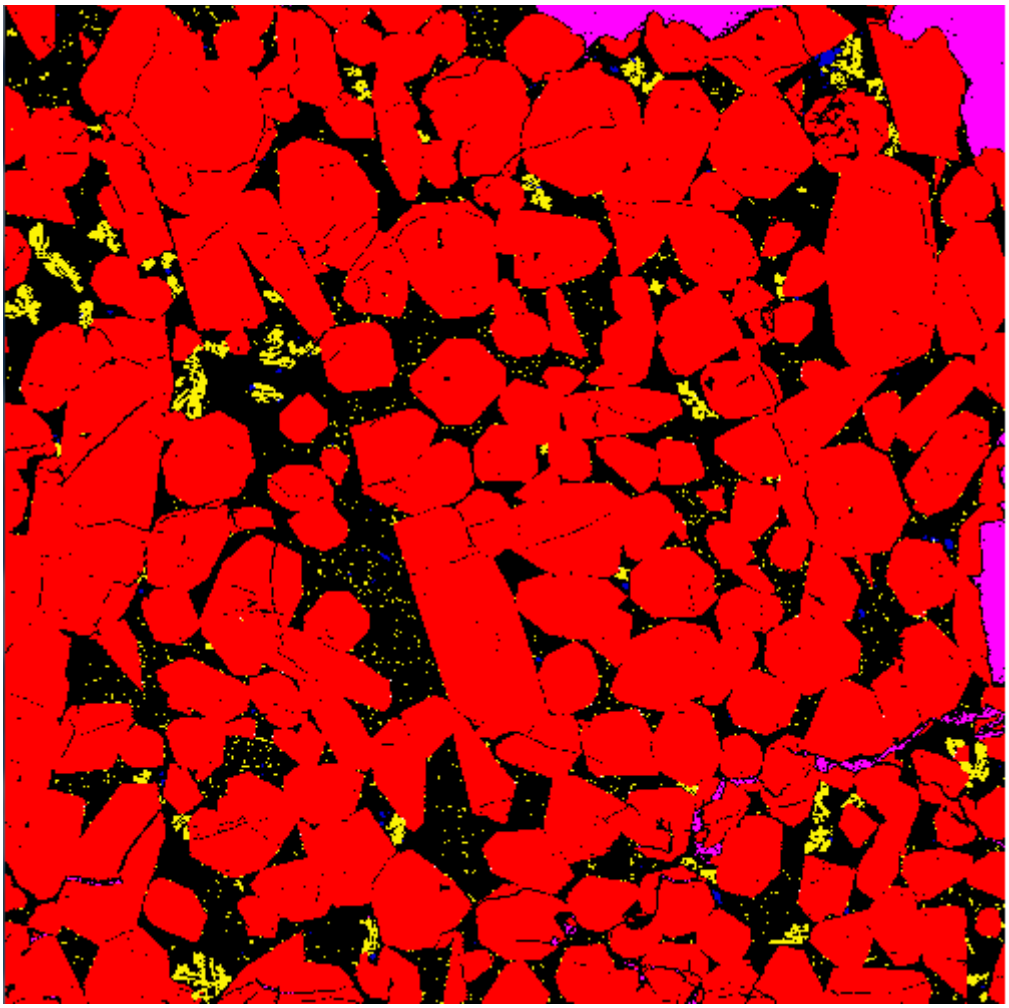

Figure 45. Color phase map of composite 2 of MIL090032. Color phase maps were made in the LISPIX program and used in order to determine the modal abundance of phases. Color Scheme: red= pyroxene; green= olivine; yellow= titano-magnetite; blue= sulfide; black=mesostasis; pink=no rock/slide.

Figure 46. MIL090030 color phase map of composite 1

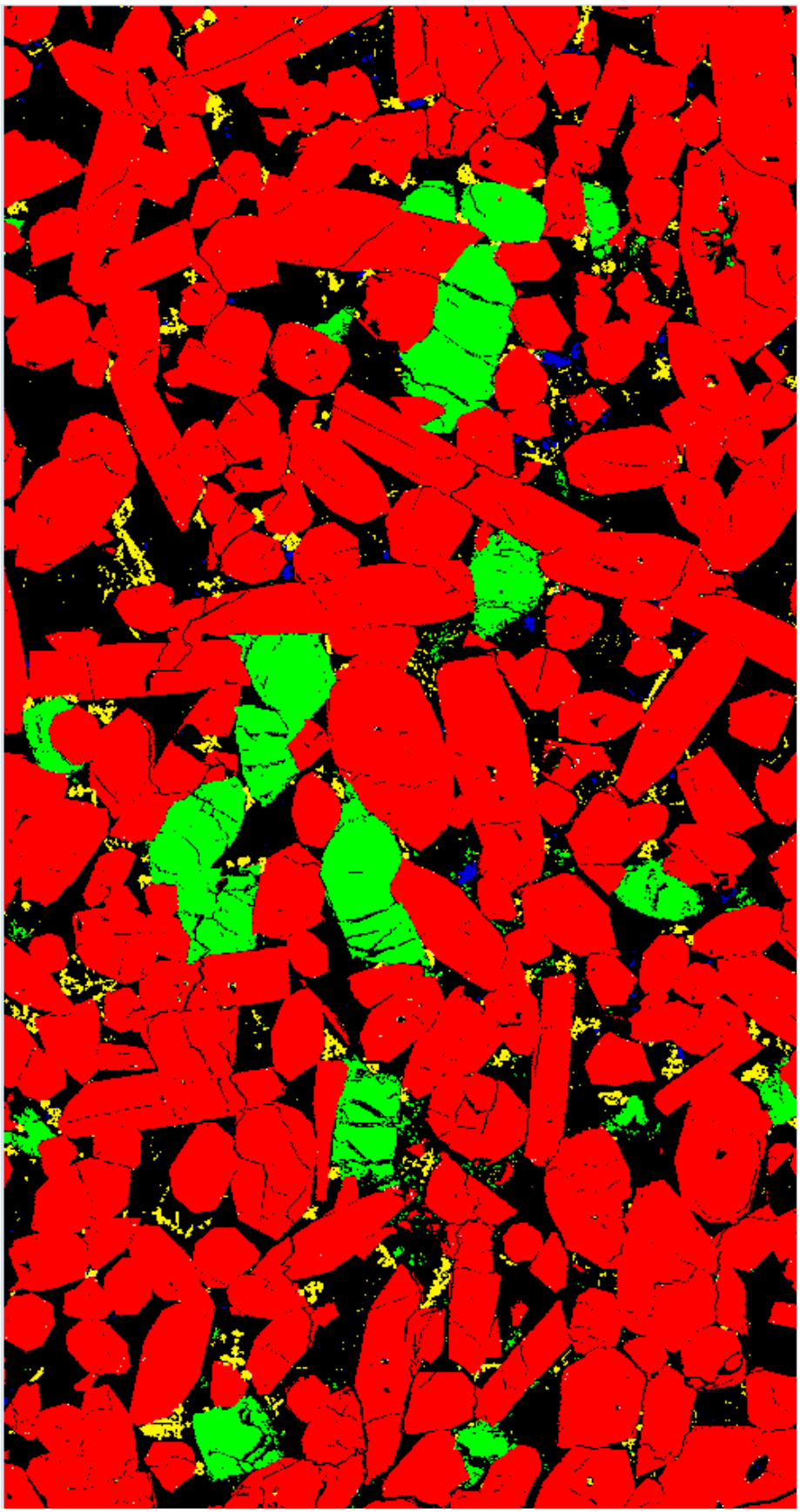

Figure 46. Color phase map of composite 1 of MIL090030. Color phase maps were made in the LISPIX program and used in order to determine the modal abundance of phases. Color Scheme: red= pyroxene; green= olivine; yellow= titano-magnetite; blue= sulfide; black=mesostasis; pink=no rock/slide.

Figure 47. MIL090030 color phase map of composite 2

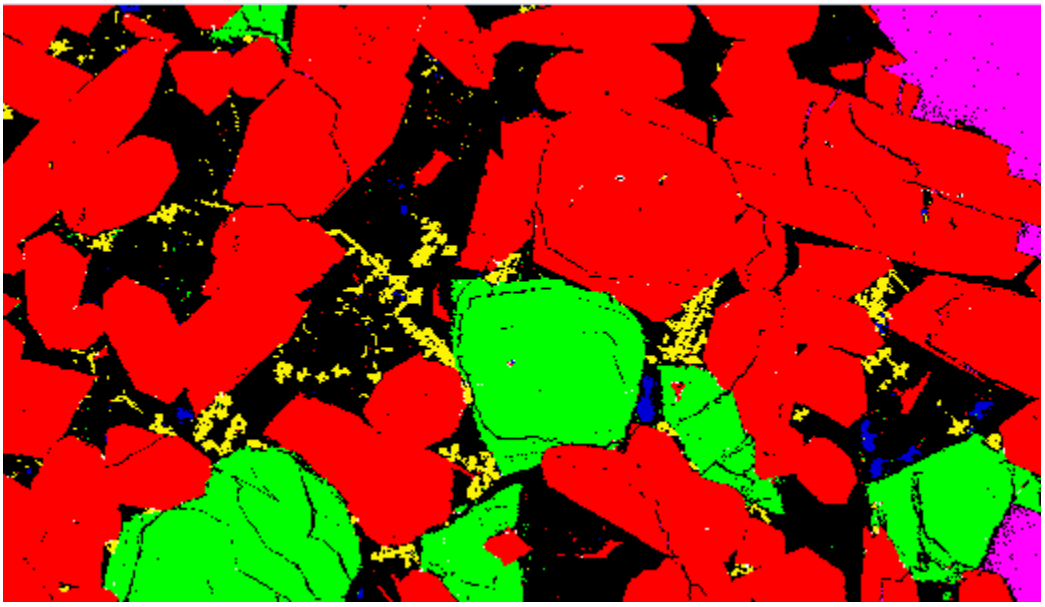

Figure 47. Color phase map of composite 2 of MIL090030. Color phase maps were made in the LISPIX program and used in order to determine the modal abundance of phases. Color Scheme: red= pyroxene; green= olivine; yellow= titano-magnetite; blue= sulfide; black=mesostasis; pink=no rock/slide.

v. Protocol for making modal abundance maps using LISPIX

ON THE PROBE:

1. Export the x-ray maps as TIFFs

ON THE PC

1. Open Photoshop
2. Open the X-ray Maps
3. Choose Save As: TIFF. A window will open. Change Image compression to: **NONE (repeat for all of the images)**

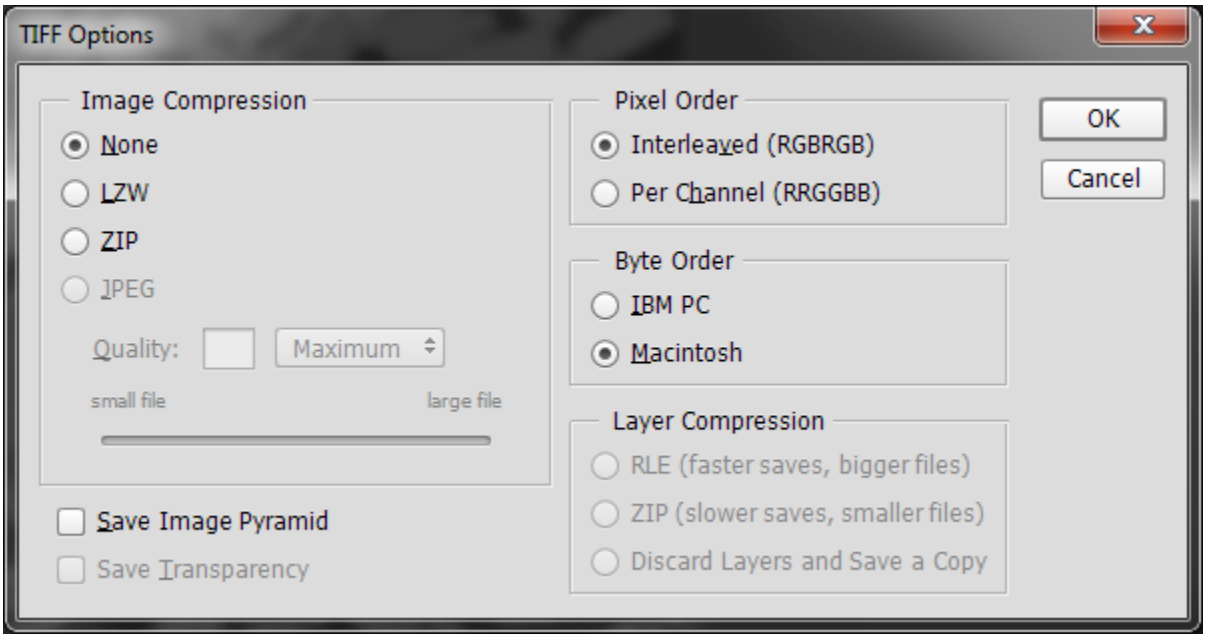

*** IF AN ERROR WINDOW OPENS DURING THIS PROCESS, DO NOT CLOSE IT OR THE PROGRAM WILL CRASH. MOVE IT OUT OF THE WAY, AND CONTINUE.

1. In 'lispixLx190P' go to file open and open the uncompressed image. **(Repeat for all of the images)**
2. Go to TOOLS → PHASE (A window opens)
3. Click the SETUP Button → Select Maps Images Already Open (A window with open files appears)
4. Highlight the maps you want to include → OK
5. Add button → Enter a phase name (e.g. Pyroxene)
6. Click Define Phase (this is a toggle switch)
7. Add (Pick the maps to add). A window opens. Select a map (e.g. Ca). A threshold window opens. Along with an instruction window.
8. Move the left and right ends of the threshold marker to highlight the phase you are interested in. (in the case of Test Map #1, the threshold range is ~61-254)
9. Press the Continue Button (Pyx Mode has been defined on the basis of Ca Only at this point. In the Phase Tool window the values of 61/254 and 58% will be displayed)
10. Press Add to add the Mg
11. Mg map moves forward. Once clicked, move the threshold slider (37/254). Press Continue (Problem 1 for JD-how do you deal with the zoned pyroxenes)
12. Press Add to add the Fe Map. Click Map. Move threshold.
13. If done with this phase, click Choose Map
14. Click Add for the next phase. (e.g. Olivine)

15. (In the Phase Tool Window, make sure the phase you are interested in is defined in Red.
16. Define Phase
17. Add
18. For Ol, click on Mg, and change the thresholds (by default, the old threshold values will appear). Move the cursor over the old threshold slider window, and it will change to Mg.
19. Continue
20. Add Fe for Ol (Fe in Ol + Mesostasis, but the Mg map does not include the mesostasis so it can be subtracted).
21. Click Continue.
22. As a way to verify, click Show Results. And a new map appears. If there are some extraneous pixels, go back and change the slider. Go back to Edit Threshold
23. Choose Map
24. Add
25. Sulfide
26. Define Phase
27. Add
28. Continue
29. Add Fe
30. Use slider to define threshold
31. Continue
32. Add S
33. Use slider to define threshold
34. Continue
35. Show Results
36. Add
37. Magnetite
38. Define Phase
39. Add
40. Fe
41. Use Slider
42. Continue
43. Add
44. Ti
45. Continue
46. Show Results (Combined Phase Map)
47. Add
48. Background

49. Define Phase
50. Add
51. Fe
52. Pick Low (1/1)
53. Ok
54. Show results (combined phase map)

vi. Sulfur isotope data

Table 15. SIMS data from Miller Range (MIL) 090030/090032/090136

Sample	$\delta^{34}S$	$\Delta^{33}S$
MIL090030-1	14.4	-0.66
MIL090030-2	15.4	-0.71
MIL090030-3	14.6	-0.82
MIL090030-4	16.9	-0.53
MIL090030-5	13.3	-0.66
MIL090030-6	15.1	-0.32
MIL090030-7	13.2	-0.67
MIL090030-8	13.9	-0.79
MIL090030-9	14.5	-0.79
MIL090030-10	14.1	-0.77
MIL090030-12	14.6	-0.66
MIL090030-13	11.7	-0.78
Average	**14.3**	**-0.68**
1σ Standard Deviation	**1.3**	**0.14**
MIL090032-1	15.3	-0.65
MIL090032-2	11.7	-0.65
MIL090032-3	14.3	-0.53
MIL090032-4	12.7	-0.63
MIL090032-5	19.4	-0.53
Average	**14.7**	**-0.60**
1σ Standard Deviation	**3.0**	**0.06**
MIL0900136-10	18.4	-0.92
MIL0900136-11	11.2	-0.83
MIL0900136-12	14.0	-0.63
MIL0900136-13	10.4	-0.87
MIL0900136-14	15.1	-0.88
MIL0900136-15	12.0	-0.66
MIL0900136-16	14.1	-0.50
MIL0900136-19	11.0	-0.58
MIL0900136-21	11.6	-0.81
MIL0900136-4	14.4	-0.72
MIL0900136-5	18.3	-0.96
Average	**13.7**	**-0.76**
1σ Standard Deviation	**2.8**	**0.15**

Table 16. Isotopic and concentration data for paired MIL samples

Meteorite	$\delta^{34}S$	$\Delta^{33}S$	$\Delta^{36}S$	S (ppm)
MIL03346, 191*				
Water-soluble sulfate	7.08	-0.207	-0.48	201
Acid-soluble sulfate	10.39	-0.254	-0.11	840
CRS	6.81	-0.434	-0.04	242
MIL090030,41				
Acid-soluble sulfate	6.23	-0.474	-0.28	541
CRS	8.78	-0.538	0.12	212
MIL090032,85				
Water-soluble sulfate	11.73	-0.226	0.38	143
Acid-soluble sulfate	9.01	-0.187	-0.67	674
CRS	8.85	-0.523	0.06	167
MIL090136,32				
Water-soluble sulfate	12.75	-0.176	-0.32	129
Acid-soluble sulfate	9.7	-0.247	0.46	689
CRS	7.66	-0.476	0.18	109

*Data from Kim and Farquhar, LPSC 2008

Bibliography

Ashwal, L.D., Warner, J.L., Wood, C.A., 1982. SNC Meteorites: Evidence against an Asteroidal Origin. J. Geophys. Res. 87, A393–A400.

Ballhaus, C., Berry, R.F., Green, D.H., 1990. Oxygen fugacity controls in the Earth's upper mantle. Nature. doi:10.1038/348437a0

Becker, R.H., Pepin, R.O., 1984. The case for a martian origin of the shergottites: nitrogen and noble gases in EETA 79001. Earth Planet. Sci. Lett. 69, 225–242. doi:10.1016/0012-821X(84)90183-3

Bogard, D.D., Nyquist, L.E., Johnson, P., 1984. Noble gas contents of shergottites and implications for the Martian origin of SNC meteorites. Geochim. Cosmochim. Acta 48, 1723–1739. doi:10.1016/0016-7037(84)90028-0

Burgess, R., Wright, I.P., Pillinger, C.T., 1989. Distribution of sulphides and oxidised sulphur components in SNC meteorites. Earth Planet. Sci. Lett. 93, 314–320. doi:10.1016/0012-821X(89)90030-7

Chevrier, V., Lorand, J.P., Sautter, V., 2011. Sulfide petrology of four nakhlites: Northwest Africa 817, Northwest Africa 998, Nakhla, and Governador Valadares. Meteorit. Planet. Sci. 46, 769–784. doi:10.1111/j.1945-5100.2011.01189.x

Chevrier, V., Mathé, P.E., 2007. Mineralogy and evolution of the surface of Mars: A review. Planet. Space Sci. 55, 289–314. doi:10.1016/j.pss.2006.05.039

Cottrell, E., Kelley, K.A., 2011. The oxidation state of Fe in MORB glasses and the oxygen fugacity of the upper mantle. Earth Planet. Sci. Lett. 305, 270–282. doi:10.1016/j.epsl.2011.03.014

Day, J.M.D., Taylor, L.A., Floss, C., McSween, H.Y., 2006. Petrology and chemistry of MIL 03346 and its significance in understanding the petrogenesis of nakhlites on Mars. Meteorit. Planet. Sci. 41, 581–606. doi:10.1111/j.1945-5100.2006.tb00484.x

Dehouck, E., Gaudin, A., Chevrier, V., Mangold, N., 2016. Mineralogical record of the redox conditions on early Mars. Icarus 271, 67–75. doi:10.1016/j.icarus.2016.01.030

Dyar, M.D., Treiman, A.H., Pieters, C.M., Hiroi, T., Lane, M.D., O'Connor, V., 2005. MIL03346, the most oxidized Martian meteorite: A first look at spectroscopy, petrography, and mineral chemistry. J. Geophys. Res. E Planets 110, 1–9. doi:10.1029/2005JE002426

Ehlmann, B.L., Edwards, C.S., 2014. Mineralogy of the Martian Surface. Annu. Rev. Earth Planet. Sci. 42, 291–315. doi:10.1146/annurev-earth-060313-055024

Farquhar, J., Kim, S.T., Masterson, A., 2007. Implications from sulfur isotopes of the Nakhla meteorite for the origin of sulfate on Mars. Earth Planet. Sci. Lett. 264, 1–8. doi:10.1016/j.epsl.2007.08.006

Farquhar, J., Savarino, J., Jackson, T.L., Thiemens, M.H., 2000. Evidence of atmospheric sulphur in the martian regolith from sulphur isotopes in meteorites. Nature 404, 50–52. doi:10.1038/35003517

Franz, H.B., Kim, S.-T., Farquhar, J., Day, J.M.D., Economos, R.C., McKeegan,

K.D., Schmitt, A.K., Irving, A.J., Hoek, J., Dottin, J., 2014. Isotopic links between atmospheric chemistry and the deep sulphur cycle on Mars. Nature 508, 364–8. doi:10.1038/nature13175

Gao, X., Thiemens, M., 1990. Sulfur Isotopic Studies in Meteorites. LPSC 29. doi:10.1017/CBO9781107415324.004

Gendrin, A., Mangold, N., Bibring, J.-P., Langevin, Y., Gondet, B., Poulet, F., Bonello, G., Quantin, C., Mustard, J., Arvidson, R., LeMouélic, S., 2005. Sulfates in Martian layered terrains: the OMEGA/Mars Express view. Science 307, 1587–1591. doi:10.1126/science.1109087

Greenwood, J.P., Riciputi, L.R., McSween, H.Y., 1997. Sulfide isotopic compositions in shergottites and ALH84001, and possible implications for life on Mars. Geochim. Cosmochim. Acta 61, 4449–4453. doi:10.1016/S0016-7037(97)00246-9

Hallis, L.J., Taylor, G.J., 2011. Comparisons of the four Miller Range nakhlites, MIL 03346, 090030, 090032 and 090136: Textural and compositional observations of primary and secondary mineral assemblages. Meteorit. Planet. Sci. 46, 1787–1803. doi:10.1111/j.1945-5100.2011.01293.x

Harner, P.L., Gilmore, M.S., 2015. Visible–near infrared spectra of hydrous carbonates, with implications for the detection of carbonates in hyperspectral data of Mars. Icarus 250, 204–214. doi:10.1016/j.icarus.2014.11.037

Herd, C.D.K., Borg, L.E., Jones, J.H., Papike, J.J., 2002. Oxygen fugacity and geochemical variations in the martian basalts: Implications for martian basalt petrogenesis and the oxidation state of the upper mantle of Mars. Geochim.

Cosmochim. Acta 66, 2025–2036. doi:10.1016/S0016-7037(02)00828-1

Hulston, J.R., Thode, H.G., 1965. Cosmic-Ray-Produced S and S in the Metallic Phase of Iron Meteorites. J. Geophys. Res. 70.

Hulston, J.R., Thode, H.G., 1965. Variations in the S S and S Contents of Meteorites and Their Relation to Chemical and Nuclear Effects. 3OURNAL Geophys. RESEAR 70, 3475–3484.

Johnson, J.R., Bell, I.F., Cloutis, E., Staid, M., Farrand, W.H., McCoy, T., Rice, M., Wang, A., Yen, A., 2007. Mineralogic constraints on sulfur-rich soils from Pancam spectra at Gusev crater, Mars. Geophys. Res. Lett. 34, 1–6. doi:10.1029/2007GL029894

Kim, S.-T., Farquhar, J., 2008. MULTIPLE SULFUR ISOTOPE COMPOSITIONS IN MARTIAN METEORITE MIL 03346. LPSC 127–128.

Kounaves, S.P., Carrier, B.L., O'Neil, G.D., Stroble, S.T., Claire, M.W., 2014. Evidence of martian perchlorate, chlorate, and nitrate in Mars meteorite EETA79001: Implications for oxidants and organics. Icarus 229, 206–213. doi:10.1016/j.icarus.2013.11.012

Kuebler, K.E., 2013. A combined electron microprobe (EMP) and Raman spectroscopic study of the alteration products in Martian meteorite MIL 03346. J. Geophys. Res. E Planets 118, 347–368. doi:10.1029/2012JE004244

Labidi, J., Cartigny, P., Jackson, M.G., 2015. Multiple sulfur isotope composition of oxidized Samoan melts and the implications of a sulfur isotope "mantle array" in chemical geodynamics, Earth and Planetary Science Letters. doi:10.1016/j.epsl.2015.02.004

Lichtenberg, K.A., Arvidson, R.E., Morris, R. V., Murchie, S.L., Bishop, J.L., Remolar, D.F., Glotch, T.D., Dobrea, E.N., F.Mustard, J., Andrews-Hanna, J., Roach, L.H., 2010. Stratigraphy of hydrated sulfates in the sedimentary deposits of aram chaos, mars. J. Geophys. Res. E Planets 115, 1–13. doi:10.1029/2008JE003208

Mandeville, C.W., Webster, J.D., Tappen, C., Taylor, B.E., Timbal, A., Sasaki, A., Hauri, E., Bacon, C.R., 2009. Stable isotope and petrologic evidence for open-system degassing during the climactic and pre-climactic eruptions of Mt. Mazama, Crater Lake, Oregon. Geochim. Cosmochim. Acta 73, 2978–3012. doi:10.1016/j.gca.2009.01.019

McCanta, M.C., Elkins-Tanton, L., Rutherford, M.J., 2009. Expanding the application of the Eu-oxybarometer to the iherzolitic shergottites and nakhlites: Implications for the oxidation state heterogeneity of the Martian interior. Meteorit. Planet. Sci. 44, 725–745. doi:10.1111/j.1945-5100.2009.tb00765.x

McCubbin, F.M., Tosca, N.J., Smirnov, A., Nekvasil, H., Steele, A., Fries, M., Lindsley, D.H., 2009. Hydrothermal jarosite and hematite in a pyroxene-hosted melt inclusion in martian meteorite Miller Range (MIL) 03346: Implications for magmatic-hydrothermal fluids on Mars. Geochim. Cosmochim. Acta 73, 4907–4917. doi:10.1016/j.gca.2009.05.031

Mickouchi, T., Miyamoto, M., Koizumi, E., Makishima, J., McKay, G., 2006. Relative Burial Depths of Nakhlites: an Update. LPSC. doi:10.1017/CBO9781107415324.004

Mojzsis, S.J., Coath, C.D., Greenwood, J.P., McKeegan, K.D., Harrison, T.M., 2003.

Mass-independent isotope effects in Archean (2.5 to 3.8 Ga) sedimentary sulfides determined by ion microprobe analysis. Geochim. Cosmochim. Acta 67, 1635–1658. doi:10.1016/S0016-7037(03)00059-0

Murchie, S., Roach, L., Seelos, F., Milliken, R., Mustard, J., Arvidson, R., Wiseman, S., Lichtenberg, K., Andrews-Hanna, J., Bishop, J., Bibring, J.P., Parente, M., Morris, R., 2009. Evidence for the origin of layered deposits in Candor Chasma, Mars, from mineral composition and hydrologic modeling. J. Geophys. Res. E Planets 114, 1–15. doi:10.1029/2009JE003343

Nyquist, L.E., Bogard, D.D., Greshake, A., Eugster, O., 2001. The clan of Martian meteorites , formerly called SNCs after S hergotty , N akhla and C hassigny , now consists of 16 unpaired meteorites of magmatic origin (basalts and ultramafic cumulates). Generally young crystallization ages (with the exception of 105–164.

O'Neill, H.S.C., Wall, V.J., 1987. The Olivine-Orthopyroxene-Spinel Oxygen Geobarometer , the Nickel Precipitation Curve , and the Oxygen Fugacity of the Earth ' s Upper Mantle. J. Petrol. 28, 1169.

Ono, S., Eigenbrode, J.L., Pavlov, A.A., Kharecha, P., Rumble, D., Kasting, J.F., Freeman, K.H., 2003. New insights into Archean sulfur cycle from mass-independent sulfur isotope records from the Hamersley Basin, Australia. Earth Planet. Sci. Lett. 213, 15–30. doi:10.1016/S0012-821X(03)00295-4

Ott, U., Begeman, F., 1985. Are all the "martian" meteorites from Mars? Nature 317, 509–512. doi:10.1038/317509a0

Pollack, J.B., Black, D.C., 1982. Noble gases in planetary atmospheres: Implications

for the origin and evolution of atmospheres. Icarus 51, 169–198. doi:10.1016/0019-1035(82)90079-3

Richter, F., Chaussidon, M., Mendybaev, R., Kite, E., 2016. Reassessing the cooling rate and geologic setting of Martian meteorites MIL 03346 and NWA 817. Geochim. Cosmochim. Acta 182, 1–23. doi:10.1016/j.gca.2016.02.020

Righter, M., Lapen, T.J., Andreasen, R., Irving, A.J., 2016. Sm-Nd and Lu-Hf isotope systematics of Nakhlite NWA 1053. Goldschmidt.

Rutherford, M.J., Calvin, C., Nicholis, M., McCanta, M., 2005. PETROLOGY AND MELT COMPOSITIONS IN NAKHLITE MIL-03346: SIGNIFICANCE OF DATA FROM NATURAL SAMPLE AND FROM EXPERIMENTALLY FUSED GROUNDMASS AND M.I.'s. LPSC 36.

Savarino, J., 2003. UV induced mass-independent sulfur isotope fractionation in stratospheric volcanic sulfate. Geophys. Res. Lett. 30, 9–12. doi:10.1029/2003GL018134

Stolper, E., McSween, H.Y., 1979. Petrology and origin of the shergottite meteorites. Geochim. Cosmochim. Acta 43, 1475–1498. doi:10.1016/0016-7037(79)90142-X

Szymanski, A., Brenker, F.E., Palme, H., El Goresy, A., 2010. High oxidation state during formation of Martian nakhlites. Meteorit. Planet. Sci. 45, 21–31. doi:10.1111/j.1945-5100.2009.01002.x

Thode, H.., Monster, J., Dunford, H.., 1961. Sulphur isotope geochemistry. Geochim. Cosmochim. Acta 25, 159–174. doi:10.1016/0016-7037(61)90074-6

Tosca, N.J., McLennan, S.M., Clark, B.C., Grotzinger, J.P., Hurowitz, J.A., Knoll,

A.H., Schröder, C., Squyres, S.W., 2005. Geochemical modeling of evaporation processes on Mars: Insight from the sedimentary record at Meridiani Planum. Earth Planet. Sci. Lett. 240, 122–148. doi:10.1016/j.epsl.2005.09.042

Tuff, J., Wade, J., Wood, B.J., 2013. Volcanism on Mars controlled by early oxidation of the upper mantle. Nature 498, 342–345. doi:10.1038/nature12225

Udry, A., McSween, H.Y., Lecumberri-Sanchez, P., Bodnar, R.J., 2012. Paired nakhlites MIL 090030, 090032, 090136, and 03346: Insights into the Miller Range parent meteorite. Meteorit. Planet. Sci. 47, 1575–1589. doi:10.1111/j.1945-5100.2012.01420.x

van der Plas, L.V.D., Tobi, A.C., 1965. A chart for judging the reliability of point counting resuts. Am. J. Sci. doi:10.2475/ajs.263.8.722

Wadhwa, M., 2008. Redox Conditions on Small Bodies, the Moon and Mars. Rev. Mineral. Geochemistry 68, 493–510. doi:10.2138/rmg.2008.68.17

Wadhwa, M., 2001. Redox state of Mars' upper mantle and crust from Eu anomalies in shergottite pyroxenes. Science 291, 1527–1530. doi:10.1126/science.1057594

Wray, J.J., Noe Dobrea, E.Z., Arvidson, R.E., Wiseman, S.M., Squyres, S.W., McEwen, A.S., Mustard, J.F., Murchie, S.L., 2009. Phyllosilicates and sulfates at Endeavour Crater, Meridiani Planum, Mars. Geophys. Res. Lett. 36, 1–5. doi:10.1029/2009GL040734

Wray, J.J., Squyres, S.W., Roach, L.H., Bishop, J.L., Mustard, J.F., Noe Dobrea, E.Z., 2010. Identification of the Ca-sulfate bassanite in Mawrth Vallis, Mars. Icarus 209, 416–421. doi:10.1016/j.icarus.2010.06.001